Amorphization of S, Cl-salts induced by Martian Dust Activities

Alian Wang[1], Yuanchao Yan[1], Darby Dyar[2], Jennifer L. Houghton[3], William Farrell[4], Bradley L. Jolliff[5], Scott M. McLennan[6], Erbin Shi[5], and Hongkun Qu[1]

[1]Washington University in St. Louis
[2]Mount Holyoke College
[3]Washington Univ, Dept Earth & Planetary Sci, St Louis, MO 63130 USA
[4]NASA/Goddard Space Flight Center, Greenbelt, Maryland, USA
[5]Dept. Earth and Planetary Sciences
[6]Stony Brook University

November 24, 2022

Abstract

A high proportion of non-crystalline (X-ray-amorphous) components has been found in all samples analyzed by CheMin on the Curiosity rover at Gale crater on Mars, and such X-ray-amorphous components probably occur at all sites that have been investigated thus far by landers and rovers. The amorphous material at Gale crater is rich in volatiles (S, Cl, and H2O), as indicated by other science payload elements (APXS, SAM). We demonstrate here that amorphization of S and Cl salts can be induced by energetic electrons and free radicals generated in a medium-strength electrostatic discharge (ESD) process during martian dust activities such as dust storms, dust devils, and grain saltation. Furthermore, we found that the amorphization is commonly accompanied by dehydration of the salts and oxidation of Cl, S, and Fe species. On the basis of experimentally observed rates of the above phase transformations and the mission-observed dust activities and wind speeds on Mars, we anticipate that similar phase transformations could occur on Mars within a time frame of years to hundreds of years. Considering the high frequency, long duration, and large areal coverage of Martian dust activities, our study suggests that the ESD induced by Martian dust activities may have contributed to some the S- and Cl-rich portion of X-ray amorphous materials observed in surface soils at Gale crater. Furthermore, dust activities in the Amazonian period may have generated and deposited a significant quantity

Amorphization of S, Cl-salts by Martian Dust Activities

Alian Wang[1], Yuanchao Yan[1], Darby Dyar[2], Jen Houghton[1], William M. Farrell[3], Bradley Jolliff[1], Scott McLennan[4], Erbin Shi[1,5], Hongkun Qu[1,5]

[1]Dept. Earth & Planetary Sciences and McDonnell Center for the Space Sciences, Washington University in St. Louis (alianw@levee.wustl.edu),
[2]Planetary Science Institute, 1700 E. Fort Lowell, Suite 106, Tucson, AZ 85719.
[3]Solar System Exploration Division, Goddard Space Flight Center (GSFC), NASA, USA.
[4]Dept. Geoscience, Stony Brook University, Stony Brook, NY 11794
[5]Dept. Physics and Space Sciences, Shandong University at Weihai, China.

Corresponding author: Alian Wang

Key points

- Amorphization of S and Cl salts was induced by electrostatic discharge (ESD) in a Mars chamber that simulates martian dust activities.
- Amorphization is commonly accompanied by dehydration of salts and the oxidation of Fe, Cl, and S species.
- Dust activities may have generated and deposited large quantities of S- and Cl-rich amorphous materials all over the martian surface.

Abstract

A high proportion of non-crystalline (X-ray-amorphous) components has been found in all samples analyzed by CheMin on the *Curiosity Rover* at Gale Crater on Mars, and such X-ray-amorphous components probably occur at all sites that have been investigated thus far by landers and rovers. The amorphous material at Gale Crater is rich in volatiles (S, Cl, and H_2O), as indicated by other science payload elements (APXS, SAM). We demonstrate here that amorphization of S and Cl salts can be induced by energetic electrons and free radicals generated in a medium-strength electrostatic discharge (ESD) process during martian dust activities such as dust storms, dust devils, and grain saltation. Furthermore, we found that the amorphization is commonly accompanied by dehydration of the salts and oxidation of Cl, S, and Fe species. On the basis of experimentally observed rates of the above phase transformations and the mission-observed dust activities and wind speeds on Mars, we anticipate that similar phase transformations could occur on Mars within a time frame of years to hundreds of years. Considering the high frequency, long duration, and large areal coverage of martian dust activities, our study suggests that the ESD induced by martian dust activities may have contributed to some the S- and Cl-rich portion of X-ray amorphous materials observed at Gale Crater. Furthermore, dust activities in the Amazonian period may have generated and deposited a significant quantity of S- and Cl-rich amorphous materials all over Mars.

Plan language summary

Martian dust activities have physically altered the morphology of the surface of Mars. When electrostatic discharge (ESD) is induced by dust activity, it exerts two additional processes on the surface materials: it physically impacts them with energetic electrons and chemically attacks them with free radicals and electrons, causing mineral and chemical reactions. Our study reports experimental findings through a simulated ESD process on various Mars-relevant minerals in a Mars environmental chamber. Three types of phase transformations in S and Cl salts were induced by a moderate-strength ESD process: amorphization, dehydration, and oxidation of Cl, S, and Fe. Based on these observations, and considering the areal and temporal extent of martian dust activities during the Amazonian period, i.e., dust storms, dust devils, and dust- and sand-grain saltation, they may have generated and deposited a large quantity of S- and Cl-rich amorphous materials all over the surface of Mars.

1. Introduction

Among many great findings in martian mineralogy, the discovery of X-ray amorphous components in all samples analyzed by CheMin on the *Curiosity* rover at Gale Crater (Bish et al., 2013, Blake et al., 2013, Vaniman et al., 2014) has been an eye-opening discovery. The proportion of X-ray amorphous components in different martian samples ranges from 19-36 wt% in active and inactive dune materials to 20-54 wt% in all mudstones and 14-71 wt% in non-altered and altered Stimson formation samples (Achilles et al., 2017; Morris, et al., 2016; Morrison et al., 2018a; Rampe et al., 2017, 2018; Yen et al., 2017), implying multiple geological processes for producing the X-ray amorphous components.

In the early history of Mars, several geological processes would form species with low crystallinity. These processes include volcanic activity, impacts, hydrothermal activity, and chemical (including acidic) weathering at low temperature that could free (or partially free) molecules or ionic groups in geological materials, but with insufficient time (or energy) for the newly formed phases to reach crystallographic equilibrium (i.e., a high degree of crystallinity).

A phenomenon with equal significance was that the X-ray amorphous components in all Gale crater samples have a high concentration of volatile-element components (e.g., SO_3 and Cl), a conclusion from combined CheMin and APXS data analyses (Dehouck et al., 2014; Morris et al., 2016; Rampe et al., 2017, 2018; Yen et al., 2017; Achilles et al., 2017), based on a newly developed method to refine unit-cell parameters that has increased the accuracy in derived major-mineral chemistry (Morrison et al, 2018b). An overview published by Morrison et al. (2018a) revealed the highest average concentration of SO_3 + Cl in the amorphous components to be 18.5 wt% from two soil samples, among all 13 samples from Bradbury landing through Naukluft Plateau (69 -1332 sols) at Gale crater. In addition, the data from the SAM payload on the same set of collected samples support the existence of poorly crystalline magnesium and iron sulfates and the association of water with amorphous phases (Sutter et al. 2017, 2019). A relevant observation made by the *Spirit* and *Opportunity* rovers at Gusev crater and Meridiani Planum, was that a higher content of SO_3 and Cl were found in surface soils and un-brushed rock surfaces than in rock interiors (Gellert et al., 2006). A key follow up question is: By what processes could some of the S- and Cl-bearing salts at the martian surface become (or form as) X-ray amorphous materials?

A sudden exposure (by impact or by rover trench, e.g., Byrne et al., 2009; Wang et al., 2006a) of subsurface hydrous sulfates to current atmospheric conditions at the martian surface, as simulated by vacuum desiccation of hydrous salts in laboratory experiments (Sklute et al., 2015; Vaniman et al., 2004; Wang et al., 2006b, Wang and Zhou 2014), could have formed amorphous sulfates directly from crystalline Mg, Fe^{2+}, and Fe^{3+} sulfates. Another process, a sudden release of subsurface brine(s) to the current martian surface with subsequent desiccation may also form non-crystalline salts. Geological processes on present-day Mars that might induce subsurface brine release could be Recurring Slope Lineae (RSL) (McEwen et al., 2014, Wang et al., 2019) and impacts. In a fast brine-dehydration laboratory simulation, amorphous ferric sulfates were first found to form at mid to high temperatures (293-323 K) (Sklute et al., 2015; Wang et al., 2012), and amorphous Mg, Fe^{2+}, Fe^{3+} (but not Ca, K, Na) sulfates formed at 77 K (Morris et al., 2015). Sklute et al. (2018) further revealed the formation of amorphous phases from pure $FeCl_3$ brine (but not from pure $CaCl_2$, $MgCl_2$, and NaCl brines), and from the brines of mixed salts, i.e., $Fe_2(SO_4)_3$ mixed with Na, Mg, Ca, Fe^{3+} chlorides and Na bicarbonate, at room temperature. Toner et al. (2014) observed that amorphous glasses of $Mg(ClO_4)_2$ and $Ca(ClO_4)_2$ formed near 153 K by cooling the relevant brines below their eutectic temperatures. Furthermore, both amorphous Mg and Fe^{3+}sulfates can host structural H_2O to various degrees (up to three structural H_2O per Mg-sulfate molecule, and up to eleven structural H_2O per Fe^{3+}-sulfate molecule), all of which are stable at low relative humidity (RH <11%) and in a wide temperature range (278-323 K) (Wang et al., 2009, 2012).

In addition, energetic particles from space, such as galactic cosmic rays and energetic UV photons, are capable of damaging the crystal structures of surface minerals on airless planetary bodies, while their effect on martian secondary minerals at the surface needs further investigation.

On the basis of the studies referenced above and our previous experimental investigations (Wu et al., 2018, Wang et al., 2020), we hypothesize that S- and Cl-rich X-ray amorphous materials at the surface of Mars may be very common, and one mechanism to produced them is by *multiphase redox plasma chemistry* (or simply, *electrochemistry*) induced by electrostatic discharge (ESD) that occurred during martian dust activities during the Amazonian period. In this manuscript, we report the results of 75 sets of ESD experiments on 22 Mars-relevant minerals under martian atmospheric conditions to explore and test our hypothesis.

We present some background about ESD in martian dust events in section 2, the studied samples and the experiments in section 3, and the results in section 4. We then report the finding of three phase transformation trends in section 5, and discuss the implications of our study in section 6.

2. Martian dust activities, ESD, free radicals, and electrochemistry

Frictional electrification of mineral particles and aerosols can occur in four types of martian surface processes: volcanic eruption, dust storm, dust devil, and grain saltation. Except for volcanic eruptions, the last three processes occur continuously on present-day Mars. For example, a regional dust storm occurs every martian year and a global dust storm occurs every 6-8 Earth years (Shirley, 2015; Wang and Richardson, 2015). Dust devils have been observed by all landed missions on Mars (Metzger and Carr, 1999; Ferri at al., 2000; Ellehoj et al., 2010; Greeley et al., 2006, 2010; Lemmon et al., 2017; Murphy et al., 2016), as well as remotely by orbital observations (Cantor et al., 2006; Choi and Dundas, 2011; Reiss and Lorentz, 2016; Verba et al., 2010; Whelley and Greeley, 2008). Grain saltation was first confirmed on Mars at Meridiani Planum and Gusev Crater (Sullivan et al., 2005, 2008), with laboratory simulations suggesting that they could be a ubiquitous occurrence on the martian surface (Sullivan and Kok, 2017).

A tendency for triboelectric charge was revealed by experiments (Forward et al., 2009; Krauss et al., 2003), i.e., generation of negative charges on smaller grains, but positive charges on larger grains of similar composition. Separation of smaller grains from larger grains by convective martian dust storms and dust devils would generate a large-scale charge separation, i.e., *an active electric field (E-field)*. On Earth, E-fields of up to 60 kv/m were detected during the passage of dust devils (Esposito et al., 2016; Farrell et al., 2004; Harrison et al., 2016; Jackson and Farrell, 2006), and 166 kv/m during grain saltation (Schmidt et al., 1998).

When a local E-field accumulates beyond the *breakdown electric field threshold* (BEFT), electrostatic discharge (ESD) can occur. BEFT on Mars is estimated to be ~ 20-25 kv/m from modeling (Melnik and Parrot, 1998) and ~ 25-34 kv/m from measurements in Mars environmental chambers (Farrell et al., 2015; Yan et al., 2017). This is about 1% of the BEFT on Earth (~ 3000 kv/m), consistent with martian atmospheric pressure being < 1% that of Earth. Therefore, ESD occurs on Mars much more easily than on Earth. Among the three types of ESD processes (Gallo, 1975), *Townsend dark discharge (TDD)* and *normal glow discharge (NGD)* would more likely occur on Mars, but not *lightning*. Unlike what occurs on Earth, the low BEFT on Mars prevents the accumulation and separation of large amounts of charges. In a set of experiments simulating grain saltation using silicates under Mars atmospheric composition and pressure, Bak et al. (2017) detected light emissions (red colored glow from quartz sand and blue colored glow from basaltic sand) that are similar to normal glow discharge (NGD) in a Mars chamber simulated in our laboratory (Wang et al., 2020; Wu et al., 2018).

ESD generates a flux of electrons with high kinetic energy (i.e., a relatively high drift speed), producing an electron avalanche. When these electrons collide with CO_2, O_2, N_2, Ar, and H_2O in the martian atmosphere, electron impact ionization (EII) of CO_2, electron/CO_2 dissociation attachment (ED of CO_2), and electron/H_2O dissociation attachment (ED of H_2O) can occur (Jackson et al., 2010; Wu et al., 2018). This generates free radicals, such as ions with positive and negative charges, neutral species at excited states, and additional electrons that could cause further chain electron avalanches (Delory et al., 2006).

During a normal glow discharge (ESD-NGD) under simulated Mars atmospheric composition and pressure (Wu et al., 2018), CO^{2+}, CO^{+}, O_I, H_{III}, H_{II}, *OH*, Ar_I, N_2, N_2^{+} were detected instantaneously as free radicals by *in situ* plasma emission spectroscopy. This does not exclude O_2, *NO, and* O^{+} because of the overlapping of plasma lines used for detection. O_3 was detected in the output gas by UV and mid-IR spectroscopy. Similarly, H_2O_2 and ·OH production were detected in a simulated saltation experiment on silicates upon contact of water (Bak et al., 2017). A study of CO_2 splitting (to CO and O_2) by dielectric barrier discharge was reported by Aerts et al. (2015).

These charged ions or excited neutral particles with high kinetic energy would react with the molecules in the martian atmosphere and in surface materials. As demonstrated by our previous work, these *multiphase redox plasma chemical reaction* (or simply *electrochemical reaction*) cause the oxidation of chlorine from chloride (Cl^{1-}) to chlorate/perchlorate (Cl^{5+} and Cl^{7+}) (Wu et al., 2018), and the release of Cl atoms at the first excited state (Cl_I) from common chlorides (Wang et al., 2020), instantaneously and apparently with high yields.

3. Samples and Experiments

3.1 Sample selection

To make our experiments relevant to the volatile portion (high wt% of SO_3 + Cl) of the X-ray amorphous component found on Mars (Dehouck et al., 2013; Morris et al., 2016; Morrison et al., 2018a; Rampe et al., 2017), we selected crystalline sulfates and chlorides as the starting phases for our ESD experiments. For the most part, hydrous salts were used, based on the association of H_2O with amorphous phases suggested by data analyses of SAM (Sutter et al., 2017, 2019). Salts with Mg, Fe^{2+}, Fe^{3+}, Ca, Al, Na, K were selected, based on the findings by recent missions of martian sedimentary minerals that were enriched in Mg and Fe, moderately enriched in Ca, and relatively depleted in Na and K (McLennan and Grotzinger 2008; McLennan, 2012; McLennan et al., 2019). A few relevant samples were added later, including two Na-sulfites, an Fe-sulfide (pyrite), and a Fe-hydroxide (akaganeite). These starting phases are listed in Table 1**.**

Each starting sample for an ESD experiment was ground and sieved. A grain size range of 63-88 µm was selected for all samples. Each powdered sample was placed into a fused-SiO_2 cell with an inner diameter of 22 mm and inner depth of 2 mm, i.e., about 760 mm^3 in volume. Depending on the density of different salts, a total mass of different salts in the range of 400-1100 mg was used. During each ESD experiment (Figure 1), the SiO_2 sample cell was placed in the lower electrode (Figure 1b), facing the energetic electrons from the upper electrode, and was entirely enveloped by the generated plasma (inset of Figure 1).

3.2 ESD experiments

We conducted all ESD experiments in a Mars environmental Chamber (Figure 1a, the PEACh, Planetary Environment and Analysis Chamber at Washington University in St. Louis, Sobron and Wang, 2012). The simulated atmospheric composition and pressure are regulated via a combination of needle and ball valves connecting the PEACh with a CO_2 gas tank. During an ESD experiment, the PEACh was first evacuated to 3×10^{-2} mbar to remove the air, and then it was filled with pure ultra-dry CO_2 for this study.

The atmospheric pressure, during an active evacuation and continuous CO_2 in-filling, was kept at 3 ± 0.1 mbar for all ESD experiments of this study.

As described by Sobron and Wang (2012), the temperature of the sample cell can be controlled by a liquid nitrogen (LN_2) delivery system attached to the PEACh (Figure 1). The LN_2, stored in a dewar outside the PEACh, is heated by a resistor immersed in the LN_2 reservoir, and the evaporated N_2 gas at near-LN_2 temperature is directed via a feedthrough in the PEACh's wall into a toroid-shaped, double-walled copper block (referred to as *the cold plate* hereafter) that sits inside the PEACh. Another feedthrough allows for the evacuation of the nitrogen gas after its circulation through the cold plate. An electronic controller (OMEGA Engineering Inc. CN76000 autotune controller) monitors the temperature of the cold plate via a resistive thermal device and regulates the flow of cold N_2 gas that enters the cold plate. This setup allows the temperature of the cold plate to be kept relatively constant at a desired temperature between 21°C and −100°C with deviations of less than 0.5°C.

Two parallel electrodes (made of copper, 35 mm diameter) were used in the PEACh for ESD experiments (Fig. 1b). The upper electrode (6 mm thickness) has a flat surface (top one in Figure 1b). The lower electrode (10 mm thickness) has a sample cup (bottom one in Figure 1b) that can hold the fused SiO_2 cell filled with powdered salts for this study. A motorized precision translation stage (Thorlab PTI-Z8) was used to fine-adjust the distance between the two electrodes. A distance of 6 mm was used in all experiments of this study.

Normal glow discharge (NGD) was generated in the experiments (insert of Fig. 1a). We used AC power (110 V, 50/60 Hz), a contact voltage regulator (No. 2090 VR), and a triggering neon power supply (CPI Advanced Inc., CPI-EZ12, max output 12 kV, 40 mA) that was directly connected to the ESD electrodes in the PEACh. We recorded electric voltage from the upper electrode to the ground, and electric current through the pair of ESD electrodes every 30 minutes during an ESD experiment, using two multimeters (KEYSIGHT-U1251B). Among different starting salt samples, we found very similar values of electric current (~ 22 mA) to those reported in Wu et al. (2018) and Wang et al. (2020), which gave the same electron flux density shown in Table S1.

The electron flux density in this experimental setting is 1.42×10^{20} $s^{-1}m^{-2}$, calculated from the electric current measurement (Table S1). Thus the ESD process in our experimental setting has a strength midway between the two extreme cases, ESD-TDD and ESD-NGD, that range from 9×10^{16} $s^{-1}m^{-2}$ (TDD) to 1.5×10^{24} $s^{-1}m^{-2}$ (NGD) (detailed discussion in section 5.3 of Wu et al., 2018). The energy of electrons generated in our ESD experimental setting can be estimated using the observed free radicals. For example, CO_2^+ was the dominant species generated by ESD in CO_2, (Figure 4a, b, c, and Table 1 of Wu et al., 2018) and it is a product of electron impact ionization (EII) of CO_2 (Delory et al., 2006; Jackson et al., 2010). The occurrence of EII of CO_2 revealed that a considerable portion of electrons generated in our ESD experimental setting has a kinetic energy >14 eV. Furthermore, a very strong Hα line at 656.3 nm was observed by *in situ* plasma spectroscopy at extremely low P_{H2O} (Fig. 4b, d, e of Wu et al., 2018) or when the starting mineral is hydrous salt. This line is generated by a transition from H_{III} to H_{II} that indicates the presence of electrons with energy > 17.19 eV (Delory et al., 2006, Itikawa and Mason 2005).

Specifically for this investigation, we used the cold plate to control the temperature of some starting salts during ESD so that is was lower than 30°C to avoid sample melting (melting point (MP) in Table 1, based on Lide 2001). The cold plate in the PEACh is electrically grounded, as well as the PEACh itself. On the other hand, the lower electrode must be isolated electrically from the cold plate; this was satisfied by using a Teflon holder between the lower electrode and the cold plate. The holder is thin enough (1.59 mm) to allow the temperature (T) of the lower electrode to be thermally controlled by the cold plate. A thermocouple was inserted into a tunnel of 0.79 mm diameter in this Teflon holder to measure the T of the lower electrode while keeping its electric isolation from the cold plate.

During an ESD process in the PEACh, the equilibrated temperature T_{eq} of the lower-electrode sample cell was normally reached after > 30 minutes. For most hydrous S and Cl salts with melting-point temperatures above 130°C, we do not use LN_2 cooling. The resulting T_{eq} is in the range of 80-105°C (Figure 2). For a few selected salts (e.g., $FeSO_4 \cdot 7H_2O$ and some hydrous chlorides, Table 1), the ESD experiments were run using LN_2 to cool the cold plate and generate a T_{eq} in the range of 10-30°C, with the exact T_{eq} value depending on the type of salt (Figure 2).

3.3 Analyses of ESD reaction products

Almost all sulfates and chlorides show a color change after an ESD process of certain time duration (e.g., 7 hours, Table 1) under Mars conditions. For example, the photos in Figure 3 (a, b) are $MgCl_2 \cdot 6H_2O$ before and after 7h ESD, shown with different magnifications (Figure 3b, c, d). The color change only appears at the surface of ESD products, consistent with our previous finding of surface enrichment of ESD-generated species ($NaClO_3$ and $NaClO_4$, when using NaCl as the starting phase) from Ion Chromatography (IC) analyses of the layers in the ESD-product (Figure 6b of Wu et al., 2018). Both color change and IC data suggest that the electrochemical reaction induced by ESD in a Mars chamber is an atmosphere-to-surface interaction, i.e., the *as is* surface of an ESD product should be the best sampling site for the characterization of new species generated by ESD.

We used laser Raman spectroscopy (Raman), X-ray diffraction (XRD), Vis-Near-IR spectroscopy (VNIR), Mössbauer spectroscopy (MB), and Ion Chromatography (IC) to characterize the ESD products in this study. Among them, Raman and VNIR measurements were made on the *as is* surface. In particular, all micro-beam Raman analyses were made directly on the spots that show color changes, which were selected under the microscope of our Raman system. On the other hand, the field of view (FOV) of the VNIR probe matches well with the size of the SiO_2 cell that contains the ESD product, so a VNIR spectrum was taken from the whole *as is* surface of the ESD product. For XRD and Mössbauer analyses, the bulk powder sample from the full depth of the SiO_2 cell of an ESD product was re-ground and used. Bulk powder samples were also used for IC analyses. All these analyses were taken at room temperature.

Raman spectra of all samples were collected using a Renishaw inVia Raman system, with 532 nm excitation wavelength, spectral range of 50-4300 cm^{-1} and spectral resolution better than 1 cm^{-1}. A 50× long-working-distance objective was used that generates an ~ 1 µm beam diameter at laser focus. Raman analysis of each ESD product was always taken on multiple spots in several areas at the *as is* surface of a sample, with a total of > 30 (at least) spectra per sample. A laser beam energy of 5 mW was normally used for the measurements of ESD products from Mg, Ca, and Na salts. A much lower laser energy (0.5-0.05 mW) was used on the ESD products from Fe-bearing salts. The Raman spectrometer is calibrated during each working day to keep the accuracy and precision of Raman peak positions within ± 0.5 cm^{-1}.

The VNIR spectra of the ESD products were acquired using Analytical Spectral Devices (ASD) FieldSpec4 spectroradiometer (Malvern Panalytical Company) with a contact probe. The obtained spectrum covers a wavelength range of 0.35 to 2.5 µm, with spectral resolution of 3 nm @ 700 nm and 10 nm @ 1400/2100 nm. A Spectralon target was used for absolute reflectance calibration before the sample measurements. The VNIR spectra were taken directly on the *as is* surface of an ESD product that matches with the full FOV of the VNIR probe. The recording time of each spectrum was 1 second, and at least two spectra were taken from each sample for redundancy.

XRD measurements were made using a Bruker D8 Advance diffractometer with CuKα radiation (λ = 1.54052 Å) at 40 kV and 40 mA and a collecting angle of 3° was used for phase identification. Each sample was ground again to fine powder and held by a MTI zero background silicon holder. A 0.02° step size, 1 second dwell time, and 15 rotation per minute for the sample holder were used to record the XRD pattern in a 4° to 60° 2θ range. The Bruker XRD has a guaranteed calibration that is confirmed during installation and monitored by analysis of a NIST SRM 1976a Al_2O_3 standard. The alignment is also guaranteed and has been demonstrated to be within 0.03° 2θ of the absolute peak position of the NIST SRM.

Mössbauer spectral measurements were made on the ESD products from a few Fe-bearing phases. Each sample was gently mixed with sugar and then heaped in a sample holder confined by Kapton® polyimide tape. Mössbauer spectra were acquired at 295 K using a source of ~80 mCi ^{57}Co in Rh on a SEE Co. (formerly WEB Research Co.) model WT302 spectrometer at Mount Holyoke College. For each sample, the fraction of the baseline due to the Compton scattering of 122 keV gammas by electrons inside the detector was determined by measuring the count rate with and without a 14.4-keV stop filter (~2 mm of Al foil) in the gamma beam. Compton-corrected absorption was calculated for each individual spectrum using the formulation A/(1 - b), where b is the Compton fraction and A is the uncorrected absorption. This correction does not change the results of the fits per se but does allow accurate determination of % absorption in the spectra. It is necessary because the range of energy deposited in the detector by Compton events extends from 0 keV to 40 keV, overlapping both the 14 keV and 2 keV energies deposited by the 14 keV gammas.

The run time of each Mössbauer measurement was ~24 hours. Spectra were collected in 1024 channels and corrected for nonlinearity via interpolation to a linear velocity scale, which is defined by the spectrum of the 31 μm Fe foil used for calibration. The WMOSS algorithm fits a straight line to the points defined by the published values of the Fe metal peak positions (as *y* values) and the observed positions in channels (*x* values). Data were then folded before fitting, using the WMOSS Auto-fold procedure that folds the spectrum about the channel value that produces the minimum least squares sum difference between the first half of the spectrum and the reflected second half of the spectrum.

Ion chromatography was used to quantify the SO_4 production from ESD experiments using Na_2SO_3 and $NaHSO_3$ as starting salts. A 15-20 mg homogenized sample was dissolved in N_2-purged milliQ water and analyzed by ion chromatography using an A-Supp7-250 anion column (45◦C, 3mM Na_2CO_3 eluent, 0.8mL/min, with suppression) on a Metrohm 881 Compact IC pro with a conductivity detector. Five standards were prepared from pure Na_2SO_4 from Sigma-Aldrich at concentrations of 1.3 ppm, 10.6 ppm, 20.3 ppm, 51.4 ppm, and 100.6 ppm, which generated a calibration line with R^2 value of 0.9954. The detection limit for sulfate by IC analysis was 0.1 ppm. The concentration in solution (in ppm) is then converted to ppm in the solid (mg SO_4/kg sample). Due to the rapid oxidation of sulfite in solution to sulfate under ambient laboratory conditions, the sample solutions were analyzed immediately after preparation to minimize oxidation during sample handling. The stability of sulfite was tested by comparing the concentration in the freshly prepared solutions and the same solution after sitting in air for 1 hour. Slight oxidation occurs even in this short time; therefore, the error of these measurements is estimated as the standard deviation between these two replicate measurements and was found to be on average 0.6 ppm in solution. This equates to a conservative estimate of ~350 ppm error in the solid, although samples were prepared and analyzed within ~20 min.

4. Analyses of the ESD products from S and Cl salts

4.1 ESD products from Mg, Fe^{2+}, Fe^{3+}, Ca, Na sulfates and sulfites

4.1.1. ESD products from $MgSO_4 \cdot xH_2O$ (x=1, 4, 7)

As listed in Table 1, 0.25h, 1h, 2h and 7h ESD experiments were carried out on $MgSO_4 \cdot xH_2O$ (x=1, 4, 7) powder. The ESD product from each experiment was analyzed using Raman on multiple spots of an *as is* surface and using XRD on the bulk sample (from the full depth of the SiO_2 cell).

Raman spectra in Figure 4a are from 36-spot analyses on the *as is* surface of a 0.25h-ESD product from epsomite $MgSO_4 \cdot 7H_2O$. Data from the shortest ESD duration (0.25 hour) were purposely presented to show the intermediate species generated during the ESD process. In a Raman spectrum of sulfate, the fundamental vibrational modes (ν_1, ν_2, ν_3, and ν_4) of SO_4 unit are located in four spectral regions centered around ~ 1000, 500, 1150, and 600 cm^{-1}, often with multiple peaks for each mode. Among the ν_1 Raman peaks near 1000 cm^{-1} in Figure 4a, the strongest sharp peak at 1000 cm^{-1} belongs to a crystalline starkeyite $MgSO_4 \cdot 4H_2O$ (4W), a weak sharp peak at 983 cm^{-1} belongs to a crystalline $MgSO_4 \cdot 6\text{-}7H_2O$ phase (6-7 W) (983.6 cm^{-1} for $MgSO_4 \cdot 6H_2O$ and 984.1 cm^{-1} for $MgSO_4 \cdot 7H_2O$, Table 3 of Wang et al., 2006), the broad peaks (from all sampling spots) centered ~1030 cm^{-1}, ~600 cm^{-1} and ~500 cm^{-1} (marked as "Amor") demonstrate the initiation of amorphization (based on Figure 20 of Wang et al., 2009). Figure 4b shows an overlay of the Raman spectra from a 37-spot analysis of the same 0.25h-ESD product in 3876 - 3072 cm^{-1} spectral range. The occurrence of H_2O peaks from each sampling spots indicates retention of structural H_2O in ESD product, i.e., $MgSO_4 \cdot 7H_2O$ is partially dehydrated.

Raman spectra in Figure 4 reveal a fast dehydration from epsomite $MgSO_4 \cdot 7H_2O$ to crystalline starkeyite (4W) at least, and the initiation of amorphization. Experimental study of hydrous Mg-sulfates (Wang et al., 2009) revealed that amorphous $MgSO_4 \cdot xH_2O$ can hold up to three structural H_2O per $MgSO_4$ molecule, consistent with the observation of H_2O Raman peaks of different shapes from all sampled spots on the *as is* surface (Fig. 4b).

Amorphization in epsomite $MgSO_4 \cdot 7H_2O$ developed very fast with increased ESD time duration. After 1 hour of ESD processing in the PEACh, almost no crystalline Mg-sulfates can be detected in the fundamental vibrational spectra range (not shown, but similar to Figure 5a). On the other hand, a trace of the H_2O peak still remains (not shown) after 7h ESD process on epsomite. In other words, full amorphization was reached but the full dehydration was not reached at the *as is* surface.

Total amorphization at the *as is* surface was reached after 1.5 h of ESD process on crystalline starkeyite $MgSO_4 \cdot 4H_2O$. As seen in Figure 5a, amorphization is characterized by (1) shift of the ν_1 peak from 1000 cm^{-1} to ~ 1030 cm^{-1}, (2) broadened peak width for every peak in the whole spectrum and in every spectrum from all sampled spots, (3) merged peaks of ν_2, ν_4, and the lattice modes (below 400 cm^{-1}) into three large spectral envelopes, and (4) severely reduced S/N ratio (because the Raman peak intensity of non-crystalline phase is 1-2 order of magnitude weaker than that of crystalline phase with similar composition, White 1975) which also appeared as a raised spectral background. In Figure 5b, the structural damage of a crystalline kieserite $MgSO_4 \cdot H_2O$ by a 1.5h ESD are presented by (1) broadened peak widths, (2) loss of minor peaks, and (3) reduction of S/N, but to a lesser degree when compared with Figure 5a from crystalline starkeyite of 1.5h ESD.

XRD measurements made on the bulk ESD products from $MgSO_4 \cdot xH_2O$ (x=1, 4, 7) are shown in Figure 6. Both XRD patterns on the top of Figure 6 have a raised "hump" from 10° to 40°(2θ), which can be fitted with three wide "bands", centered at 14.2°, 21.9°, and 28.0° with widths of 5.4°, 11.4°, and 11.5°, respectively. A few sharp XRD lines remain on the top of the "hump"; some can be assigned as crystalline $MgSO_4 \cdot H_2O$ (1w) or $MgSO_4 \cdot 4H_2O$ (4w), with some lines unassigned since hydrous Mg-sulfates can have eight different hydration degrees. The difference in the degrees of amorphization seen in XRD patterns (Fig. 6) and Raman spectra (Fig. 5a) is caused by the sampling differences of the two analyses, with XRD sampled the bulk sample (from full depth of SiO_2 cell) and Raman sampled the *as is* surface only.

The third XRD pattern in Figure 6 is obtained from the 1.5h-ESD product from kieserite $MgSO_4.H_2O$ (8.5h-ESD product has the same pattern). When compared with the standard XRD pattern of kieserite, the 1.5h-ESD product has a broadened line width for every line in the whole XRD pattern. In addition, the multiple lines in the line groups at 25-30°, 35-40°, ~44°, and 55-60° 2θ ranges are merged into envelopes with non-symmetric shape. XRD standard 00-001-0638 (kieserite, $MgSO_4 \cdot H_2O$, monoclinic) and 00-037-009 (caminite $Mg_2(SO_4)_2 \cdot 2H_2O$, tetragonal) in the PDF database have lines that may contribute the merged line groups of the ESD product (Fig. 6). The observed XRD line widening and merging of line clusters suggest a heavily distorted crystal structure in the ESD product from kieserite, suggesting development of amorphization caused by the impact of energetic electrons and by the reaction with free radicals generated in the ESD process. This conclusion is consistent with Raman observations from Figure 5b.

Overall, the effects of ESD processes on hydrous Mg sulfates are dehydration and amorphization. The higher the hydration degree in an original salt, the higher the rate of amorphization by the ESD process, a phenomenon that we also observed for other salts in this study.

4.1.2. ESD products from FeSO4.xH2O (x=1, 4, 7)

The melting point of melanterite $FeSO_4 \cdot 7H_2O$ is 60°C (Lide 2001, Table 1). So the ESD experiment of melanterite was made with LN_2 temperature control, $T_{eq} < 30°C$ (Figure 2), and durations of 0.25h, 1h, 3h, and 7h. ESD products were analyzed by Raman and VNIR on the *as is* surface, and by XRD and Mössbauer on bulk samples. Very low laser power (0.5 mW) was used in Raman measurements to avoid overheating of these Fe-bearing phases by the laser beam, which was confirmed by visual inspection under the Raman microscope before and after each scan.

Raman spectra Figure 7 (a, b) shows the overlay of the first 60 Raman spectra from the 0.25h ESD and 7h ESD products. The obtained spectra from the 0.25h ESD product are compared in Figure 7a with the standard Raman spectra of $FeSO_4 \cdot xH_2O$ (x=1, 4, 7, Choi et al., 2007). The ν_1 mode of rozenite $FeSO_4.4H_2O$ (4w) and szomolnokite $FeSO_4 \cdot H_2O$ (1w), 1018 cm^{-1} and 990 cm^{-1}, appeared after a 0.25 hour ESD process, while the Raman peaks of melanterite $FeSO_4 \cdot 7H_2O$ (7w) disappeared i.e., a total destruction of melanterite by 0.25h-ESD. The only unassigned Raman peak in Figure 7a is at 1035 cm^{-1} (marked by red arrow), which is an indication of early development of amorphization (Fig. 7 of Ling and Wang, 2010), similar to the case of $MgSO_4 \cdot 7H_2O$ after 0.25h-ESD (Fig. 4a). The peak position at 1035 cm^{-1} suggests an amorphous phase $Fe^{3+}_2(SO4)_3 \cdot 5H_2O$ (based on Fig. 18 of Wang and Ling 2011). Because of the different T_{eq} achieved by ESD processes on epsomite and melanterite (Fig. 2), a direct comparison of the amorphization rate cannot be extracted for these Mg, Fe-sulfates.

Figure 7b shows the first 60 spectra from a 120-spots Raman scan on the *as is* surface of 7h ESD product from melanterite, which revealed the abundant amorphization in the product. The center of strongest peak moves to near 1075 cm^{-1} (Fig. 7b), shown as a large envelop that merged the multiple peaks of ν_1 and ν_3 modes of SO_4 unit together (the merge of ν_1 and ν_3 was less obvious in Mg-sulfates, Fig. 5, 6). Peaks of the ν_2, ν_4, and lattice modes are also merged into three large envelopes around 610, 470, and 240 cm^{-1}, respectively, with severely reduced S/N ratio. The ν_1 peak of crystalline szomolnokite $FeSO_4 \cdot H_2O$ (1w) at 1018 cm^{-1} remains in some spectra.

Raman spectra obtained from a scan on the 1.5h-ESD product from rozenite $FeSO_4 \cdot 4H_2O$ are shown in Figure 8a. The strong and wide envelope spanning 1300 to 950 cm^{-1} represents a merge of ν_1 and ν_3 modes of SO_4 unit, with the sharp ν_1 peak of $FeSO_4 \cdot H_2O$ remaining in some spectra. The other three wide envelopes (below 1000 cm^{-1}) are from the merged peaks of ν_2, ν_4, and lattice modes respectively, similar to 7h ESD products from melanterite (Fig. 7b). H_2O peaks centered at 3430 cm^{-1} were detected at almost all sampled spots on the *as is* surface (Fig. 8a), suggesting that full dehydration was not reached.

Very sharp Raman peaks remained in all spectra from the ESD products of szomolnokite $FeSO_4 \cdot H_2O$ (1w), even after 15.5h-ESD (Fig. 8b). When compared with the standard spectra of various ferrous and ferric sulfates, we found that the best match was with $Fe^{3+}OHSO_4$. The transformation from $Fe^{2+}SO_4 \cdot H_2O$ to $Fe^{3+}OHSO_4$ demonstrated the occurrence of oxidation ($Fe^{2+} \rightarrow Fe^{3+}$) and hydrolysis caused by the ESD process. The major peak at 1094 cm^{-1} of $Fe^{3+}OHSO_4$ was also observed at some sampled spots (hidden in the spectral overlay of Fig. 8a) on the *as is* surface of 1.5h-ESD product from rozenite $FeSO_4 \cdot 4H_2O$.

XRD measurements were made on the bulk samples of ESD products from $FeSO_4 \cdot xH_2O$ (x = 1, 4, 7). Figure 9 shows the XRD pattern from the 7h ESD product from melanterite $FeSO_4 \cdot 7H_2O$ and from szomolnokite $FeSO_4 \cdot H_2O$. The top XRD pattern in Figure 9 overlays the characteristic XRD lines of $FeSO_4.H_2O$ onto two large XRD "humps", centered at 11.4° and 27.5° that are similar to the humps in Figure 6, but slightly narrower in widths, 5.4° and 9.0°. This XRD pattern reveals a partially amorphous bulk sample. The XRD pattern from the 1.5h-ESD product from $FeSO_4 \cdot 4H_2O$ (not shown) has strong lines of crystalline rozenite and szomolnokite. The partial amorphization observed in Raman data (Fig. 8a) appears less obvious in XRD data, likely because a bulk sample from full depth of ESD product in the SiO_2 cell was used for XRD. The XRD pattern (2^{nd} in Fig. 9) from the 1.5h-ESD product from $FeSO_4 \cdot H_2O$ has the major lines of butlerite $Fe^{3+}OHSO_4 \cdot 2H_2O$ and $Fe^{3+}OHSO_4$, in addition to the remaining lines of $FeSO_4 \cdot H_2O$. The appearance of butlerite and dehydrated butlerite indicate the oxidation of Fe^{2+} to Fe^{3+}, and hydrolysis caused by ESD processes, consistent with Raman observations (Fig. 8b).

VNIR spectra (Fig. 10) were taken at the *as is* surfaces of 0.25h, 1h, 3h, and 7h ESD products from $FeSO_4 \cdot 7H_2O$ (T_{eq} < 30°C, Fig. 2). The first major spectral change with increasing ESD time is a decrease in absorption band depth near 1.0, 1.4, and 1.9 µm, suggesting gradual dehydration. Indeed, the narrow and strong VNIR doublet near 1.9 µm of the 0.25h-ESD product can be assigned to $FeSO_4 \cdot 4H_2O$ (Fig. 3 of Wang et al., 2016), and the much wider and weaker doublets (near 1.9 µm) in the spectra of the 1h, 3h, 7h ESD products are similar to the doublet of $FeSO_4 \cdot H_2O$ (Fig. 6 of Wang et al., 2016). The second major spectral change is a gradual decrease of spectral contrast, which is especially obvious in the spectrum of 7h ESD product. This phenomenon reflects the destruction from a crystalline structure, consistent with Raman and XRD observations. Notice a weak but characteristic VNIR spectral pattern of $FeSO_4 \cdot H_2O$ (Fig. 10) was obtained from the 7h ESD product, while on the same *as is* surface, a multi-spot Raman scan shows almost total amorphization; only a few spots retained the 1018 cm^{-1} peak of szomolnokite (Fig. 7b). This phenomenon shows that the sensitivities of Raman and VNIR spectra for detecting structural damage are different. A previous study using XRD, Raman, Mid-IR, and VNIR on a set of saponite samples with different degrees of amorphization revealed that VNIR spectroscopy is less sensitive to the loss of crystallinity. From the saponite samples that show totally non-crystalline XRD patterns, sharp VNIR spectral peaks can still be seen at 1.4 µm, 1.9 µm and especially in the 2.2-2.4 µm spectral range (Fig. 1, 2 of Fu et al., 2017).

A *Mössbauer spectrum* was obtained from 59 mg of the powdered bulk 7h ESD product from $FeSO_4 \cdot 7H_2O$. The measured spectrum was fit in a variety of ways using two different programs. The Mex_disdd solves the full hyperfine interaction Hamiltonian and minimizes the difference between modeled line shape independent peaks and the experimental spectrum using center shift, quadrupole splitting, and linewidth as variable parameters. Disd_3e makes velocity approximations rather than solving the full interaction Hamiltonian and uses a range of line-shape-independent quadrupole splitting distributions (QSD) to build the peaks. Because the peaks in these spectra overlap heavily and it is difficult to prioritize one model over the other, so both are shown and reported (Figure 11a, b). In both models, there are two Fe^{3+} and three Fe^{2+} distributions. Parameters are given in Table 2; errors on total $\%Fe^{3+}$ are ±1-5 % absolute based on repeated fits to the same spectra, with a detection limit for Fe^{3+} of roughly 1%. Although it is known that differential recoil-free fraction (*f*) effects can affect the assumption that Mössbauer peak area directly represents the proportions of Fe in each site or valence state, *f* has not been determined for these materials. Thus, this paper assumes that recoil is the same for both Fe^{2+} and Fe^{3+}. Based on Mössbauer analysis, we obtained a Fe^{3+}/Fe_{total} ratio of 44% in analyzed sample.

This result indicates a strong oxidation has occurred during ESD process on melanterite $FeSO_4 \cdot 7H_2O$. This conclusion is visually confirmed by the color change of the samples, from light green of $FeSO_4 \cdot 7H_2O$, to light yellow, to light brow, and finally to dark brown after 7h ESD, suggesting more oxidized iron (Fig. S1). The amorphization development in 7h ESD product from $FeSO_4 \cdot 7H_2O$ may be reflected in the details of Mössbauer parameters, e.g., CS = 1.21-1.29 mm/s and QS = 1.55-2.66 mm/s, which are different from the ranges in literature for $FeSO_4 \cdot xH2O$ (x=1, 4,7), 1.16-1.31 mm/s for CS and 3.17-3.24 mm/s for QS (Cheetham et al., 1981; Dyar et al., 2013; Eissa et al., 1994a,b; Grant et al., 1966; Montano; 1981; Sakai et al., 1981; Sallam et al., 1994).

Overall, the effects of ESD processes on hydrous Fe^{2+} sulfates are dehydration, amorphization, and oxidation from Fe^{2+} to Fe^{3+}.

4.1.3. ESD products from ferric sulfates

Given the importance of Fe^{3+}-bearing phases for Mars surface mineralogy, we conducted ESD experiments in the PEACh on four Fe^{3+}-bearing species, Na-jarosite $NaFe_3(OH)_6(SO_4)_2$, ferricopiapite $Fe_{4.67}(SO_4)_6(OH)_2 \cdot 20H_2O$, akaganeite FeO(OH,Cl), and pyrite FeS_2 (Table 1).

4.1.3.1. ESD products from ferricopiapite

Figure 12 shows a typical Raman spectra obtained from ESD products of ferricopiapite $Fe_{4.67}(SO_4)_6(OH)_2 \cdot 20H_2O$, with the ESD durations of 0.25h, 1h, 2h, 3h, and 7h. When compared with Raman spectra of standard ferric sulfates (Fig. 12a, from Ling and Wang, 2010), we found the spectra from the 0.25h-ESD product can be assigned to ferricopiapite (#1 in Fig. 12b), rhomboclase $FeH(SO_4)_2 \cdot 4H_2O$ (#2 in Fig. 12b), and a phase whose most peaks are similar to those of ferricopiapite in positions and shapes, except its strongest ν_1 peak at 1018 cm^{-1} (#3 in Fig. 12b) that can be regarded as a merged ferricopiapte doublet, with an upper-shifted peak center. Forming acidic rhomboclase from basic ferricopiapite is also a dehydration process with N_{H2O}/N_{SO4}=3.67 → 2. The shifting of ν_1 peak position to higher wavenumber is normally an indication of dehydration, observed in the Raman spectra of hydrous Mg, Fe^{2+}, and Ca sulfates. The merge of the doublet suggests a damaged crystal structure, i.e., an early step towards the amorphization.

Typical Raman spectra from #4 to #8 in Figure 12b obtained from 1h, 2h, and 7h ESD products all have the strong and wide peak in ν_1 spectral range, but the central position of this peak gradually shifted towards higher wavenumber (indicated by a dotted arrow line in Fig. 12b), from 1018 cm^{-1} to 1057cm^{-1} (#3 to #8 in Fig. 12b). This peak shift is accompanied by the loss of details for all peaks below 800 cm^{-1}, which eventually become three wide envelopes centered around ~650 cm^{-1}, ~480 cm^{-1}, and ~250 cm^{-1} (spectrum #4, #5, #6, #7, #8). These are typical Raman spectral pattern of amorphous ferric sulfates (#3 in Fig. 12a). Wang and Ling (2011) built a calibration curve (their Fig. 18) to quantify the number of structural H_2O per $Fe_2(SO_4)_3$ unit, from eleven to five, using the ν_1 peak position of amorphous ferric sulfates (from 1022 to 1035 cm^{-1}). Although there are no other experimental studies of amorphous ferric sulfates with structural water less than five, an educated guess is that the continuous ν_1 peak upper shift from 1035 cm^{-1} to 1057 cm^{-1} (Fig. 12b) is due to continuous dehydration from five to zero structural waters per $Fe_2(SO_4)_3$ unit, based on the assignment of spectra #9 and #10 in Figure 12b.

Spectra #9 and #10 (Figure 12b) were obtained from many Raman sampled spots on the *as is* surface of the 7h ESD product from ferricopiapite. Spectrum #10 is a perfect match with the standard Raman spectrum of crystalline anhydrous $Fe_2(SO_4)_3$ (#4 in Fig. 12a), and spectrum #9 is a mixture of standard spectra of two polymorphs, the anhydrous $Fe_2(SO_4)_3$ and mikasaite $Fe_2(SO_4)_3$ (#5 in Fig. 12a), both are crystalline materials (Ling and Wang 2010). The multi-spots Raman scans revealed that crystalline anhydrous $Fe_2(SO_4)_3$ appeared early in ESD products (e.g., 1h-ESD) and became abundant in the ESD product with longer time duration (e.g., 7h ESD).

Overall, the major effect of ESD process on ferricopiapite is dehydration, from N_{H2O}/N_{SO4}=3.67 to N_{H2O}/N_{SO4}=0. The ESD caused structural change is complicated, from crystalline to full amorphization, then back to crystalline again. During the early dehydration, the ferric sulfate also changed from basic ferricopiapite to acidic rhomboclase.

4.1.3.2. ESD products from Na-jarosite, akaganeite, and pyrite

It is quite surprising that no obvious mineral transformation occurred in Na-jarosite after long duration ESD processes (even after 64 hours). The post-ESD sample surface color shows an obvious darkening (Fig. S2). The peaks of hematite appeared in the spectra from some spots in multi-spots Raman scans. However, 99% of Raman spectra obtained from the *as is* surfaces of eight ESD products from Na-jarosite maintain an almost perfect match with the Raman spectrum of the original Na-jarosite (Fig. S3). The Mössbauer spectrum of this post-64h ESD product revealed a set of typical CS and QS for Na-jarosite (Fig. S4).

Considering the importance of jarosite in martian surface mineralogy, we made two sets of 1:1 mixtures of Na-jarosite with $MgSO_4 \cdot 7H_2O$ and $MgCl_2 \cdot 6H_2O$, and did ESD on them, with a goal to study a potential catalysis effect. Again, no obvious mineral phase transformation was observed by Raman spectroscopy in the products from two additional sets of eight ESD experiments (Table 1, 2), except the spectrum of hematite was seen from some spots in the Raman scans on these ESD products. The Mössbauer spectra of the 7h ESD products from the two mixtures (not shown) support ~ 100% jarosite among the Fe-phases in bulk samples.

Similar to Na-jarosite, no obvious mineral transformation was found by Raman and Mössbauer analysis of the post-ESD products from akaganeite $Fe^{3+}O(OH,Cl)$ (Fig. S5). On the other hand, Raman scans on post-ESD products from a natural pyrite show minor changes in Raman peak positions and shapes (Fig. S6). However, the XRD pattern of the 14h ESD product from this natural pyrite does show an obvious change from standard pyrite, thus it cannot be compared with Raman spectra to suggest any significant phase transformation.

4.1.4. ESD products from Na_2SO_4

The Raman spectra obtained on the *as is* surface of the 7h ESD product from Na_2SO_4 powder have only minor changes from the standard spectrum (Fig. 13), such as the slight peak broadening of Raman ν_1 mode near 992 cm^{-1} (insert of Fig. 13), and slightly raised spectral background after 400 cm^{-1}. The broadening of the Raman peak indicates a damaged crystalline structure from original Na_2SO_4. XRD measurements were not made on this sample.

4.1.5. ESD products from $CaSO_4.2H_2O$

The Raman spectra (Fig. 14) obtained on the 7h ESD product of $CaSO_4 \cdot 2H_2O$ powder revealed the transformation from gypsum to γ-$CaSO_4$ phase (not anhydrite α-$CaSO_4$) mainly, that has a sharp peak at 1026 cm^{-1} shown in the insert of Figure 14. Ordinary γ-$CaSO_4$ would not be stable at ambient terrestrial laboratory conditions. The post-ESD product from $CaSO_4 \cdot 2H_2O$ was sealed in a glass vial, with the Raman measurements made through the glass wall. In addition to γ-$CaSO_4$, bassanite $CaSO_4 \cdot 0.5H_2O$ was identified in some sampled spots (peak at 1014 cm^{-1} in the inset of Fig. 14), that is also supported by the observations of structural H_2O peaks in Raman spectra (not shown) of some sampled spots. No XRD measurement was made on this sample. It is notable that a large amount of γ-$CaSO_4$ was found to be stable within the vein system of martian meteorite MIL03346 (Ling and Wang, 2015), as well as in soils of hyperarid regions on Earth, such as from the Atacama Desert (Wei et al., 2015) and the saline playa on the Tibet Plateau (Wang et al., 2018). The γ-$CaSO_4$ phase apparently can exist stably under ambient terrestrial laboratory conditions. We are currently investigating the structural and chemical reasons for the abnormal stability of the γ-$CaSO_4$.

4.1.6. <u>ESD products from Na_2SO_3 and $NaHSO_3$</u>

In order to evaluate the oxidation power of ESD processes on S-bearing species, we selected two sulfites, $Na_2S^{4+}O_3$ and $NaHS^{4+}O_3$, as the starting phases for a set of ESD experiments with 0.25h to 11h duration (Table 1).

Among the obtained Raman spectra from 252 spots-scan on the *as is* surface of 7h ESD product from Na_2SO_3, about ~ 12% has an additional peaks at 997 cm^{-1} (insert of Fig. 15). On the other hand, all Raman spectra from a total of 188 spots-scan on the *as is* surface of the 7h ESD product from $NaHSO_3$ has the additional peak at 997 cm^{-1} (not shown). Besides, this peak position does not match with the ν_1 peak of Na_2SO_4 at 993 cm^{-1} (insert of Fig. 15). XRD measurements were made on both sulfites. The XRD pattern of the 7h ESD product of $NaHSO_3$ is different from that of original sample (#1 in Fig. 16). After the 7h ESD process, new XRD lines appeared, and multiple lines merged in four regions (22-30°, 31-37°, 46-50°, and 57– 61° 2θ), suggesting structural damage of $NaHSO_3$. In addition, XRD standards 00-037-1488 ($Na_2S^{4+}O_3$), 04-015-3684 ($Na_2S^{4+}{}_2O_5$), and 00-021-1371 ($Na_2S^{6+}{}_3O_{10}$) in PDF database (#2, #3, #4 in Fig. 16) have lines that might contribute the merged line groups that appear in the top XRD pattern of Figure 16. The potential contribution of $Na_2S^{6+}{}_3O_{10}$ (#4 in Fig. 16) to the merged line groups provides a hint for the oxidation of S^{4+} to S^{6+}.

Oxidation of sulfite ($S^{4+}O_3^{-2}$) to sulfate ($S^{6+}O_4^{-2}$) through the ESD process was finally established using the Ion Chromatography (IC) analyses of 1h, 3h, 7h ESD products from Na_2SO_3 (dissolved in N_2-purged milliQ water and immediately analyzed by IC), shown in Figure 17. The time series shows a gradual increase as a function of ESD experimental duration, from 1 hour to 7 hours.

4.2. Analyses of the ESD products from Mg, Fe, Ca, Al, Na, K- Chlorides

We conducted ESD experiments on six chlorides (Table 1), two anhydrous (NaCl and KCl) and four hydrous (Mg-, Fe^{2+}-, Ca-, Al-chlorides). This selection was made on the basis of their potential existence in anhydrous or hydrous forms on Mars and their stable existence at ambient laboratory conditions making them experimentally feasible. Three hydrous chlorides (Mg-, Fe^{2+}-, Al-) among them have melting points T_{mp} below 100°C (Table 1); thus we ran the ESD experiments on these chlorides with LN2 temperature control with equilibrated temperature T_{eq} < 30 °C (Fig. 2).

<u>4.2.1. ESD products from $FeCl_2.4H_2O$</u>

Figure 18 shows typical Raman spectra obtained from the *as is* surfaces of 0.25h, 1h, 3h, and 7h ESD products from $FeCl_2{\cdot}4H_2O$. Spectral features from most spots on 0.25h-ESD product remained similar to those of crystalline chlorides, with an additional sharp Raman peak at 334 cm^{-1} (#2 in Fig. 18) The major H_2O peak at 3406 cm^{-1} and a peak-shoulder at 3445 cm^{-1} (not shown) suggest a change of hydration degree from $FeCl_2{\cdot}4H_2O$ to probably $FeCl_2{\cdot}2H_2O$. After 1h ESD, Raman peaks began to broaden (#3 in Fig. 18). In addition, an overall Raman spectral shape very similar to that of hematite $Fe^{3+}{}_2O_3$ occurs frequently after 3h ESD (#4 in Fig. 18). After 7h ESD, a few sampled spots have a peak near 395 cm^{-1} (#5 in Fig. 18) that is the major Raman peak of goethite, $Fe^{3+}OOH$, but most spots have extremely broad Raman "humps" near 1310, 710, and 300 cm^{-1} (#6 in Fig. 18). The H_2O peak in the 3300-3700 cm^{-1} range becomes wide and weak, to almost nonexistent (not shown). Overall, this set of spectra revealed a progressive loss of crystallinity, oxidation ($Fe^{2+} \rightarrow Fe^{3+}$), and dehydration.

The XRD pattern obtained from this 7h ESD product from $FeCl_2{\cdot}4H_2O$ (Fig. 19) has three "humps" in 2θ ranges of 8-18°, 23-41°, and 45-60°, with broadened lines on top of the humps. These XRD lines match with $FeCl_2{\cdot}2H_2O$ (pdf: 00-025-1040), $FeCl_2$ (pdf: 00-001-1106), and $Fe^{3+}OCl$ (pdf: 00-039-0612) (#1, #2,

#3 in Fig. 19), but have much wider linewidth and merged line groups. Therefore, XRD data supports the inferences of amorphization, oxidation, and dehydration that are based on Raman analysis.

The Mössbauer spectrum of bulk 7h ESD product from $FeCl_2{\cdot}4H_2O$ (Fig. 20) was modeled using the Mex_disdd program. These data are interpreted within the context of broader work on Mössbauer spectroscopy of minerals with similar structures. Only a handful of Mössbauer spectra could be found in the literature for iron dichloride tetrahydrate, and most of the papers do not provide explicit parameters (Ohshita et al., 2002) or focus on low-temperature (Shinohara, 1977) or magnetic field measurements (Johnson, 1966; Kandel et al., 1973; Spiering et al., 1978) that are not comparable to this study. Overall, the analyzed sample contains 88% of the total Fe as Fe^{3+}, which was 0% in the starting phase of $FeCl_2{\cdot}4H_2O$. The strong oxidation revealed by this Mössbauer result is consistent with Raman observation of hematite occurrence in 3h and 7h ESD products.

The Mössbauer result suggests that both Fe^{2+} and Fe^{3+} are present in two dissimilar sites. Most of the Fe is Fe^{3+} in sites with CS = 0.37-0.38 mm/s and Qs = 0.55 and 0.93 mm/s. A small amount of Fe^{2+} is also observed, with CS = 1.22 and 1.26 mm/s and Qs = 2.96 and 2.10 mm/s, respectively. Ôno et al. (1964) report parameters of CS = 1.26 mm/s and QS = 0.80 mm/s for $FeCl_2$; these seem unusual for this phase. Chandra and Hoy (1966) studied $FeCl_2{\cdot}2H_2O$ and gave parameters of CS = 1.03 mm/s and QS = 2.50 mm/s. Grant et al. (1966) gave parameters of CS = 1.22 mm/s and QS = 2.98 mm/s for $FeCl_2{\cdot}4H_2O$ – very similar to the parameters obtained in this study, though our modern analyses reveal two different doublets.

VNIR spectra (Fig. 21) were measured from the *as is* surfaces of 0.25h, 1h, 3h, and 7h ESD products from $FeCl_2{\cdot}4H_2O$ (T_{eq} < 30°C, Fig. 2). As with the ESD products from $FeSO_4{\cdot}7H_2O$ (Fig. 10), there are two major trends of spectral changes following the increase of ESD duration. Absorption band depth near 1.0, 1.4, and 1.9 µm decreases, suggesting a gradual dehydration, and overall spectral contrast decreases, consistent with the destruction of a crystalline structure observed by Raman and XRD analysis. Furthermore, there is a reduction of spectral slope between 400 to 800 nm that is more obvious in Figure 21 than in Figure 10. This more obvious slope change could be a reflection of Fe^{3+}/Fe_{total} = 88% in 7h ESD from $FeCl_2{\cdot}4H_2O$, which is higher than Fe^{3+}/Fe_{total} = 44% in 7h ESD product from $FeSO_4{\cdot}7H_2O$, determined by Mössbauer analyses.

4.2.2. ESD products from Na, K, Mg, Al, Fe^{2+}-chlorides

The structural damage (i.e., development towards amorphization) of common chlorides by energetic electrons of the ESD process is strongly influenced by chemical bonding. XRD is the major tool to characterize these ESD products.

After running ESD experiments with the same time duration (Table 1), the product from a starting material of $FeCl_2{\cdot}4H_2O$ shows an obvious change in XRD pattern (Fig. 19), whereas the products from either NaCl or KCl as starting material (Fig. 22) still have perfect matches with the standard crystalline forms of NaCl (pdf: 00-005-0628) and KCl (pdf: 00-004-0587).

Similarly, the XRD pattern of the LT-7h ESD product from $AlCl_3.6H_2O$ indicates a total amorphization (1st black curve in Fig. 23). On the other hand, the XRD pattern of the LT-7h ESD product from $MgCl_2{\cdot}6H_2O$ (2nd black curve in Fig. 23) has an uneven raised background, with lines that match with a mixture of $MgCl_2{\cdot}H_2O$ (pdf: 00-061-0222), $MgCl_2{\cdot}2H_2O$ (pdf: 00-003-0765), and $MgCl_2{\cdot}4H_2O$ (pdf: 04-017-8711), suggesting dehydration from $MgCl_2{\cdot}6H_2O$. The raised background, the line broadening, and line merging indicate development of amorphization. Furthermore after a long duration (21 hours) ESD on $MgCl_2{\cdot}6H_2O$, the XRD lines of $Mg(ClO_4)_2{\cdot}6H_2O$ (pdf: 00-014-0022) appear (not shown), indicating oxidation from Cl^{1-} to Cl^{7+} as observed in NaCl by our previous study (Wu et al., 2018).

In contrast, the XRD pattern of the LT-7h ESD product from $CaCl_2 \cdot 2H_2O$ (3rd black curve in Fig. 23) almost perfectly matches standard $CaCl_2 \cdot 2H_2O$ (pdf: 04-010-1481). During the XRD measurement (total of 15 minutes) on the 14h ESD product from $CaCl_2 \cdot 2H_2O$, an obvious color change of the sample (from white to semi-transparent) was observed (laboratory relative humidity > 55%) and an XRD pattern similar to standard $CaCl_2 \cdot 2H_2O$ was obtained. Based on these two XRD measurements, we estimate that the ESD process may have caused dehydration of $CaCl_2 \cdot 2H_2O$, while a positive identification of the ending phase is lacking at current stage.

Overall, these XRD data on 7h ESD products from Mg, Fe, Al, Ca, Na, K chlorides suggest an approximate grouping that reflects how easily the ESD process causes structural damage of these chlorides, with Al, Fe, and Mg chlorides more easily damaged than Ca, Na, and K chlorides. This grouping is consistent with the observed ease of Cl release induced by the ESD process from common chlorides as reported in Wang et al. (2020).

5. Discussion

Table 3 summarizes the major conclusions on phase identifications of the ESD products from each salt. The column of "mid-phase" after a short period of ESD ($\leqslant$ 1.5 hour) shows the pathways of these ESD-induced phase transformations. The listed final phases were reached mostly after 7 hours of the ESD process, with a few exceptions. Table 3 shows that phase transformations have occurred to different degrees in most of the 22 minerals and their mixtures tested in this study (a total of 75 ESD experiments, Table 1), as induced by a medium-strength ESD process with limited time duration (normally 7 hours). There are three major trends in the phase transformations: dehydration, amorphization, and oxidation of Fe, S, and Cl, which will be discussed separately.

5.1. Dehydration

Dehydration of hydrous salts was determined on the basis of direct Raman and XRD identification in ESD products of phases with hydration degrees lower than the starting salts. For example, $MgSO_4 \cdot xH_2O$ (x=1, 4), $FeSO_4 \cdot xH_2O$ (x=1, 4), $FeOHSO_4$, $Fe_2(SO_4)_3$, and γ-$CaSO_4$ were found in the ESD products of $MgSO_4 \cdot 7H_2O$, $FeSO_4 \cdot 7H_2O$, $Fe_{4.67}(SO_4)_6(OH)_2 \cdot 20H_2O$, and $CaSO_4 \cdot 2H_2O$ (Fig. 4, 6, 7, 8, 9, 12, 14). $FeCl_2 \cdot 2H_2O$, $FeCl_2$, and $MgCl_2 \cdot xH_2O$ (x=1, 2, 4) were found in the ESD products of $FeCl_2 \cdot 4H_2O$ and $MgCl_2 \cdot 6H_2O$ (Fig. 19, 23).

In addition, there are three specific ESD-induced dehydrations. The first is that the highly hydrated sulfates ($MgSO_4 \cdot 7H_2O$, $FeSO_4 \cdot 7H_2O$) have a higher dehydration rate than those with lower hydration degrees of the same type (i.e., $MgSO_4 \cdot xH_2O$, $FeSO_4 \cdot xH_2O$, x=1, 4). This was reflected by the shift of central positions of the ν_1 Raman peak in the products as a function of ESD duration. The second is the occurrence of hydrolysis induced by ESD, i.e., from $FeSO_4 \cdot H_2O$ to $Fe(OH)SO_4$. The third is the difficulty in the dehydration of the salts (and minerals) without structural H_2O but only OH, such as jarosite $NaFe_3(OH)_6(SO_4)_2$ and akaganeite FeO(OH, Cl), as well as the 1:1 mixtures of Na-jarosite with each of two hydrous salts ($MgSO_4 \cdot 7H_2O$ and $MgCl_2 \cdot 6H_2O$). The spectrum of hematite was seen from some spots in the Raman scans on these ESD products, but it did not affect the conclusion from Mössbauer spectra, i.e. ~ 100% jarosite among the Fe-phases in bulk samples. This result means that transformation to hematite from jarosite by medium-strength ESD must be at a very low rate compared with those of other Mg, Fe^{2+}, Fe^{3+}, Ca, and Na sulfates.

5.2. Amorphization

Amorphization of salts in this study is judged by Raman and XRD data analyses, with Raman analysis made on the *as is* surface of ESD products, and XRD analysis made on the bulk sample of ESD products. Three stages of amorphization can be distinguished based on Raman data analyses (Table 3). For the Amor-I group, such as those observed from Na_2SO_4, $CaSO_4 \cdot 2H_2O$, and Na_2SO_3 after 7h ESD (Fig. 13, 14, 15), the obvious broadening of major Raman peaks indicates the initiation of structural distortion from a perfect crystalline phase, which is commonly accompanied by the raising of spectral background and reduction of signal to noise (S/N). Structural distortion would generate the observed changes in chemical bond lengths and bond angles in a crystal, causing a much wider Raman peak to be obtained from a vibrational mode. The envelope of many Raman peaks with slightly different central positions widens because of many slightly different chemical bonds in a distorted structure, and an overall reduced S/N. Raman spectra of Amor-III exhibit a total loss of spectral details, in many cases with merged peaks in ν_1, ν_2, ν_3, and ν_4 modes, extensively broadened peak widths (> 10 times), and very low S/N, observed from $MgSO_4 \cdot yH_2O$ (y=7, 4), $FeSO_4 \cdot yH_2O$ (y=7, 4), $Fe_{4.67}(SO_4)_6(OH)_2 \cdot 20H_2O$, $FeCl_2 \cdot 4H_2O$ after the ESD process (Fig. 5a, 7b, spectra #4 to #8 in Fig. 12b, spectra #3 to #6 in Fig. 18). The spectra of Amor-II have characteristics between those of Amor-I and Amor-III, such as the ESD product of $MgSO_4 \cdot H_2O$ shown in Fig. 5b.

Two stages of amorphization can be distinguished from the XRD data (Table 3). Amor-III would appear as the "large hump" in the XRD patterns from the ESD products from $MgSO_4 \cdot yH_2O$ (y=7, 4) (Fig. 6), $FeSO_4 \cdot 7H_2O$ (Fig.9), $FeCl \cdot 4H_2O$ (Fig. 19), and $AlCl_3.6H_2O$ (Fig. 23), consistent with Amor-III assigned by Raman analyses. Because XRD sampled the powder from the full depth of the SiO_2 cell including the bottom of cell that is less affected by energetic electrons, some XRD lines of crystalline phases may overlie the "large hump" (Fig. 6, 9, 19) while the Raman spectra from the *as is* surface show full amorphization (Fig. 5a, 18). The XRD pattern of the products assigned to Amor-I and Amor-II by Raman analysis would appear as line broadening and the merge of line groups, as seen in Figure 6 (1.5h-ESD from $MgSO_4 \cdot H_2O$), Figure 16 (7h ESD from $NaHSO_3$), and Figure 23 (LT- 7h ESD from $MgCl_2 \cdot 6H_2O$).

It is worth noting that the generation of Amor-III is normally accompanied by the rapid dehydration from sulfates originally having high degrees of hydration, such as from $MgSO_4 \cdot xH_2O$ (x=4, 7), $FeSO_4 \cdot xH_2O$ (x=4,7), and $Fe_{4.67}(SO_4)_6(OH)_2 \cdot 20H_2O$. Amor-I or Amor-II occurred in anhydrous sulfates (e.g., Na_2SO_4, Na_2SO_3) or those with a low degree of hydration, e.g., $MgSO_4 \cdot H_2O$.

The rate of amorphization (i.e., the ease of damaging the crystalline structure) of common chlorides appears to be more related to the type of cations present, and reflected by a grouping of chlorides mentioned in section 4.2.2, i.e., higher rates in Fe, Mg, and Al chlorides than in Ca, Na, and K chlorides. The same grouping was found in experimentally observed rates of Cl-release induced by ESD from Mg, Fe, Al, Ca, Na, and K chlorides (Wang et al., 2020), which was correlated with the degree of M - Cl bond covalence that is usually quantified by the difference of electronegativity of M and Cl (Allred, 1961). These electronegativity differences range from 2.34 to 2.16 for KCl, NaCl, and $CaCl_2$, and from 1.2 to 1.85 for $FeCl_3$, $AlCl_3$, $FeCl_2$, and $MgCl_2$ (Wang et al., 2020). An apparent connection between amorphization and dehydration is observed in chlorides. Hydrous chlorides ($AlCl_3 \cdot 6H_2O$, $FeCl_2 \cdot 4H_2O$, $MgCl_2 \cdot 6H_2O$) appeared to amorphize more quickly (Fig. 19, 23) than anhydrous chlorides (NaCl, KCl, Fig. 22). Nevertheless, the ESD-induced Cl-release experiments were conducted strictly on anhydrous chlorides (KCl, NaCl, $CaCl_2$, $FeCl_3$, $AlCl_3$, $FeCl_2$, and $MgCl_2$), and the same grouping was found in two sets of experiments (Wang et al., 2020, and this study). We conclude that the rate of amorphization of the tested chlorides is fundamentally affected by the degree of M - Cl bond covalence.

5.3. Oxidation

Oxidation of Fe^{2+} to Fe^{3+} is evidenced by Mössbauer analyses of the ESD products from $FeSO_4 \cdot 7H_2O$ and $FeCl_2 \cdot 4H_2O$. The ratio of Fe^{3+}/Fe_{total} in both cases changed from zero to 44%, and to 88%, respectively, after a medium-strength ESD process of only 7 hours. These Mössbauer results are confirmed by the slope change in the 400-800 nm range of VNIR spectra, particularly as seen in the ESD-product set from $FeCl_2 \cdot 4H_2O$ (Fig. 21). The hydrolysis from $Fe^{2+}SO_4 \cdot H_2O$ to $Fe^{3+}(OH)SO_4$ revealed by Raman spectra (Fig. 8) and by XRD-based phase ID (Fig. 9), and the appearance of $Fe^{3+}OCl$ in the ESD product of

$FeCl_2 \cdot 4H_2O$ (Fig. 19), provide additional evidence of the oxidation of ferrous iron to ferric iron, induced by the ESD process.

During a normal glow discharge (ESD-NGD) in simulated Mars atmospheric composition and pressure, the free radicals CO^{2+}, CO^{+}, O_I, H_{III}, H_{II}, OH, Ar_I, N_2, N_2^{+} (and not excluding O_2, NO, *and* O^{+} because of the overlapping of plasma lines used for detection) were detected instantaneously by *in situ* plasma emission spectroscopy. O_3 was also detected in the output gas by UV and mid-IR spectroscopy (Wu et al., 2018). These free radicals would induce the oxidation of Fe^{2+} to Fe^{3+}. Similarly, oxidation of Cl^{-} to Cl^{7+} was indicated in this study by the presence of $Mg(ClO_4)_2 \cdot 6H_2O$ in 21h ESD products from $MgCl_2 \cdot 6H_2O$ (section 4.2.2). In addition, Wu et al. (2018) observed the formation of $NaClO_3$ and $NaClO_4$ from NaCl, both induced by the ESD processes of medium strength (Table S1).

Finally, our hypothesis of S-oxidation induced by ESD process was validated by the analyses of ESD products from two sulfites, $Na_2S^{4+}O_3$ and $NaHS^{4+}O_3$. The XRD-based identification of $Na_2S^{6+}{}_3O_{10}$ in ESD products (Fig. 16) supports the oxidation hypothesis, as does the IC observation of a surge in SO_4 concentration with increasing ESD duration (Fig. 17).

Overall, the results of this study demonstrated that dehydration and amorphization (to different degrees depending on the properties of salts) were induced by the medium-strength ESD processes within a nominal time duration from 0.25 hours to 7 hours. In addition, oxidation of Cl, S, and Fe occurred in Cl-, S-, and Fe-bearing salts as a result of this type of ESD process.

6. Implications for martian dust activities

Martian dust activities have been physically altering the morphology of the martian surface, including physically removing/redepositing the top layer of rocks and soils, particularly for soft secondary minerals. When electrostatic discharge is induced by martian dust activity, it exerts two additional effects on surface minerals: physically impacting them with energetic electrons and chemically attacking them with free radicals and electrons. The potential effects in chemistry and biology of ESD induced by Mars dust activities have been investigated and reported by Wu et al. (2018), and Wang et al. (2020a, b and this study) and by another group in Denmark (Bak et al., 2016, 2017, 2018; Knakjensen et al., 2014; Thoegersen et al., 2019).

To date, there has been no actual measurement made of the electric properties of martian dust events. Thus, two important unknowns remain. First is the probability of the occurrence of an ESD during a dust event, which would be expressed as a percentage of time duration in a dust event. Second is the type of ESD, either *Townsend dark discharge (TDD)*, or *normal glow discharge (NGD)*, that would occur in a specific dust event. Our current investigations (Wu et al. (2018), and Wang et al. (2020a, b and this study)) revealed the types of phase transformations (with some rate information) that can be induced by a medium-strength NGD to a group of important secondary martian minerals (S- and Cl-salts). However, the overall effect of these phase transformations on the "*big picture"* of martian surface mineralogy cannot be estimated, unless some assumptions on the above two important unknowns are made.

We will take a very conservative assumption for the first unknown, and consider only two extreme cases: grain saltation and global dust storm.

First, grain saltation (GS) can occur on Mars everywhere and all year around when wind speed is beyond a threshold. Atmospheric scientists use *threshold friction speed* ($\boldsymbol{u_{*t}}$) to judge the generation of GS. An early experiment using a wind tunnel (Greely et al., 1980) found that the $\boldsymbol{u_{*t}}$ at martian condition (at 5 mbar, 95% CO_2, T =150-240K) is about 10 times higher than on Earth, i.e., GS is more difficult to initiate on Mars than on Earth. For example, the $\boldsymbol{u_{*t}}$ for grain size of 100 μm is 2.5-3.5 m/s, and the $\boldsymbol{u_{*t}}$ for grain size of 800 μm is 4-5 m/s (Figure 5 of Greely et al., 1980). When adding the effect of the lower gravitational field of Mars, however, a recent study (Sullivan and Kok, 2017) found that at a wind speed much lower than $\boldsymbol{u}_{*t}$, "sporadically mobilized" grains on Mars can develop into "self-sustaining saltation." This conclusion was validated by the observations made during the *Spirit, Opportunity,* and *Curiosity* rover missions (Sullivan et al., 2005, 2008; Sullivan and Kok, 2017).

Fortunately, a Rover Environmental Monitoring Station (REMS) was carried by *Curiosity* rover to Gale Crater. A recent paper (Viudex-Mpreiras et al., 2019) published wind speed data at Gale Crater collected by REMS from sol 9 to sol 1474. Their finding was that the *wind speed probability density function* at Gale Crater matches quite well with the Weibull function, with a scale factor c= 6.87 m/s and a shape parameter k= 1.73 (Fig.1 of Viudex-Mpreiras et al., 2019; Table S2). Furthermore, they found these parameters fall into the ranges of two Viking landers (which landed on flat plain, c=2.55 – 7.9 m/s, k=1.06 – 1.68). On the basis of this REMS data set collected during 2.19 Mars years, the probability of wind speed > 3.5 m/s is 70% and of wind speed > 5 m/s is 53%, at Gale Crater (Table S2). Therefore, even we took the most conservative consideration by using the high *threshold friction speed* ($\boldsymbol{u}_{*t}$) derived by the Greely et al. (1980) experiments (> 5 m/s for grain size of 800 µm), the winds at Gale Crater would induce grain saltation (GS) over half of a martian year (53%, Table 4).

Schmidt et al. (1998) measured the E-fields in saltating grains at a California field site and found a level as high as 166 kV/m (>> 25-34 kv/m BEFT measured in Mars environmental chambers, Farrell et al., 2015; Yan et al., 2017). Since there was no actual measurement of the electric properties of grain saltation made on Mars and counting the other uncertainties in ESD generation that beyond the scope of current study, we chose a very conservative number, 1%, to estimate the ESD occurrence probability induced by martian grain saltation (GS). Combined with the occurring probability of GS during a Mars year at specific sites (e.g., Gale Crater), the resulting probability of a GS-induced ESD would be 5.3×10^{-3}, equal to 87 hours during a martian year (Table 4).

Other martian dust activities, e.g., dust devils and dust storms, would disturb the martian surface dust and sand to much larger degrees than that by grain saltation. For simplification, we use global dust storm (GDS) to make a rough numerical calculation for comparison purposes. In general, GDS occurs on average once every three martian years. Once it occurs, it can be roughly assumed to cover at least 80% of the martian surface and last 10% of a martian year, corresponding ~ 69 Earth days (Gierasch, 1974; Shirley, 2015; Wang and Richardson, 2015). Therefore, the probability of any location on Mars during a martian year encountering a GDS is 0.026, or 435 hours (Table 4).

Now the question is: what is the percentage of time during a GDS that ESD could occur? Based on decades of study of martian dust storms, we understand that they are driven by a set of hot cores. Within the cores, there is likely convective activity, which could generate large electric fields (E-field) that would eventually cause an ESD to occur. During a GDS, the dust in these cores then gets transported to high altitudes and covers the globe of Mars. Therefore in the regions away from the cores, the dust load increases, but it is not vigorously mixing dust. The amount of suspended small aerosols increases, but there is probably not a lot of electrical activity away from the cores (Gierasch, 1974). Considering this model and many more remaining uncertainties in martian GDS than GS, we chose a percentage at two orders of magnitude lower, 0.01%, for the probability of ESD occurring during a global dust storm (Table 4). Thus, the probability of encountering ESD as induced by GDS at any location on Mars during a martian year is 2.6×10^{-6} that equals to 4.4×10^{-2} hour (Table 4).

The second unknown is the type of ESD (either *Townsend dark discharge (TDD),* or *normal glow discharge (NGD)*) that would occur in a specific dust event. Based on gas discharge phenomena described in the literature (Fig. S7), the major difference between TDD and NGD is in electron flux density. This is reflected by the electric current measured in a discharge event (Gallo, 1975), which was observed at µA level for TDD by Farrell et al., (2015), and at mA level for NGD by Wu et al., (2018), both under Mars atmospheric conditions. Based on a modeling study (Delory et al., 2006), the full range of estimated electron flux density between martian TDD and NGD ranges over seven orders of magnitude, from 9 $\times 10^{16}$ $s^{-1}m^{-2}$ (TDD) and 1.5 $\times 10^{24}$ $s^{-1}m^{-2}$ (NGD) (detailed discussion in section 5.3 of Wu et al., 2018**).** An ESD-NGD was observed in our experimental setting, with an electron flux density of 1.42 $\times 10^{20}$ $s^{-1}m^{-2}$ (Table S1) calculated on the basis of measured electric current across the two electrodes, a strength at mid-way between the two extreme cases.

On the other hand, the type of chemical reaction that would be induced by an ESD process depends on the kinetic energy ($\boldsymbol{E_k}$) of electrons being generated, i.e., $\boldsymbol{E_k}$ > an energy threshold for a reaction to occur. As discussed in Wu et al. (2018) and discussed in section 3.2, the kinetic energy of electrons generated in our ESD experiments was estimated on the basis of plasma spectroscopic observations of CO_2^+ and H_α lines, with considerable portion of electrons having $\boldsymbol{E_k}$ >14 eV and even > 17.2 eV. Because the drift velocities of electrons in TDD and NGD are similar (Fig. 4a and equation (8) of Delory et al., 2006; Jackson et al., 2008, 2010), their electrons should have similar kinetic energy distributions. Therefore, the chemical reactions induced by NGD can also be induced by TDD. However, the same reaction induced by the TDD process will take much longer time than NGD to reach the same level of phase transformation because of its lower electron flux density (Fig. S7). For example, the electron flux realized in our NGD experiments is about ~10^4 times of that of typical TDD, thus the mineral transformation produced by a 0.25h ESD-NGD in our experiments (Table 3) would only be seen after about 2500 hours of a typical TDD process.

We further assume that NGD would more likely be induced by dust storms, while TDD would more likely be induced by grain saltation, simply because the difference in the amounts of dust grains involved in these two extreme dust activities matches well with the differences in electron flux densities of NGD and TDD, which are at mA and µA levels, respectively, when measuring electric current under Mars conditions (Farrell et al., 2015; Wu et al., 2018).

Based on the above assumptions and considering only the grain saltation and the global dust storms, we can make very rough estimations on how long it would take on Mars to reach the levels of phase transformations induced by our medium-strength ESD-NGD process in PEACh. The last two rows of Table 4 show that the phase transformations produced by a 0.25h-ESD-NGD process in the PEACh (column #3 of Table 3) would likely be seen after > 29 martian years when considering only the grain saltation induced ESD-TDD (at typical TDD electron flux density level, Table S1). The time would be > 5.7 martian years when considering only the global dust storms induced ESD-NGD (at the same electron flux density level of our experiments, Table S1). The durations needed for the phase transformation levels reached by 7h ESD-NGD (column #4 of Table 3) would likely be seen on Mars after a few hundred martian years for both extreme cases (grain saltation and global dust storms).

Note that the choice of ESD-occurring probabilities in the above analyses (1% for grain saltation and 0.01% for global dust storms), although based on some knowledge, maintains certain arbitrary nature because no real measurements have yet been made on Mars. Our goal was to enable a rough estimation on the numbers of martian years (Table 4), after which the phase transformations observed in our experiments (dehydration, amorphization, and oxidations of Fe, Cl, and S) would be seen on Mars. The estimated time lengths would be 10 to 100 times longer if we chose to further reduce the probability by one to two order of magnitude for both extreme dust activities, with a result of thousands to tens' thousands martian years. Nevertheless, the cold and dry atmospheric conditions have prevailed during Amazonian period (~ 3 Ga), especially in the most recent tens' of million years, during which martian dust activities (dust storms, dust devil, and grain saltation) have been rampantly altering martian surface materials. Our experimental results suggest that ESD induced by martian dust activities may have contributed some of the S- and Cl-rich X-ray amorphous materials at Gale crater, especially in surface soils.

Furthermore, compared with the high frequency of occurrence, large area, and long temporal coverage of martian dust activities in the current epoch on Mars, the other potential amorphization processes, i.e., the sudden exposure of subsurface hydrous salts or a sudden release of subsurface brines (section 1) that might be induced by impacts or by other events such as Recurring Slope Lineae (RSL) would result in mostly localized occurrences with a lower probability of occurrence. This comparison suggests that the ESD process induced by martian dust activities could be a very important process during the Amazonian period on Mars in causing the generation of S- and Cl-rich amorphous materials and the oxidation of Fe, S, and Cl. A direct implication of this conclusion is that we would anticipate significant amounts of S- and Cl-rich amorphous materials, with highly oxidized Cl, S, and Fe, over the entire surface of Mars.

7. Acknowledgements

All coauthors claim no conflict of interest in publishing this manuscript.
Additional data that support this manuscript can be found in Supporting Information document. The digital file corresponding the spectral data in figures of this manuscript is available at a public website of Washington University in St. Louis https://openscholarship.wustl.edu/data/29/ with a DOI link (DOI: 10.7936/e6p1-cc09). No user ID and password are required to access these data.

This laboratory experimental investigation was supported by NASA SSW-80NSSC17K0776. We are thankful to Prof. Ray Arvidson and Mr. P. Carpenter in the Department of Earth & Planetary Sciences for their help in using the ASD spectrometer and the XRD instrument, and their advice regarding the data analyses. We thank Dr. Z. C. Wu for his effort in building the initial ESD setup in the PEACh during his visit to WUSTL during 2015-2016. Furthermore, we are grateful to the McDonnell Center for the Space Sciences (MCSS) at WUSTL for specific financial support (94351A) to continue our collaboration with Chinese planetary scientists and students. EBS and HKQ thank the China Scholarship Council (201806220274 and 201906280336) for supporting their PhD studies at WUSTL.

8. Authors contributions

AW designed the experimental investigations. YCY did the sample preparations and conducted the ESD experiments in the PEACh, with the help of HKQ. AW conducted the analyses using Raman, VNIR spectroscopy, and XRD diffractometry, with the help of EBS. DD and JH performed Mössbauer and IC analyses of ESD products and data interpretations. WMF provided scientific support for the ESD process in martian dust activity, especially the implication study. BLJ and SMM examined the experimental results and the conclusions derived from them. All coauthors participated in the manuscript writing.

9. References

Achilles, C. N., Downs, R. T., Ming, D. W., Rampe, E. B., Morris, R. V, Treiman, A. H., et al. (2017). Mineralogy of an active eolian sediment from the Namib dune, Gale crater, Mars. *Journal of Geophysical Research: Planets*, *122*(11), 2344–2361. https://doi.org/10.1002/2017JE005262

Aerts, R., Somers, W., & Bogaerts, A. (2015). Carbon Dioxide Splitting in a Dielectric Barrier Discharge Plasma: A Combined Experimental and Computational Study. *ChemSusChem*, *8*(4), 702–716. https://doi.org/10.1002/cssc.201402818

Allred, A. L. (1961). Electronegativity values from thermochemical data. *Journal of Inorganic and Nuclear Chemistry*, *17*(3), 215–221. https://doi.org/https://doi.org/10.1016/0022-1902(61)80142-5

Anthony, J. W., R. A. Bideaux, K. W. Bladh, and M. C. Nichols (1990–2003), Handbook of Mineralogy, Mineralog. Soc. Am., Chantilly, VA. http://www.handbookofmineralogy.org/

Bak, E N, Larsen, M. G., Jensen, S. K., Nørnberg, P., Moeller, R., & Finster, K. (2018). Wind-Driven Saltation: An Overlooked Challenge for Life on Mars. *Astrobiology*, *19*(4), 497–505. https://doi.org/10.1089/ast.2018.1856

Bak, Ebbe N, Jensen, S. J. K., Nørnberg, P., & Finster, K. (2016). Methylated silicates may explain the release of chlorinated methane from Martian soil. *Earth and Planetary Science Letters*, *433*, 226–231. https://doi.org/https://doi.org/10.1016/j.epsl.2015.10.044

Bak, Ebbe N, Zafirov, K., Merrison, J. P., Jensen, S. J. K., Nørnberg, P., Gunnlaugsson, H. P., & Finster, K. (2017). Production of reactive oxygen species from abraded silicates. Implications for the reactivity of the Martian soil. *Earth and Planetary Science Letters*, *473*, 113–121. https://doi.org/https://doi.org/10.1016/j.epsl.2017.06.008

Bak, Ebbe N, Larsen, M. G., Moeller, R., Nissen, S. B., Jensen, L. R., Nørnberg, P., et al. (2017). Silicates Eroded under Simulated Martian Conditions Effectively Kill Bacteria—A Challenge for Life on Mars . *Frontiers in Microbiology* . Retrieved from https://www.frontiersin.org/article/10.3389/fmicb.2017.01709

Bish, D. L., Blake, D. F., Vaniman, D. T., Chipera, S. J., Morris, R. V, Ming, D. W., et al. (2013). X-ray Diffraction Results from Mars Science Laboratory: Mineralogy of Rocknest at Gale Crater. *Science*, *341*(6153), 1238932. https://doi.org/10.1126/science.1238932

Blake, D. F., Morris, R. V, Kocurek, G., Morrison, S. M., Downs, R. T., Bish, D., et al. (2013). Curiosity at Gale Crater, Mars: Characterization and Analysis of the Rocknest Sand Shadow. *Science*, *341*(6153), 1239505. https://doi.org/10.1126/science.1239505

Byrne, S., Dundas, C. M., Kennedy, M. R., Mellon, M. T., McEwen, A. S., Cull, S. C., et al. (2009). Distribution of Mid-Latitude Ground Ice on Mars from New Impact Craters. *Science*, *325*(5948), 1674 LP – 1676. https://doi.org/10.1126/science.1175307

Cantor, B. A., Kanak, K. M., & Edgett, K. S. (2006). Mars Orbiter Camera observations of Martian dust devils and their tracks (September 1997 to January 2006) and evaluation of theoretical vortex models. *Journal of Geophysical Research: Planets*, *111*(E12). https://doi.org/10.1029/2006JE002700

Chandra, S., & Hoy, G. R. (1966). Mössbauer studies of quadrupole and hyperfine interactions in FeCl2·2H2O. *Physics Letters*, *22*(3), 254–256. https://doi.org/https://doi.org/10.1016/0031-9163(66)90598-1

Cheetham, A. K., Cole, A. J., & Long, G. J. (1981). Investigation of the mixed-metal sulfide (Mn,Fe)S2 by analytical electron microscopy and Moessbauer spectroscopy. *Inorganic Chemistry*, *20*(9), 2747–2750. https://doi.org/10.1021/ic50223a001

Chio, C. H., Sharma, S. K., & Muenow, D. W. (2007). The hydrates and deuterates of ferrous sulfate (FeSO4): a Raman spectroscopic study. *Journal of Raman Spectroscopy*, *38*(1), 87–99. https://doi.org/10.1002/jrs.1623

Choi, D. S., & Dundas, C. M. (2011). Measurements of Martian dust devil winds with HiRISE. *Geophysical Research Letters*, *38*(24). https://doi.org/10.1029/2011GL049806

Dehouck, E., McLennan, S. M., Meslin, P.-Y., & Cousin, A. (2014). Constraints on abundance, composition, and nature of X-ray amorphous components of soils and rocks at Gale crater, Mars. *Journal of Geophysical Research: Planets*, *119*(12), 2640–2657. https://doi.org/10.1002/2014JE004716

Dehouck, E., McLennan, S. M., Sklute, E. C., & Dyar, M. D. (2017). Stability and fate of ferrihydrite during episodes of water/rock interactions on early Mars: An experimental approach. *Journal of Geophysical Research: Planets*, *122*(2), 358–382. https://doi.org/10.1002/2016JE005222

Delory, G. T., Farrell, W. M., Atreya, S. K., Renno, N. O., Wong, A.-S., Cummer, S. A., et al. (2006). Oxidant Enhancement in Martian Dust Devils and Storms: Storm Electric Fields and Electron Dissociative Attachment. *Astrobiology*, *6*(3), 451–462. https://doi.org/10.1089/ast.2006.6.451

Dyar, M. D., Breves, E., Jawin, E., Marchand, G., Nelms, M., O'Connor, V., et al. (2013). Mössbauer parameters of iron in sulfate minerals†. *American Mineralogist*, *98*(11–12), 1943–1965. https://doi.org/10.2138/am.2013.4604

Eissa, N. A., Sallam, H. A., Sheta, N. H., Radwan, S. N., & Soliman, M. A. (1994). Moessbauer study of the role of Fe22 /Fe3+ ratio and water of hydration on the optical and electrical properties of gamma irradiated melanterite. *Arab Journal of Nuclear Sciences and Applications*, 27(2), 143–154. Retrieved from http://inis.iaea.org/search/search.aspx?orig_q=RN:25068711

Eissa, N. A., Sheta, N. H., El Mossalamy, S. M., Soliman, M. A., & El Fouly, M. H. (1994). Study of the dehydration process of melanterite under heat treatment and gamma irradiation effects using Moessbauer spectroscopy and thermal analysis measurements. *Arab Journal of Nuclear Sciences and Applications*, *27*(2), 33–45. Retrieved from http://inis.iaea.org/search/search.aspx?orig_q=RN:25068893

Ellehoj, M. D., Gunnlaugsson, H. P., Taylor, P. A., Kahanpää, H., Bean, K. M., Cantor, B. A., et al. (2010). Convective vortices and dust devils at the Phoenix Mars mission landing site. *Journal of Geophysical Research: Planets*, *115*(E4). https://doi.org/10.1029/2009JE003413

Esposito, F., Molinaro, R., Popa, C. I., Molfese, C., Cozzolino, F., Marty, L., et al. (2016). The role of the atmospheric electric field in the dust-lifting process. *Geophysical Research Letters*, *43*(10), 5501–5508. https://doi.org/10.1002/2016GL068463

Farrell, W. M., Smith, P. H., Delory, G. T., Hillard, G. B., Marshall, J. R., Catling, D., et al. (2004).

Electric and magnetic signatures of dust devils from the 2000–2001 MATADOR desert tests. *Journal of Geophysical Research: Planets*, *109*(E3). https://doi.org/10.1029/2003JE002088

Farrell, W. M., McLain, J. L., Collier, M. R., Keller, J. W., Jackson, T. J., & Delory, G. T. (2015). Is the electron avalanche process in a martian dust devil self-quenching? *Icarus*, *254*, 333–337. https://doi.org/https://doi.org/10.1016/j.icarus.2015.04.003

Farrell, W. M., McLain, J. L., Collier, M. R., & Keller, J. W. (2017). The Martian dust devil electron avalanche: Laboratory measurements of the E-field fortifying effects of dust-electron absorption. *Icarus*, *297*, 90–96. https://doi.org/https://doi.org/10.1016/j.icarus.2017.06.001

Ferri, F., Smith, P. H., Lemmon, M., & Rennó, N. O. (2003). Dust devils as observed by Mars Pathfinder. *Journal of Geophysical Research: Planets*, *108*(E12). https://doi.org/10.1029/2000JE001421

Forward, K. M., Lacks, D. J., & Sankaran, R. M. (2009). Particle-size dependent bipolar charging of Martian regolith simulant. *Geophysical Research Letters*, *36*(13). https://doi.org/10.1029/2009GL038589

Fu, X., Wang, A. (2017). Crystallinity effects on spectral features of amorphous saponite and

Implication for poorly crystalline phyllosilicates on mars, Abstract #2977 to 48th LPSC

Gallo, C. F. (1975). Coronas and Gas Discharges in Electrophotography: A Review. *IEEE Transactions on Industry Applications*, *IA-11*(6), 739–748. https://doi.org/10.1109/TIA.1975.349370

Grant, R. W., Wiedersich, H., Muir, A. H., Gonser, U., & Delgass, W. N. (1966). Sign of the Nuclear Quadrupole Coupling Constants in Some Ionic Ferrous Compounds. *The Journal of Chemical Physics*, *45*(3), 1015–1019. https://doi.org/10.1063/1.1727651

Greeley, R, Leach, R., White, B., Iversen, J., & Pollack, J. (1980). Threshold windspeeds for sand on Mars: Wind tunnel simulations. *Geophysical Research Letters*, *7*(2), 121–124. https://doi.org/10.1029/GL007i002p00121

Greeley, Ronald, Whelley, P. L., Arvidson, R. E., Cabrol, N. A., Foley, D. J., Franklin, B. J., et al. (2006). Active dust devils in Gusev crater, Mars: Observations from the Mars Exploration Rover Spirit. *Journal of Geophysical Research: Planets*, *111*(E12). https://doi.org/10.1029/2006JE002743

Greeley, Ronald, Waller, D. A., Cabrol, N. A., Landis, G. A., Lemmon, M. T., Neakrase, L. D. V, et al. (2010). Gusev Crater, Mars: Observations of three dust devil seasons. *Journal of Geophysical Research: Planets*, *115*(E7). https://doi.org/10.1029/2010JE003608

Gellert et al., (2006). Alpha Particle X-Ray Spectrometer (APXS): Results from Gusev crater and calibration report. J. Geophys. Research, 111, E02S05, doi:10.1029/2005JE002555.

Harrison, R. G., Barth, E., Esposito, F., Merrison, J., Montmessin, F., Aplin, K. L., et al. (2016). Applications of Electrified Dust and Dust Devil Electrodynamics to Martian Atmospheric Electricity. *Space Science Reviews*, *203*(1), 299–345. https://doi.org/10.1007/s11214-016-0241-8

Huggins, F. E., & Huffman, G. P. (1979). Chapter 50 - Mössbauer Analysis of Iron-Bearing Phases in Coal, Coke, and Ash. In C. B. T.-A. M. for C. and C. P. KARR (Ed.) (pp. 371–423). Academic Press. https://doi.org/https://doi.org/10.1016/B978-0-12-399903-0.50019-2

Itikawa, Y., & Mason, N. (2005). Cross Sections for Electron Collisions with Water Molecules. *Journal* *of Physical and Chemical Reference Data*, *34*(1), 1–22. https://doi.org/10.1063/1.1799251

Jackson, T L, & Farrell, W. M. (2006). Electrostatic fields in dust devils: an analog to Mars. *IEEE Transactions on Geoscience and Remote Sensing*, *44*(10), 2942–2949. https://doi.org/10.1109/TGRS.2006.875785

Jackson, Telana L, Farrell, W. M., Delory, G. T., & Nithianandam, J. (2008). Effect of dust absorption on the electron avalanche process occurring within Martian dust storms. *Geophysical Research Letters*, *35*(16). https://doi.org/10.1029/2008GL034523

Jackson, Telana L, Farrell, W. M., Delory, G. T., & Nithianandam, J. (2010). Martian dust devil electron avalanche process and associated electrochemistry. *Journal of Geophysical Research: Planets*, *115*(E5). https://doi.org/10.1029/2009JE003396

Johnson, C. E. (1966). A M ssbauer effect study of the magnetic properties of FeCl2.2H2O. *Proceedings of the Physical Society*, *88*(4), 943–955. https://doi.org/10.1088/0370-1328/88/4/317

Kandel, L., Weber, M. A., Frankel, R. B., & Abeledo, C. R. (1974). Mössbauer spectroscopy of magnetic phases in FeCl2 · 2H2O. *Physics Letters A*, *46*(6), 369–370. https://doi.org/https://doi.org/10.1016/0375-9601(74)90920-7

Knak Jensen, S. J., Skibsted, J., Jakobsen, H. J., ten Kate, I. L., Gunnlaugsson, H. P., Merrison, J. P., et al. (2014). A sink for methane on Mars? The answer is blowing in the wind. *Icarus*, *236*, 24–27. https://doi.org/https://doi.org/10.1016/j.icarus.2014.03.036

Krauss, C. E., Hor nyi, M., & Robertson, S. (2003). Experimental evidence for electrostatic discharging of dust near the surface of Mars. *New Journal of Physics*, *5*, 70. https://doi.org/10.1088/1367-2630/5/1/370

Lemmon, M. T., Wolff, M. J., Bell, J. F., Smith, M. D., Cantor, B. A., & Smith, P. H. (2015). Dust aerosol, clouds, and the atmospheric optical depth record over 5 Mars years of the Mars Exploration Rover mission. *Icarus*, *251*, 96–111. https://doi.org/https://doi.org/10.1016/j.icarus.2014.03.029

Lide, 2001, Handbook of Chemistry & Physics, 82nd edition, by CRC, London.

Ling, Z., & Wang, A. (2015). Spatial distributions of secondary minerals in the Martian meteorite MIL 03346,168 determined by Raman spectroscopic imaging. *Journal of Geophysical Research: Planets*, *120*(6), 1141–1159. https://doi.org/10.1002/2015JE004805

Ling, Z. C., Wang, A., & Jolliff, B. L. (2011). Mineralogy and geochemistry of four lunar soils by laser-Raman study. *Icarus*, *211*(1), 101–113. https://doi.org/https://doi.org/10.1016/j.icarus.2010.08.020

McEwen, A. S., Dundas, C. M., Mattson, S. S., Toigo, A. D., Ojha, L., Wray, J. J., et al. (2014). Recurring slope lineae in equatorial regions of Mars. *Nature Geoscience*, *7*(1), 53–58. https://doi.org/10.1038/ngeo2014

McLennan, S. M., Grotzinger, J., (2008). The sedimentary rock cycle of Mars. The Martian Surface-Composition, Mineralogy, and Physical Properties, Cambridge University Press, New York

McLennan, S. M. (2012). Geochemistry of sedimentary processes on Mars. Sedimentary Geology of Mars, 102, 119–138. https://doi.org/10.2110/pec.12.102.0119

McLennan, S. M., Anderson, R. B., Bell, J. F., Bridges, J. C., Calef, F., Campbell, J. L., et al. (2014).

Elemental Geochemistry of Sedimentary Rocks at Yellowknife Bay, Gale Crater, Mars. *Science*, *343*(6169), 1244734. https://doi.org/10.1126/science.1244734

McLennan, S. M, Grotzinger, J. P., Hurowitz, J. A., & Tosca, N. J. (2019). The Sedimentary Cycle on Early Mars. *Annual Review of Earth and Planetary Sciences*, *47*(1), 91–118. https://doi.org/10.1146/annurev-earth-053018-060332

Melnik, O., & Parrot, M. (1998). Electrostatic discharge in Martian dust storms. *Journal of Geophysical Research: Space Physics*, *103*(A12), 29107–29117. https://doi.org/10.1029/98JA01954

Metzger, S. M., Carr, J. R., Johnson, J. R., Parker, T. J., & Lemmon, M. T. (1999). Dust devil vortices seen by the Mars Pathfinder Camera. *Geophysical Research Letters*, *26*(18), 2781–2784. https://doi.org/10.1029/1999GL008341

Morris, R. V., Vaniman, D. T., Blake, D. F., Gellert, R., Chipera, S. J., Rampe, E. B., et al. (2016). Silicic volcanism on Mars evidenced by tridymite in high-SiO₂ sedimentary rock at Gale crater. *Proceedings of the National Academy of Sciences*, *113*(26), 7071 LP – 7076. https://doi.org/10.1073/pnas.1607098113

Morrison, S. M., Downs, R. T., Blake, D. F., Vaniman, D. T., Ming, D. W., Hazen, R. M., et al. (2018). Crystal chemistry of martian minerals from Bradbury Landing through Naukluft Plateau, Gale crater, Mars. *American Mineralogist*, *103*(6), 857–871. https://doi.org/10.2138/am-2018-6124

Morrison, S. M., Downs, R. T., Blake, D. F., Prabhu, A., Eleish, A., Vaniman, D. T., et al. (2018). Relationships between unit-cell parameters and composition for rock-forming minerals on Earth, Mars, and other extraterrestrial bodies. *American Mineralogist*, *103*(6), 848–856. https://doi.org/https://doi.org/10.2138/am-2018-6123

Morris, R. V., Rampe, E. B., Graff, T. G., Archer Jr, P. D., Le, L., Ming, D. W., & Sutter, B. (2015). Transmission X-Ray Diffraction (XRD) Patterns Relevant to the MSL CheMin Amorphous Component: Sulfates and Silicates, Abs #2434, 46th LPSC

Montano, P.A. (1981) Transformations and role of iron sulfides in coal liquefaction. Bulletin of the American Physical Society, 26, 201–201

Murphy, J., Steakley, K., Balme, M., Deprez, G., Esposito, F., Kahanpää, H., et al. (2016). Field Measurements of Terrestrial and Martian Dust Devils. *Space Science Reviews*, *203*(1), 39–87. https://doi.org/10.1007/s11214-016-0283-y

Ohshita, T., Nakajima, D., Tsukamoto, A., Tsuchiya, N., Isobe, T., Senna, M., et al. (2002). Role of molecular strain on the solid-state synthesis of coordination compounds from iron(II) chloride tetrahydrate and 1,10-phenanthroline under mechanical stress. *Annales de Chimie Science Des Matériaux*, *27*(6), 91–101. https://doi.org/https://doi.org/10.1016/S0151-9107(02)90017-6

Ôno, K., Ito, A., & Fujita, T. (1964). The Mössbauer Study of the Ferrous Ion in FeCl2. *Journal of the Physical Society of Japan*, *19*(11), 2119–2126. https://doi.org/10.1143/JPSJ.19.2119

Rampe, E. B., Ming, D. W., Blake, D. F., Bristow, T. F., Chipera, S. J., Grotzinger, J. P., et al. (2017). Mineralogy of an ancient lacustrine mudstone succession from the Murray formation, Gale crater, Mars. *Earth and Planetary Science Letters*, *471*, 172–185. https://doi.org/https://doi.org/10.1016/j.epsl.2017.04.021

Rampe, E. B., Lapotre, M. G. A., Bristow, T. F., Arvidson, R. E., Morris, R. V, Achilles, C. N., et al. (2018). Sand Mineralogy Within the Bagnold Dunes, Gale Crater, as Observed In Situ and From Orbit. *Geophysical Research Letters*, *45*(18), 9488–9497. https://doi.org/10.1029/2018GL079073

Reiss, D., Zanetti, M., & Neukum, G. (2011). Multitemporal observations of identical active dust devils on Mars with the High Resolution Stereo Camera (HRSC) and Mars Orbiter Camera (MOC). *Icarus*, *215*(1), 358–369. https://doi.org/https://doi.org/10.1016/j.icarus.2011.06.011

Sakai, N., Sekizawa, H., & Ôno, K. (1981). Mössbauer spectroscopic identification of the γ-ray radiolytic product of FeSO4·7H2O as FeSO4OH·2H2O. *Journal of Inorganic and Nuclear Chemistry*, *43*(8), 1731–1734. https://doi.org/https://doi.org/10.1016/0022-1902(81)80373-9

Sallam, H. A., Eissa, N. A., Sheta, N. H., Soliman, M. A., & El Fouly, M. H. (1994). Mössbauer effect, x-ray diffraction and infrared studies of the effect of gamma irradiation on the molecular bonding of melanterite. *Journal of Physics and Chemistry of Solids*, *55*(11), 1175–1180. https://doi.org/https://doi.org/10.1016/0022-3697(94)90196-1

Schmidt, D. S., Schmidt, R. A., & Dent, J. D. (1998). Electrostatic force on saltating sand. *Journal of Geophysical Research: Atmospheres*, *103*(D8), 8997–9001. https://doi.org/10.1029/98JD00278

Shinohara, M. (1977). Mössbauer Effect Study of $FeCl_2 \cdot 4H_2O$ in the Antiferromagnetic State. *Journal of the Physical Society of Japan*, *42*(1), 64–71. https://doi.org/10.1143/JPSJ.42.64

Shirley, J. H. (2015). Solar System dynamics and global-scale dust storms on Mars. *Icarus*, *251*, 128–144. https://doi.org/https://doi.org/10.1016/j.icarus.2014.09.038

Sklute, E C, Jensen, H. B., Rogers, A. D., & Reeder, R. J. (2015). Morphological, structural, and spectral characteristics of amorphous iron sulfates. *Journal of Geophysical Research: Planets*, *120*(4), 809–830. https://doi.org/10.1002/2014JE004784

Sklute, Elizabeth C, Rogers, A. D., Gregerson, J. C., Jensen, H. B., Reeder, R. J., & Dyar, M. D. (2018). Amorphous salts formed from rapid dehydration of multicomponent chloride and ferric sulfate brines: Implications for Mars. *Icarus*, *302*, 285–295. https://doi.org/https://doi.org/10.1016/j.icarus.2017.11.018

Sobron, P., & Wang, A. (2012). A planetary environment and analysis chamber (PEACh) for coordinated Raman–LIBS–IR measurements under planetary surface environmental conditions. *Journal of Raman Spectroscopy*, *43*(2), 212–227. https://doi.org/10.1002/jrs.3017

Spiering, H., Hösl, S., & Vogel, H. (1978). Polarization effects in mössbauer absorption of a FeCl2 · 4 H2O single crystal in an external magnetic field. *Physica Status Solidi (B)*, *85*(1), 87–93. https://doi.org/10.1002/pssb.2220850108

Sullivan, R., & Kok, J. F. (2017). Aeolian saltation on Mars at low wind speeds. *Journal of Geophysical Research: Planets*, *122*(10), 2111–2143. https://doi.org/10.1002/2017JE005275

Sullivan, R., Banfield, D., Bell, J. F., Calvin, W., Fike, D., Golombek, M., et al. (2005). Aeolian processes at the Mars Exploration Rover Meridiani Planum landing site. *Nature*, *436*(7047), 58–61. https://doi.org/10.1038/nature03641

Sullivan, R., Arvidson, R., Bell III, J. F., Gellert, R., Golombek, M., Greeley, R., et al. (2008). Wind-driven particle mobility on Mars: Insights from Mars Exploration Rover observations at “El Dorado” and surroundings at Gusev Crater. *Journal of Geophysical Research: Planets*, *113*(E6). https://doi.org/10.1029/2008JE003101

Sutter, B, McAdam, A. C., Mahaffy, P. R., Ming, D. W., Edgett, K. S., Rampe, E. B., et al. (2017). Evolved gas analyses of sedimentary rocks and eolian sediment in Gale Crater, Mars: Results of the Curiosity rover's sample analysis at Mars instrument from Yellowknife Bay to the Namib Dune. *Journal of Geophysical Research: Planets*, *122*(12), 2574–2609. https://doi.org/10.1002/2016JE005225

Sutter, Brad, McAdam, A. C., & Mahaffy, P. R. (2019). Chapter 12 - Volatile Detections in Gale Crater Sediment and Sedimentary Rock: Results from the Mars Science Laboratory's Sample Analysis at Mars Instrument. In J. Filiberto & S. P. B. T.-V. in the M. C. Schwenzer (Eds.) (pp. 369–392). Elsevier. https://doi.org/https://doi.org/10.1016/B978-0-12-804191-8.00012-X

Thøgersen, J., Bak, E. N., Finster, K., Nørnberg, P., Jakobsen, H. J., & Knak Jensen, S. J. (2019). Light on windy nights on Mars: A study of saltation-mediated ionization of argon in a Mars-like atmosphere. *Icarus*, *332*, 14–18. https://doi.org/https://doi.org/10.1016/j.icarus.2019.06.025

Toner, J. D., Catling, D. C., & Light, B. (2014). The formation of supercooled brines, viscous liquids, and low-temperature perchlorate glasses in aqueous solutions relevant to Mars. *Icarus*, *233*, 36–47. https://doi.org/https://doi.org/10.1016/j.icarus.2014.01.018

Treiman, A. H., Morris, R. V, Agresti, D. G., Graff, T. G., Achilles, C. N., Rampe, E. B., et al. (2014). Ferrian saponite from the Santa Monica Mountains (California, U.S.A., Earth): Characterization as an analog for clay minerals on Mars with application to Yellowknife Bay in Gale Crater†. *American Mineralogist*, *99*(11–12), 2234–2250. https://doi.org/10.2138/am-2014-4763

Vaniman, D T, Bish, D. L., Ming, D. W., Bristow, T. F., Morris, R. V, Blake, D. F., et al. (2014). Mineralogy of a Mudstone at Yellowknife Bay, Gale Crater, Mars. *Science*, *343*(6169), 1243480. https://doi.org/10.1126/science.1243480

Vaniman, David T, Bish, D. L., Chipera, S. J., Fialips, C. I., William Carey, J., & Feldman, W. C. (2004). Magnesium sulphate salts and the history of water on Mars. *Nature*, *431*(7009), 663–665. https://doi.org/10.1038/nature02973

Viúdez-Moreiras, D., Gómez-Elvira, J., Newman, C. E., Navarro, S., Marin, M., Torres, J., & de la Torre-Juárez, M. (2019). Gale surface wind characterization based on the Mars Science Laboratory REMS dataset. Part II: Wind probability distributions. *Icarus*, *319*, 645–656. https://doi.org/https://doi.org/10.1016/j.icarus.2018.10.010

Wang A., L. A. Haskin, S. W. Squyres, B. L. Jolliff, L. Crumpler, R. Gellert, C. Schröder, K. Herkenhoff, J. Hurowitz, N. J. Tosca, W. H. Farrand, Robert Anderson, A. T. Knudson, (2006), Sulfate Deposition in Subsurface Regolith in Gusev Crater, Mars, *J. Geophys. Res. 111*, E02S17, doi:10.1029/2005JE002513.

Wang, A., Freeman, J. J., Jolliff, B. L., & Chou, I.-M. (2006). Sulfates on Mars: A systematic Raman spectroscopic study of hydration states of magnesium sulfates. *Geochimica et Cosmochimica Acta*, *70*(24), 6118–6135. doi.org/https://doi.org/10.1016/j.gca.2006.05.022

Wang, A., & Ling, Z. C. (2011). Ferric sulfates on Mars: A combined mission data analysis of salty soils at Gusev crater and laboratory experimental investigations. *Journal of Geophysical Research: Planets*, *116*(E7). https://doi.org/10.1029/2010JE003665

Wang, A., & Zhou, Y. (2014). Experimental comparison of the pathways and rates of the dehydration of Al-, Fe-, Mg- and Ca-sulfates under Mars relevant conditions. *Icarus*, *234*, 162–173. https://doi.org/https://doi.org/10.1016/j.icarus.2014.02.003

Wang, A., Freeman, J. J., & Jolliff, B. L. (2009). Phase transition pathways of the hydrates of magnesium sulfate in the temperature range 50°C to 5°C: Implication for sulfates on Mars. *Journal of Geophysical Research: Planets*, *114*(E4). https://doi.org/10.1029/2008JE003266

Wang, A., Ling, Z., Freeman, J. J., & Kong, W. (2012). Stability field and phase transition pathways of hydrous ferric sulfates in the temperature range 50°C to 5°C: Implication for martian ferric sulfates. *Icarus*, *218*(1), 622–643. https://doi.org/https://doi.org/10.1016/j.icarus.2012.01.003

Wang, A., Jolliff, B. L., Liu, Y., & Connor, K. (2016). Setting constraints on the nature and origin of the two major hydrous sulfates on Mars: Monohydrated and polyhydrated sulfates. *Journal of Geophysical Research: Planets*, *121*(4), 678–694. https://doi.org/10.1002/2015JE004889

Wang, A., Sobron, P., Kong, F., Zheng, M., & Zhao, Y.-Y. S. (2018). Dalangtan Saline Playa in a Hyperarid Region on Tibet Plateau: II. Preservation of Salts with High Hydration Degrees in Subsurface. *Astrobiology*, *18*(10), 1254–1276. https://doi.org/10.1089/ast.2018.1829

Wang, A., Ling, Z., Yan, Y., McEwen, A. S., Mellon, M. T., Smith, M. D., et al. (2019). Subsurface Cl-bearing salts as potential contributors to recurring slope lineae (RSL) on Mars. *Icarus*, *333*, 464–480. https://doi.org/https://doi.org/10.1016/j.icarus.2019.06.024

Wang, A., Yan, Y., Jolliff, B. L., McLennan, S. M., Wang, K., Shi, E., & Farrell, W. M. (2020). Chlorine Release From Common Chlorides by Martian Dust Activity. *Journal of Geophysical Research: Planets*, *125*(6), e2019JE006283. https://doi.org/10.1029/2019JE006283

Wang, H., & Richardson, M. I. (2015). The origin, evolution, and trajectory of large dust storms on Mars during Mars years 24–30 (1999–2011). *Icarus*, *251*, 112–127. https://doi.org/https://doi.org/10.1016/j.icarus.2013.10.033

Wei, J., Wang, A., Lambert, J. L., Wettergreen, D., Cabrol, N., Warren-Rhodes, K., & Zacny, K. (2015). Autonomous soil analysis by the Mars Micro-beam Raman Spectrometer (MMRS) on-board a rover in the Atacama Desert: a terrestrial test for planetary exploration. *Journal of Raman Spectroscopy*, *46*(10), 810–821. https://doi.org/10.1002/jrs.4656

White, W. B., (1975). The Infrared Spectra of Minerals (Eds: VC Farmer) , Mineralogical Society, London, 87–110.

Wu, Z., Wang, A., Farrell, W. M., Yan, Y., Wang, K., Houghton, J., & Jackson, A. W. (2018). Forming perchlorates on Mars through plasma chemistry during dust events. *Earth and Planetary Science Letters*, *504*, 94–105. https://doi.org/https://doi.org/10.1016/j.epsl.2018.08.040

Yan, Y. C., Wang, A., Wu, Z. C. (2017). A Simulated Electro-Chemical Reaction for the Generation of Oxidants in Near-Surface Atmosphere and the Cl^{-1} to Cl^{+X} Phase Transformation at Martian surface. Abstract #2413 for 48th Lunar and Planetary Science Conference.

Yen, A. S., Ming, D. W., Vaniman, D. T., Gellert, R., Blake, D. F., Morris, R. V, et al. (2017). Multiple stages of aqueous alteration along fractures in mudstone and sandstone strata in Gale Crater, Mars. *Earth and Planetary Science Letters*, *471*, 186–198. https://doi.org/https://doi.org/10.1016/j.epsl.2017.04.033

10. Captions of tables and figures

Table 1. Salts used in the ESD process and analysis.

Table 2. Mössbauer parameters obtained from curve fittings.

Table 3. Compilation of analysis results of ESD products of the salts studied.

Table 4. Rough calculations on grain saltation and global-dust-storm-induced ESD probabilities based on observations and various assumptions.

Figure 1. Scheme of ESD experimental setup.

Figure 2. Examples of the equilibrated temperatures T_{eq} during ESD experiments on studied salts.

Figure 3. (a) Starting $MgCl_2 \cdot 6H_2O$ (magnification ×0.75); (b, c, d) LT-7h ESD product of $MgCl_2 \cdot 6H_2O$ (×0.75, ×2.0, ×6.0).

Figure 4. Raman spectra of 0.25h ESD products from $MgSO_4 \cdot 7H_2O$; (a) fundamental vibrational modes; (b) H_2O peaks, compared with standard Raman spectra of $MgSO_4 \cdot 3H_2O$ (3w), $MgSO_4 \cdot 4H_2O$ (4w), $MgSO_4 \cdot 5H_2O$ (5w), $MgSO_4 \cdot 6H_2O$ (6w).

Figure 5. Raman spectra of 1.5h ESD products: (a) from $MgSO_4 \cdot 4H_2O$ compared with standard spectrum (4w); (b) from $MgSO_4 \cdot H_2O$ compared with standard spectrum (1w).

Figure 6. XRD results of ESD products from $MgSO_4 \cdot 7H_2O$, $MgSO_4 \cdot 4H_2O$. $MgSO_4 \cdot H_2O$, compared with standard XRD patterns.

Figure 7. Raman spectra of ESD products from $FeSO_4 \cdot 7H_2O$ (using 1% laser power=0.5 mw, Teq < 30°C); (a) First 60 spectra from a 99-spots Raman analysis on *as is* surface of 0.25h ESD product, compared with standard Raman spectra; (b) first 60 spectra of a 120 Raman analysis on as is surface of 7h ESD product.

Figure 8. Raman spectra of ESD products: (a) 1.5h-ESD product from $FeSO_4 \cdot 4H_2O$; (b) products after 1.5h, 8.5h, 15.5h ESD process from $FeSO_4 \cdot H_2O$, compared with standard spectra.

Figure 9. XRD result of LT-7h ESD product (bulk sample) from melanterite $FeSO_4 \cdot 7H_2O$ and szomolnokite $FeSO_4 \cdot H_2O$, compared with standard.

Figure 10. VNIR spectra on as is surfaces of 0.25h, 1h, 3h, 7h ESD (Teq<30°C) from melanterite $FeSO_4 \cdot 7H_2O$.

Figure 11. Mössbauer spectrum and curve fitting results (a, b) of a 7h ESD product from melanterite, $FeSO_4 \cdot 7H_2O$.

Figure 12. Raman spectra of ESD product from ferricopiapite, $Fe_{4.67}(SO_4)_6(OH)_2 \cdot 20H_2O$, compared with standards. (a) Standard spectra of ferricopiapite (ferri), rhomboclase, $FeH(SO_4) \cdot 4H_2O$ (rhom), amorphous $FeS_2(SO_4)_3 \cdot 5H_2O$ (Am5w), anhydrous $Fe_2(SO_4)_3$(anhy), and mikasaite, $Fe_2(SO_4)_3$(mika) (Ling and Wang 2010); (b) Raman spectra of ESD products from ferricopiapite.

Figure 13. Raman spectra of 7h ESD product from Na_2SO_4.

Figure 14. Raman spectra of 7h ESD product from $CaSO_4 \cdot 2H_2O$

Figure 15. Raman spectra of 7h ESD products from $NaSO_3$, compared with standard spectra.

Figure 16. XRD results of 7h ESD product from $NaHSO_3$, compared with original salt, and standards.

Figure 17. Results from ion chromatography on 1h, 2h, 7h ESD products from Na_2SO_3.

Figure 18. Typical Raman spectra of ESD-products from $FeCl_2 \cdot 4H_2O$, compared with a standard spectrum.

Figure 19. XRD pattern of 7h ESD product from $FeCl_2 \cdot 4H_2O$, compared with standards.

Figure 20. Mössbauer spectrum and curve fitting results of a 7h ESD product from $FeCl_2 \cdot 4H_2O$.

Figure 21. VNIR spectra from as is surfaces of 0.25h, 1h, 3h, 7h ESD (Teq <30°C) from $FeCl_2 \cdot 4H_2O$.

Figure 22. XRD results of ESD-7h products from NaCl, KCl, which match with PDF:00-005-0628(NaCl) and PDF: 00-004-0587 (KCl).

Figure 23. XRD results obtained from LT-7h ESD on $AlCl_3 \cdot 6H_2O$, $MgCl_2 \cdot 6H_2O$ and $CaCl_2 \cdot 2H_2O$, compared with standards.

Table 1. **Salts used in the ESD process and analysis.**

Mineral name	Salts	Sources	MP (°C) *	time duration of ESD	Raman	XRD	MB	VNIR	IC
Epsomite	$MgSO_4.7H_2O$	Sigma-Aldrich	150	0.25, 1, 2, 7h	*as is* surfaces	bulk sample			
Starkeyite	$MgSO_4.4H_2O$	made from $MgSO_4.7H_2O$	NA	1.5h	*as is* surfaces	bulk sample			
Kieserite	$MgSO_4.H_2O$	Aldrich	150	1.5h, 8.5h	*as is* surfaces	bulk sample			
Melanterite	$FeSO_4.7H_2O$	Fisher	60	0.25, 1, 3, 7h @ < 30°C*	*as is* surfaces	bulk sample	bulk sample	*as is* surfaces	
Rozenite	$FeSO_4.4H_2O$	made from $FeSO_4.7H_2O$	NA	1.5h	*as is* surfaces	bulk sample			
Szomolnokite	$FeSO_4.H_2O$	made from $FeSO_4.7H_2O$	300	1.5, 8.5, 15.5h	*as is* surfaces	bulk sample			
Ferricopiapite	$Fe_{4.67}(SO_4)_6(OH)_2.20H_2O$	made from $Fe_2(SO_4)_3.5H_2O$ of ACROS	NA	0.25h, 1h, 2h, 3h, 7h	*as is* surfaces				
Na-Jarosite	$NaFe_3(OH)_6(SO_4)_2$	RUBLEV	NA	0.25h, 1h, 2h, 7h,28h, 31h, 57h, 64h	*as is* surfaces		bulk sample	*as is* surfaces	
Na-jarosite +	$MgCl_2.6H_2O$ at 1:1		NA	1h, 2h, 3h, 7h	*as is* surfaces		bulk sample		
Na-jarosite +	$MgSO_4.7H_2O$ at 1:1		NA	1h, 2h, 3h, 7h	*as is* surfaces		bulk sample		
Gypsum	$CaSO_4.2H_2O$	Alfa Aesor	150	0.25, 1, 2, 7, 14, 16, 18h	*as is* surfaces				
Thenardite_	Na_2SO_4	Sigma-Aldrich	884	0.25, 1, 2, 7h	*as is* surfaces				
Sodium sulfite	Na_2SO_3	Sigma	NA	0.25, 1, 2, 7h	*as is* surfaces	bulk sample			Dissolved bulk sample
Sodium bisulfite	$NaHSO_3$	Sigma	NA	0.25, 1, 2, 7, 11h	*as is* surfaces	bulk sample			
Halite	NaCl	Sigma-Aldrich	801	7h		bulk sample			
Sylvite	KCl	Fisher	771	7h		bulk sample			
Bischofite	$MgCl_2.6H_2O$	Sigma-Aldrich	100	7h, 14h@ < 30°C		bulk sample			
Rokuhnite	$FeCl_2.4H_2O$	Fisher	105	7h @ < 30°C	*as is* surfaces	bulk sample	bulk sample	*as is* surfaces	
Sinjarite	$CaCl_2.2H_2O$	ACROS	175	7h, 14h @ < 30°C		bulk sample			
Chloraluminite	$AlCl_3.6H_2O$	Sigma	100	7h @ < 30°C		bulk sample			
Pyrite	FeS_2	natural from Huanzala, Peru	NA	3h, 7h, 10h, 14h	*as is* surfaces	bulk sample	bulk sample	*as is* surfaces	
Akaganeite	FeO(OH,Cl)	made by Fu et al., 2019	NA	0.25h, 1h, 2h, 3h, 7h	*as is* surfaces		bulk sample		

* melting point (°C) from CRC Handbook of Chemistry and Physics, 82nd edition (Lide 2001)

Table 2. Mössbauer parameters obtained from curve fittings.

Sample	7h-ESD from $FeCl_2 \cdot 4H_2O$	7h-ESD from $FeSO_4 \cdot 7H_2O$	7h-ESD from $FeSO_4 \cdot 7H_2O$
Model	Lorentzian/Full Hamiltonian	Lorentzian/Full Hamiltonian	QSD/Velocity approximation
Parameter			
CS 1	0.37	0.49	0.47
QS 1	0.55	0.57	0.57
Width 1	0.29	0.40	0.35*
Area 1	48	23	15
CS 2	0.38	0.42	0.42
QS 2	0.93	1.20	1.09
Width 2	0.32	0.49	0.54
Area 2	40	21	29
CS 3	1.22	1.28	1.27
QS 3	2.96	2.64	2.66
Width 3	0.26*	0.39	0.38
Area 3	5	19	19
CS 4	1.26	1.21	1.24
QS 4	2.10	2.29	2.24
Width 4	0.26	0.45	0.40
Area 4	7	24	20
CS 5		1.29	1.29
QS 5		1.55	1.61
Width 5		0.47	0.53
Area 5		13	17
$\Sigma\%Fe^{3+}$	88	44	44
χ^2	5.98	1.30	1.38

*indicates parameter held constant.

Table 3. Compilation of analyses results of ESD products of the salts studied

Minerals	Salts	Mid-phase after short ESD (≤ 1.5 h)	Final phase after long ESD (≥7h)
Epsomite	$MgSO_4.7H_2O$	$MgSO_4.4H_2O$, Amor-III (Raman)	Amor-III (Raman, XRD)
Starkeyite	$MgSO_4.4H_2O$	Amor-III (Raman)	
Kieserite	$MgSO_4.H_2O$	Amor-II (Raman, XRD)	Amor-II (XRD)
Melanterite	$FeSO_4.7H_2O$	$FeS_{O4}.4H_2O$, FeSO4.H2O, Amor-II (Raman)	Amor-III, $FeSO_4.H_2O$ (Raman, XRD), Fe^{3+}/Fe_{total} =44% (MB)
Rozenite	$FeSO_4.4H_2O$	$FeSO_4.H_2O$, Amor-III (Raman)	
Szomolnokite	$FeSO_4.H_2O$	$FeSO_4.H_2O$, Fe^{2+} to Fe^{3+} (Raman)	Fe^{2+} to Fe^{3+}, $FeSO_4.H_2O$ (Raman, XRD)
Ferricopiapite	$Fe_{4.67}(SO_4)_6(OH)_2.20H_2O$	Ferricopiapite, Rhomboclase, Amor-III (Raman)	Amor-III, mikasaite, $Fe_2(SO_4)_3$ (Raman)
Na-Jarosite	$NaFe_3(OH)_6(SO_4)_2$	No obvious phase change	no obvious phase change, rare hematite, ~ 100% jarosite (MB)
Na-jarosite +	$MgCl_2.6H_2O$ at 1:1	No obvious phase change	No obvious phase change, rare hematite, goethite, ~ 100% jarosite (MB)
Na-jarosite +	$MgSO_4.7H_2O$ at 1:1	No obvious phase change	No obvious phase change, ~100% jarosite (MB)
Gypsum	$CaSO_4.2H_2O$		γ-anhydrite, basanite, Amor-I (Raman)
Thenardite	Na_2SO_4		Amor-I (Raman)
Sodium sulfite	Na_2SO_3		Amor-I (Raman),S^{4+} to S^{6+} (IC)
Sodium bisulfite	$NaHSO_3$		Amor-I, S^{4+} to S^{6+} (XRD)
Halite	NaCl		No obvious phase change
Sylvite	KCl		No obvious phase change
Bischofite	$MgCl_2.6H_2O$		$MgCl_2$ xH_2O (x=1, 2, 4), Amor-I, Cl^{1-} to Cl^{7+} (XRD)
Rokuhnite	$FeCl_2.4H_2O$	Amor-III (Raman)	$FeCl_2.2H_2O$, $FeCl_2$, Amor-III, Fe^{2+} to Fe^{3+}(Raman, XRD), Fe^{3+}/Fe_{total} =88% (MB)
Sinjarite	$CaCl_2.2H_2O$		dehydration
Chloraluminite	$AlCl_3.6H_2O$		Amor-III (XRD)
Akaganiete	FeO(OH,Cl)		No obvious change, ~ 100% Fe^{3+} (MB)
Pyrite	FeS_2		Minor changes (Raman, VNIR, XRD), ~ 98% Fe^{3+} (MB)

Table 4. Rough calculations on grain saltation (GS) and global dust storm (GDS) induced ESD probabilities based on mission observations and various assumptions

Basics		
a year on Mars	668 sols	
a sol on Mars	24h 39m 24s	
total Earth days in a Mars year (day)	687	
total Earth hours in a Mars year (hour)	16488	
Probability in a Mars year	**GS***	**GDS****
Once per every three Mars years		0.33
Assumed duration (10% of a Mars year)		0.1
Assumed area coverage (80% surface)		0.8
Probability having a GDS pass a site		0.026
Total duration of a GDS at a site (hour)		435
Probability of wind speed > 5 m/s (Gale crater)	0.53	
Total duration of GS at Gale crater (hour)	8739	
Chosen ESD occurring probability	**1%**	**0.01%**
Probability to see ESD at a site	5.30E-03	2.6E-06
Duration of ESD at a site (hour)	87	0.0435
Electron flux density vs. current study (ESD-NGD)		
ESD-NGD of same level by GDS		1.0
typical TDD by GS	1.00E-04	
To reach the same level of PT* on Mars (year)**		
End-phases of 0.25h-ESD-NGD	**29**	**5.7**
End-phases of 7h-ESD-NGD	**801**	**161**

* GS = Grain Saltation
** GDS = Global Dust Storm
*** PT= phase transformation

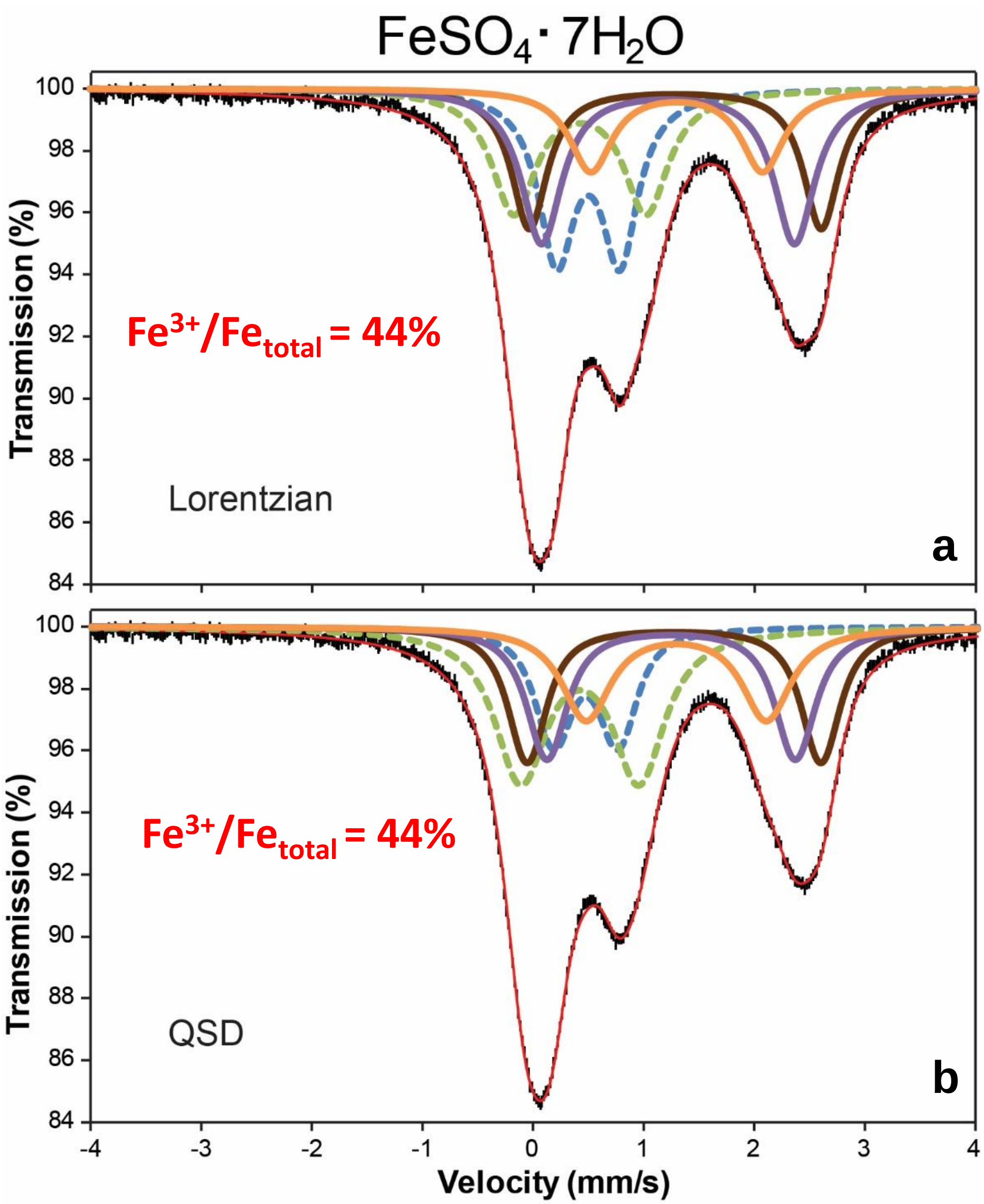

Figure 11. Mössbauer spectrum and curve fitting results (a, b) of a 7h ESD product from melanterite, $FeSO_4 \cdot 7H_2O$

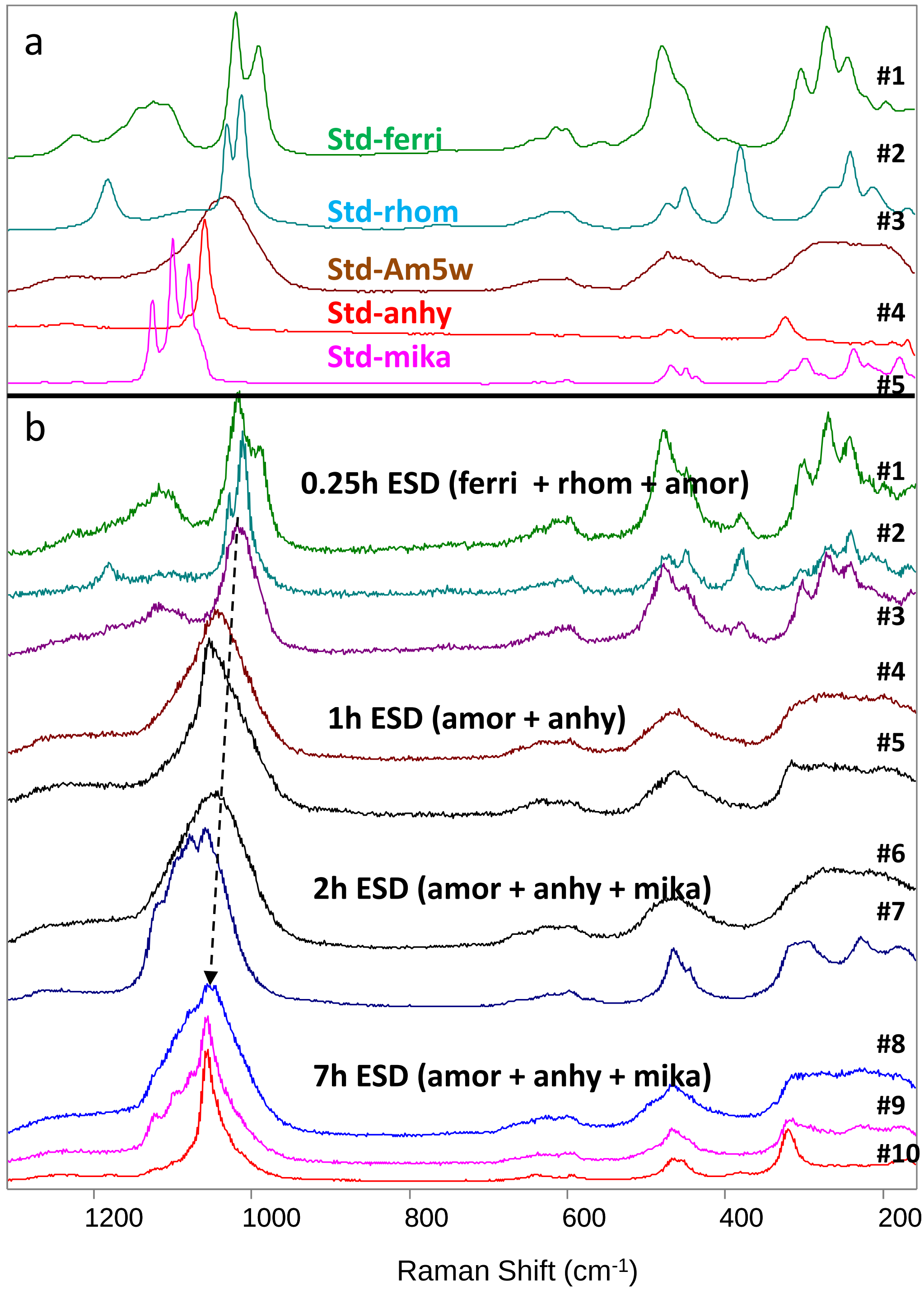

Figure 12. Raman spectra of ESD product from ferricopiapite $Fe_{4.67}(SO_4)_6(OH)_2 \cdot 20H_2O$, compared with standards. (a) Standard spectra of ferricopiapite (ferri), rhomboclase $FeH(SO_4) \cdot 4H_2O$ (rhom), amorphous $Fe_2(SO_4)_3 \cdot 5H_2O$ (Am5w), anhydrous $Fe_2(SO_4)_3$(anhy), and mikasaite $Fe_2(SO_4)_3$(mika) (Ling and Wang 2010); (b) Raman spectra of ESD products from ferricopiapite.

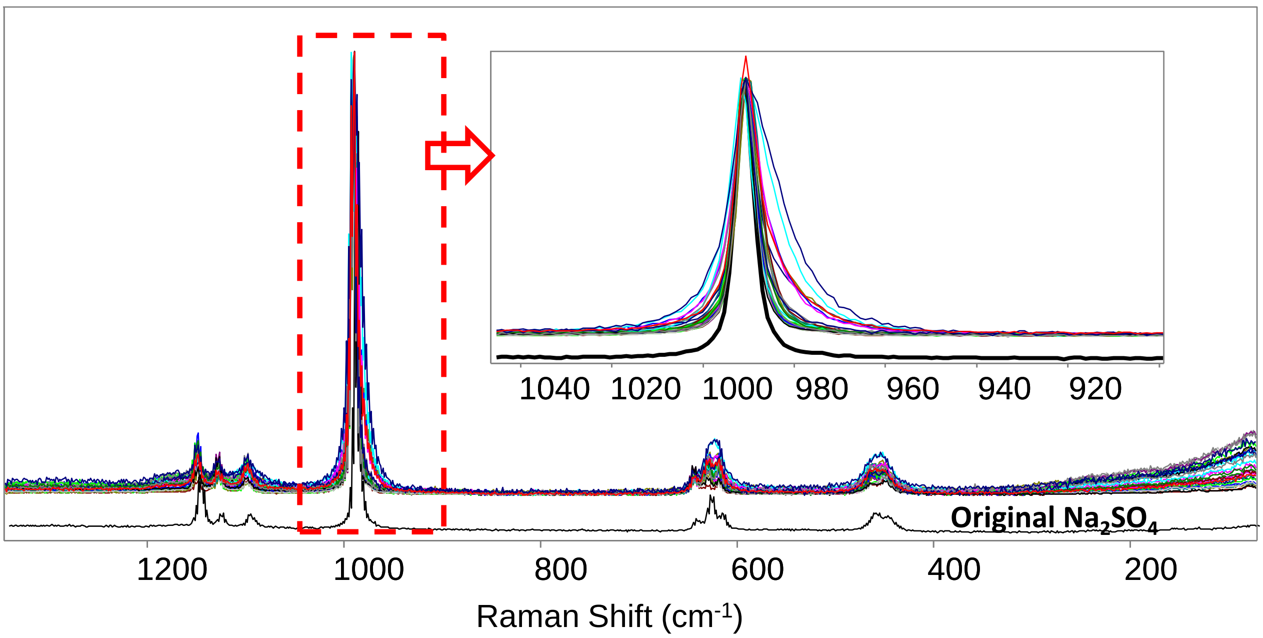

Figure 13. Raman spectra of 7h ESD product from Na_2SO_4, compared with the spectrum of starting Na_2SO_4.

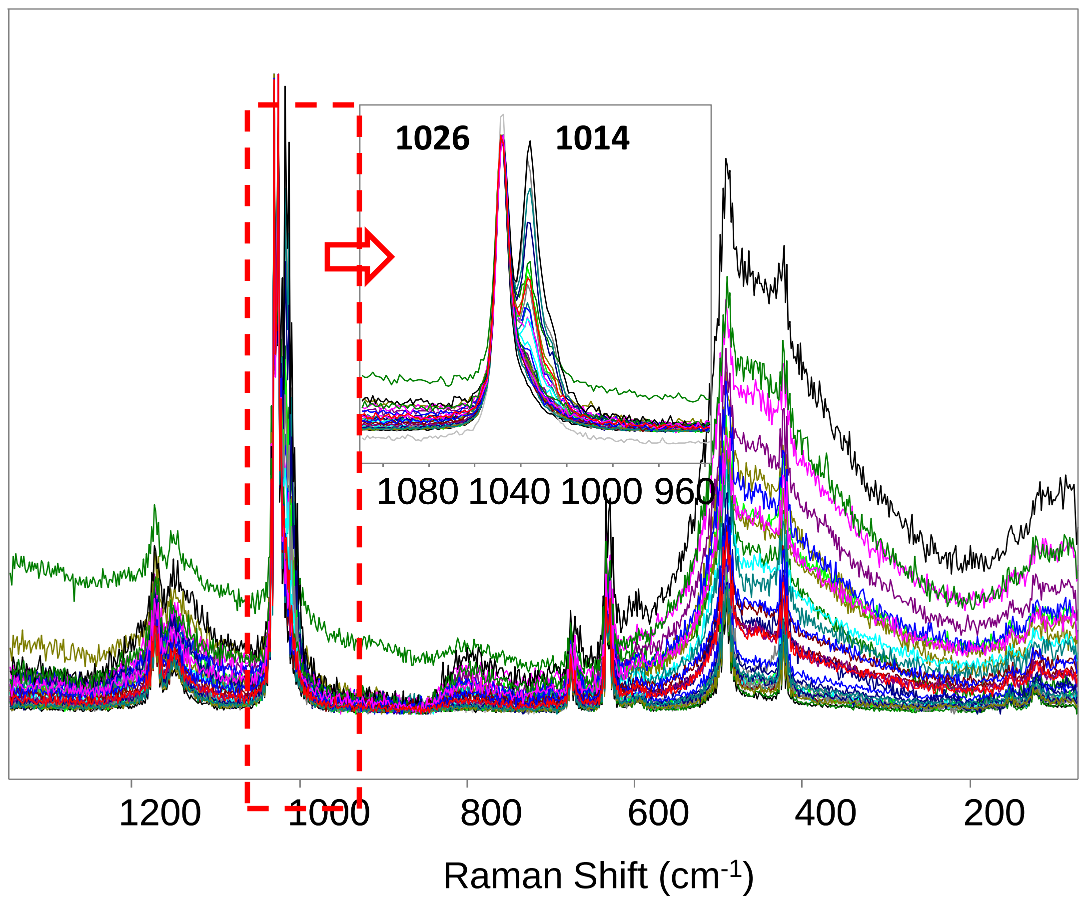

Figure 14. Raman spectra of 7h ESD product from $CaSO_4{\cdot}2H_2O$

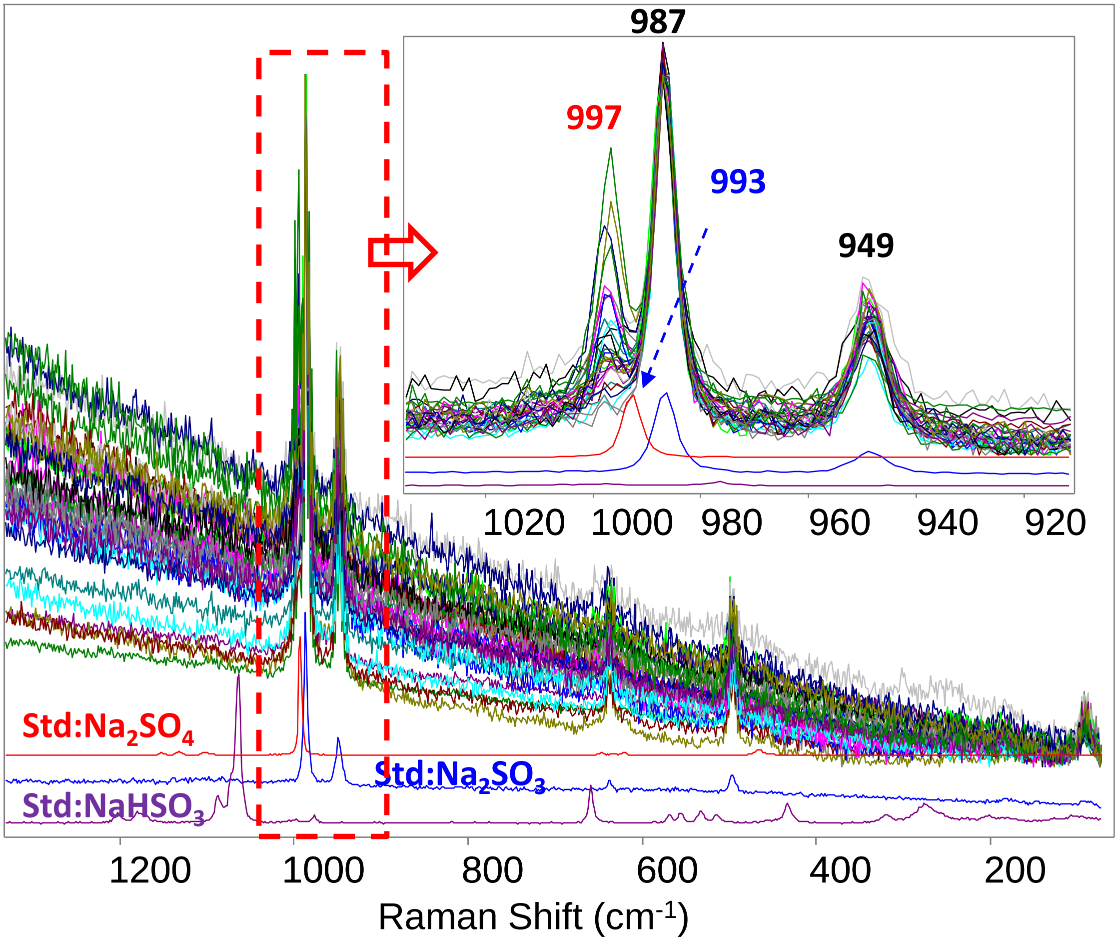

Figure 15. Raman spectra of 7h ESD products from $NaSO_3$, compared with standard spectra.

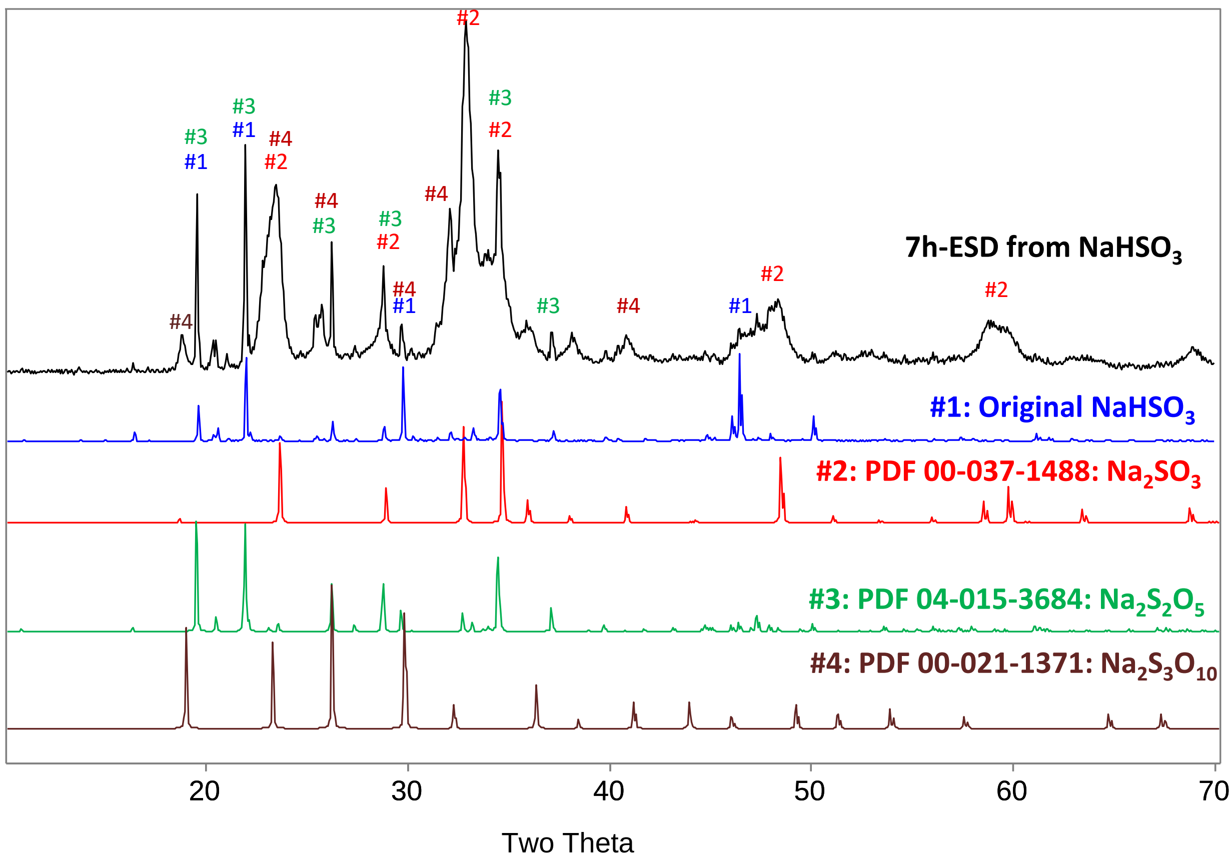

Figure 16. XRD results of 7h ESD product from $NaHSO_3$, compared with original salt, and standards.

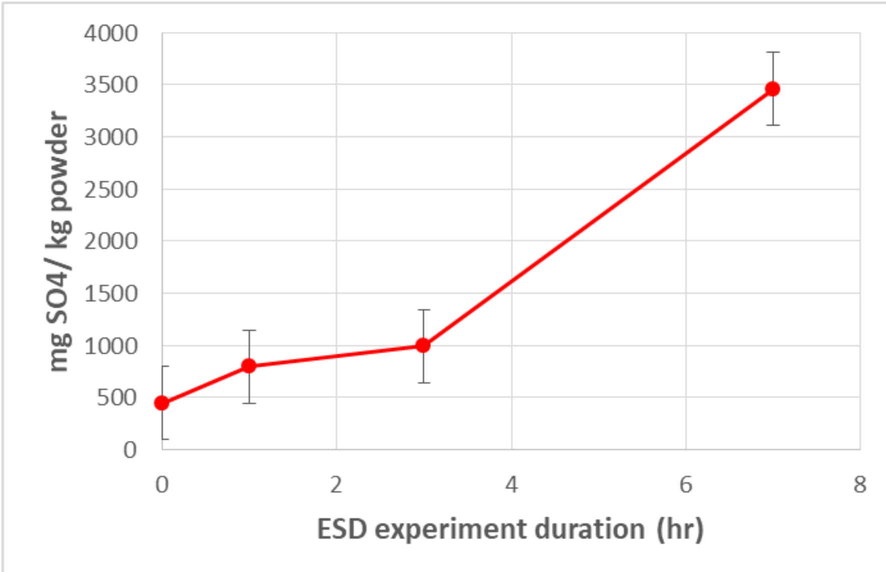

Figure 17. Results from ion chromatography on 1h, 2h, 7h ESD products from Na_2SO_3.

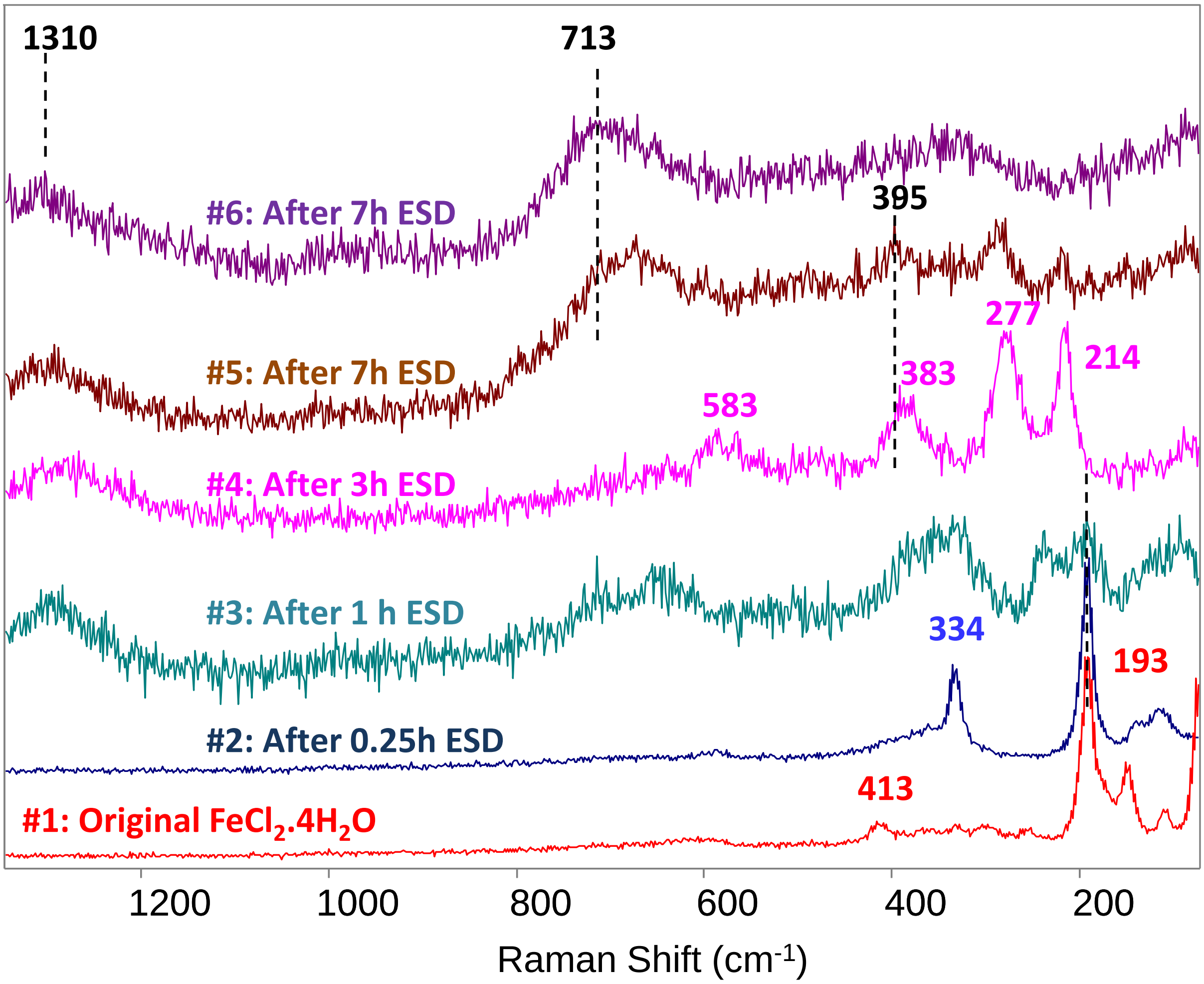

Figure 18. Typical Raman spectra of LT-ESD-products from $FeCl_2 \cdot 4H_2O$, compared with a standard spectrum of starting $FeCl_2 \cdot 4H_2O$.

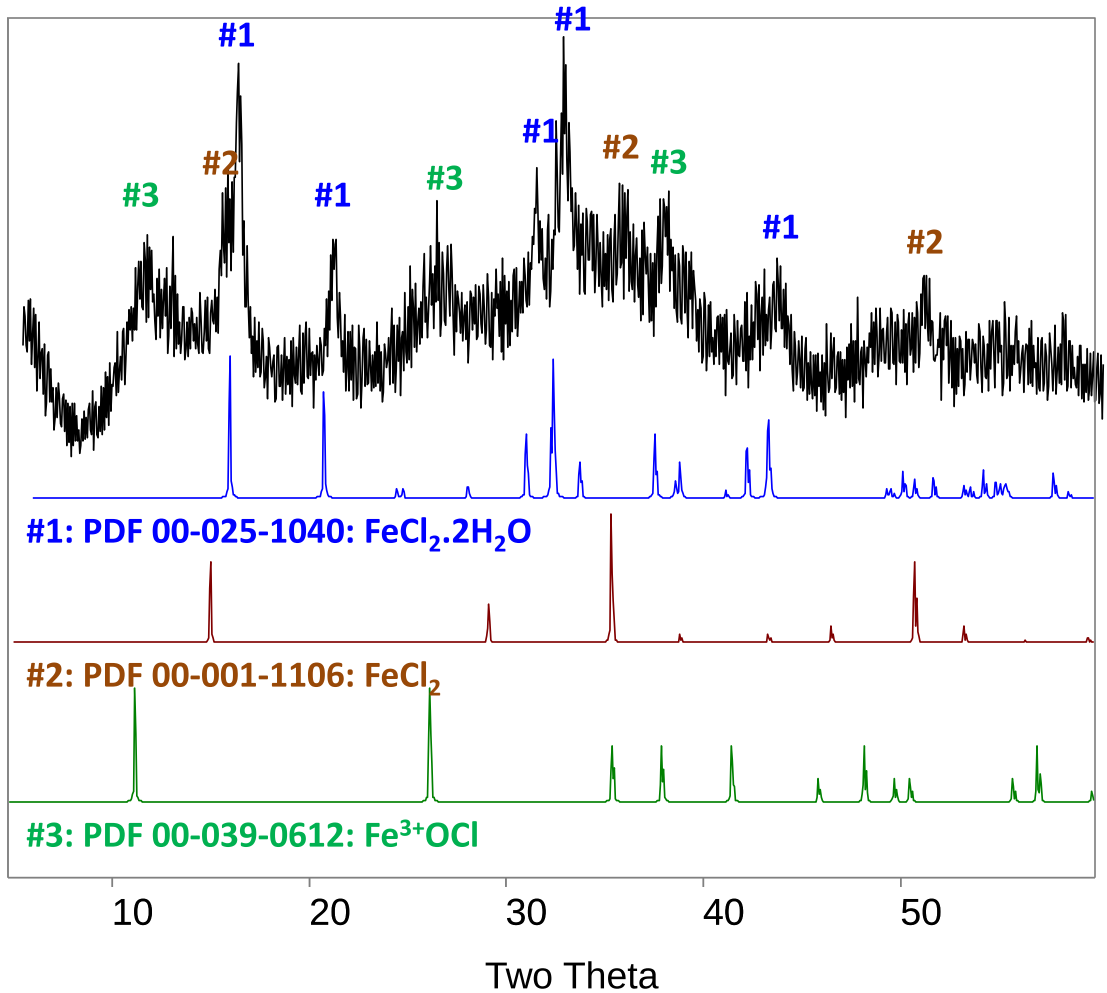

Figure 19. XRD pattern of LT-7h ESD product from $FeCl_2 \cdot 4H_2O$, compared with standards.

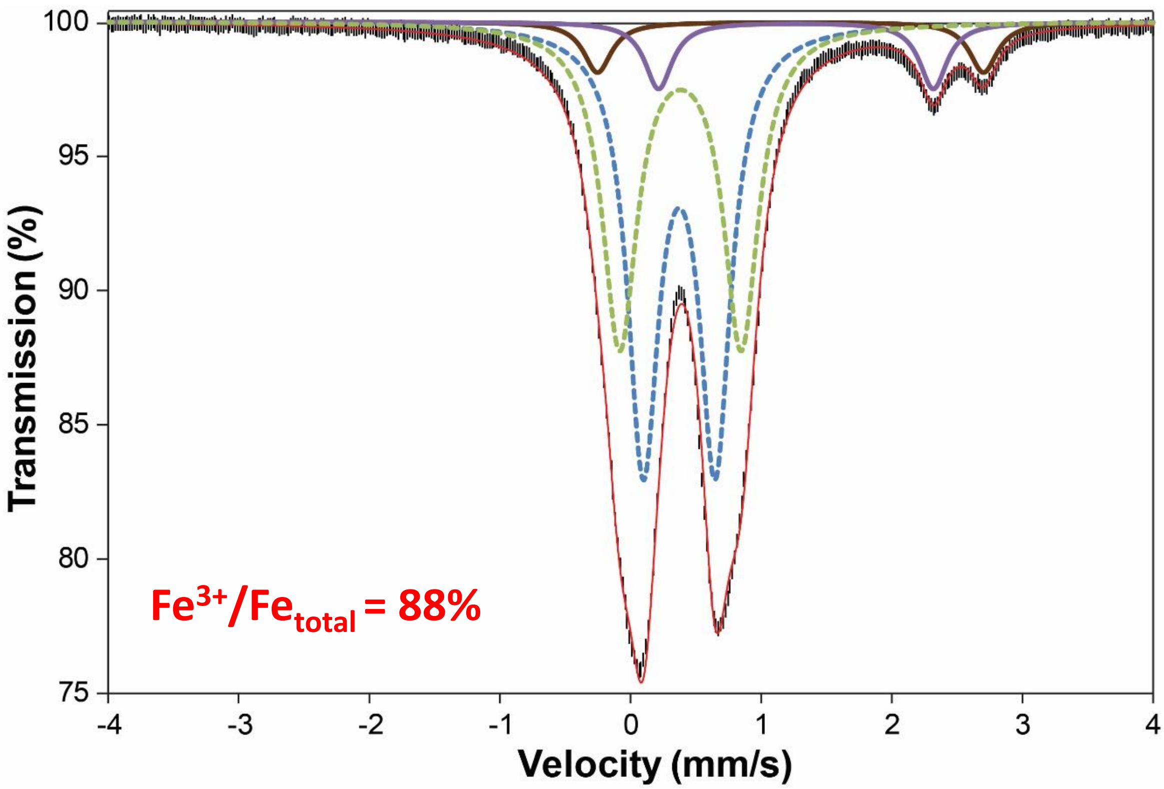

Figure 20. Mössbauer spectrum and curve fitting results of a 7h ESD product from $FeCl_2 \cdot 4H_2O$.

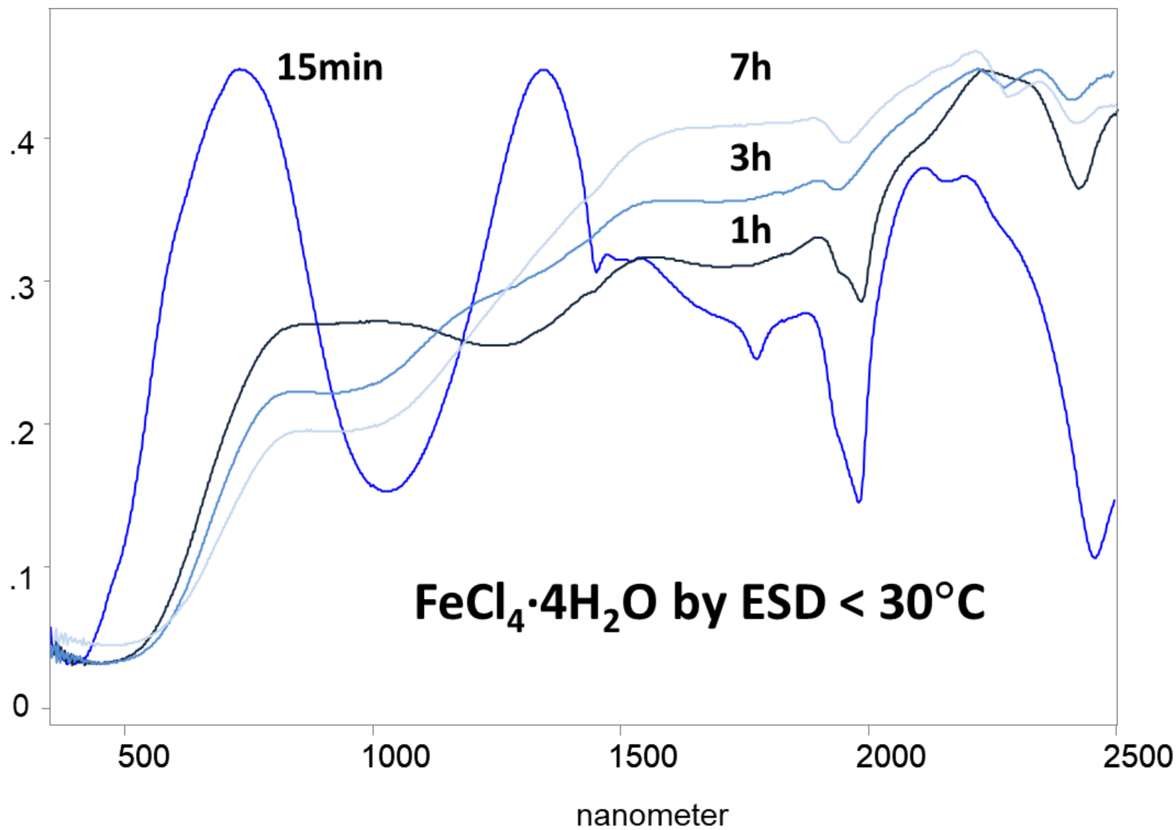

Figure 21. VNIR spectra from as is surfaces of 0.25h, 1h, 3h, 7h LT-ESD (T_{eq} <30°C) from $FeCl_2 \cdot 4H_2O$.

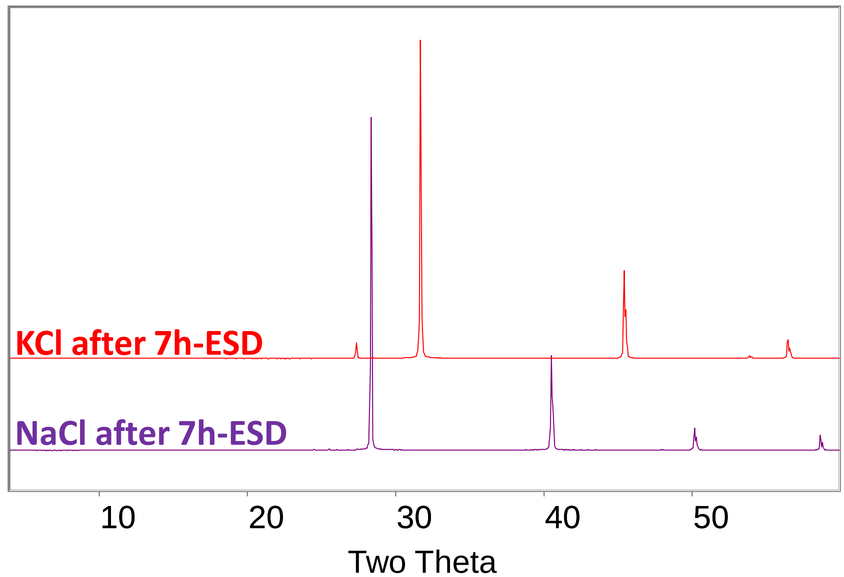

Figure 22. XRD results of ESD-7h products from NaCl, KCl, which match with PDF:00-005-0628(NaCl) and PDF: 00-004-0587 (KCl).

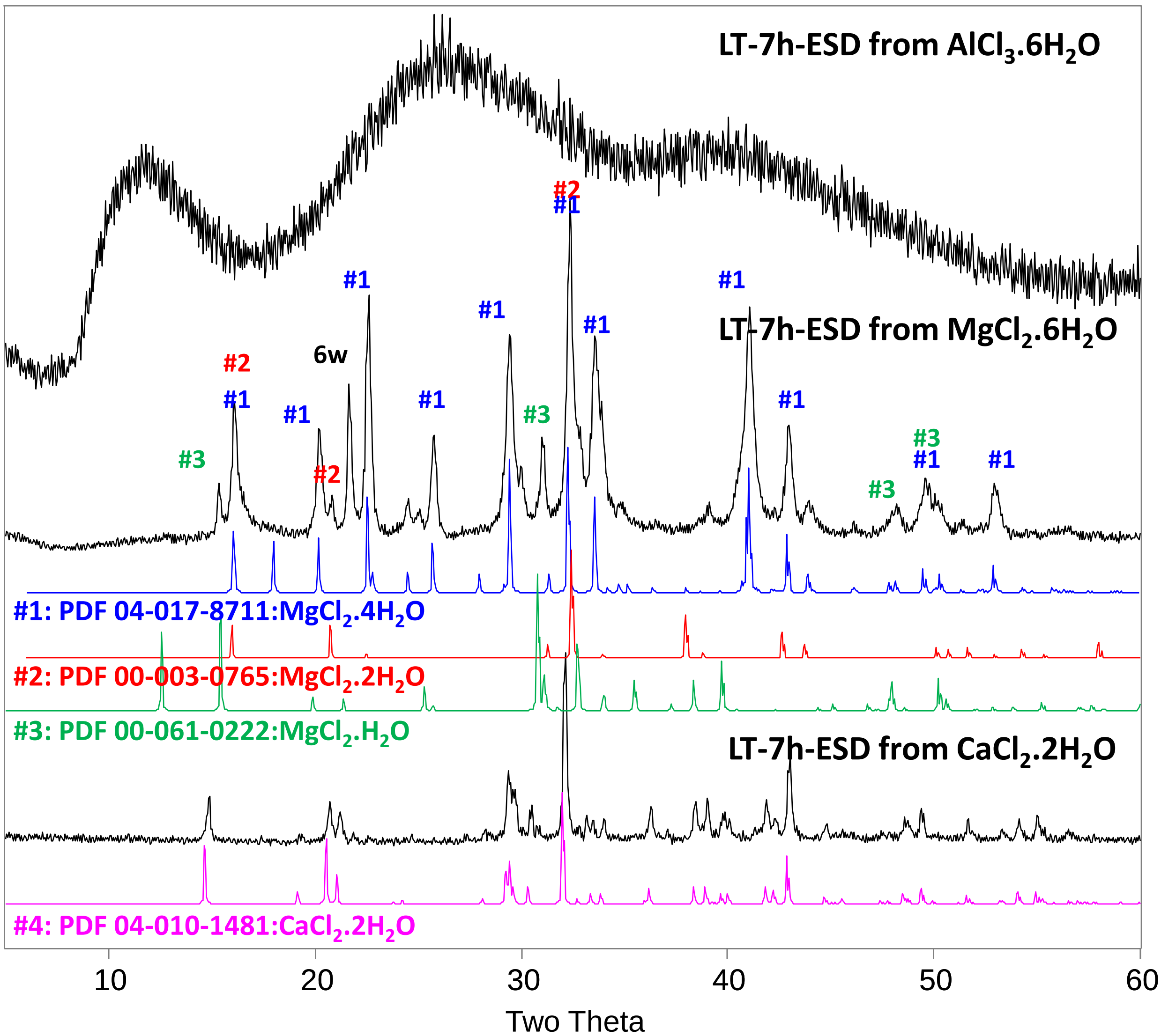

Figure 23. XRD results obtained from LT-7h ESD on $AlCl_3 \cdot 6H_2O$, $MgCl_2 \cdot 6H_2O$ and $CaCl_2 \cdot 2H_2O$, compared with standards.

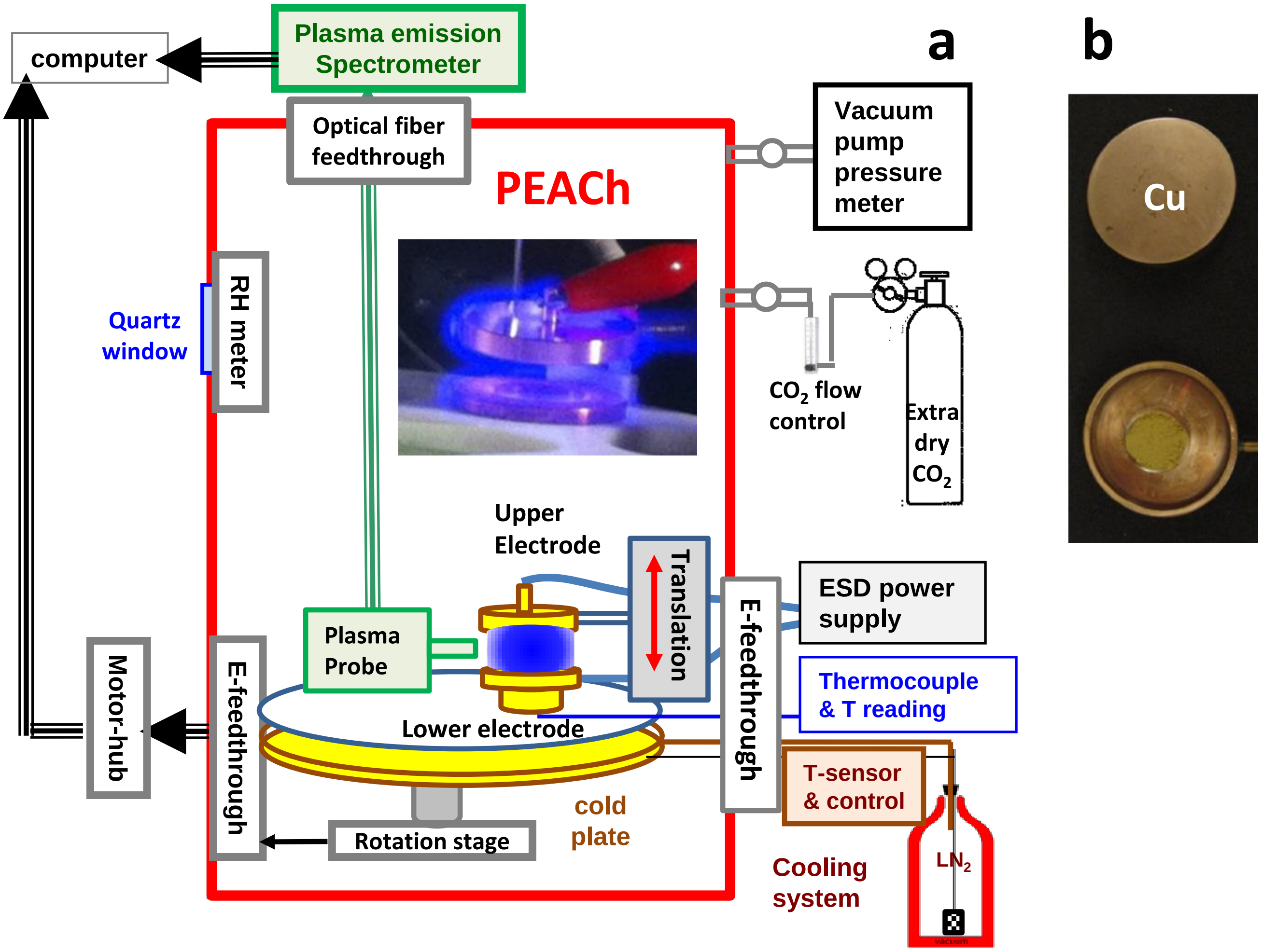

Figure 1. Scheme of ESD experimental setup

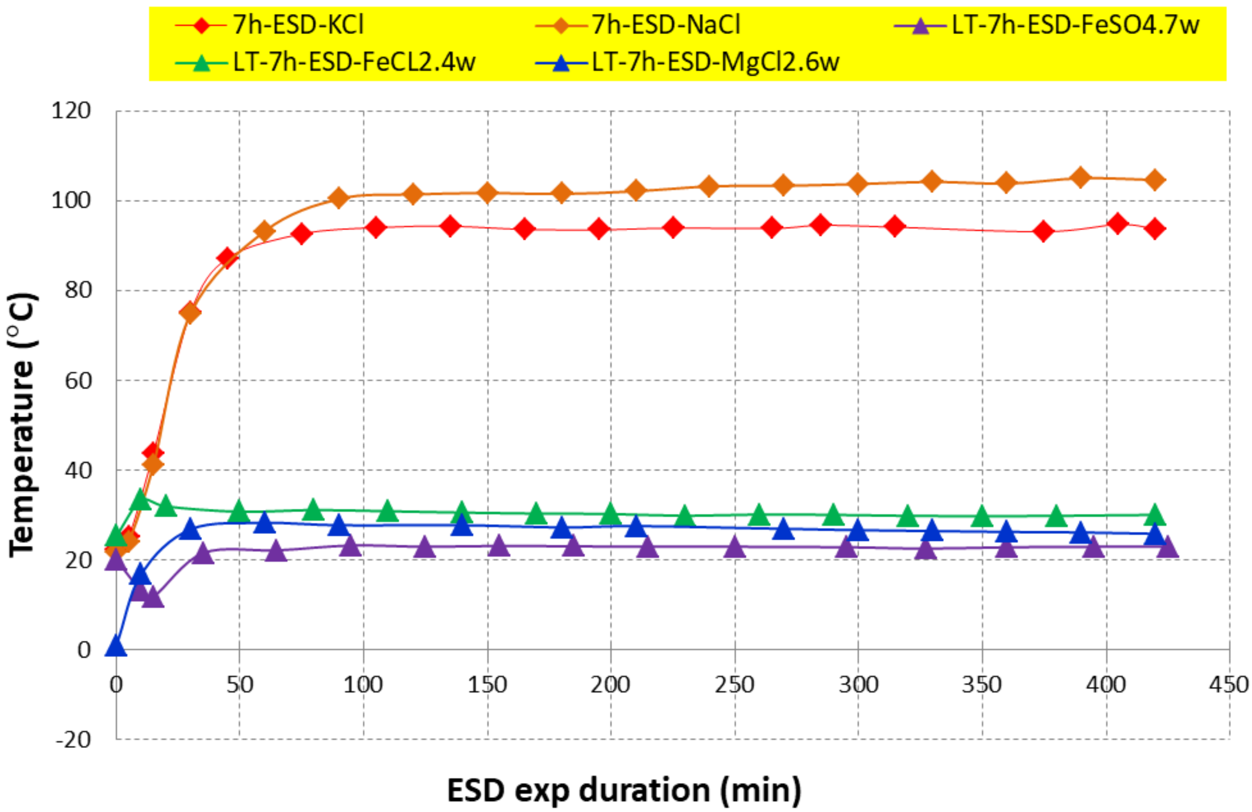

Figure 2. Examples of the equilibrated temperatures T_{eq} during ESD experiments on studied salts

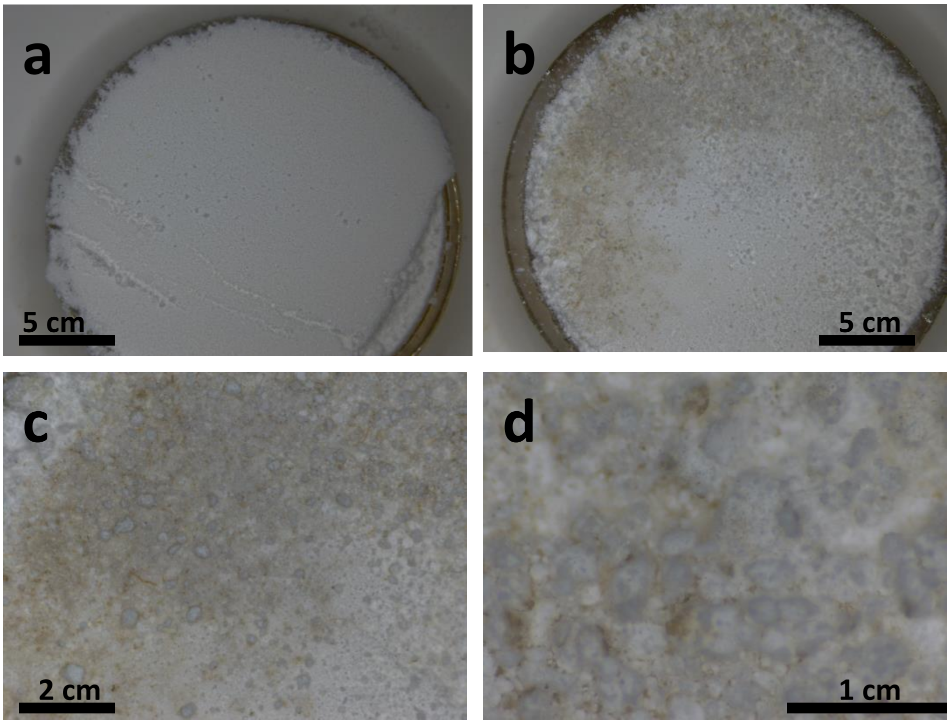

Figure 3. (a) starting $MgCl_2 \cdot 6H_2O$ in a SiO2 cell; (b, c, d) LT-7h ESD product of $MgCl_2 \cdot 6H_2O$ (in a SiO2 cell, and zoom-in)

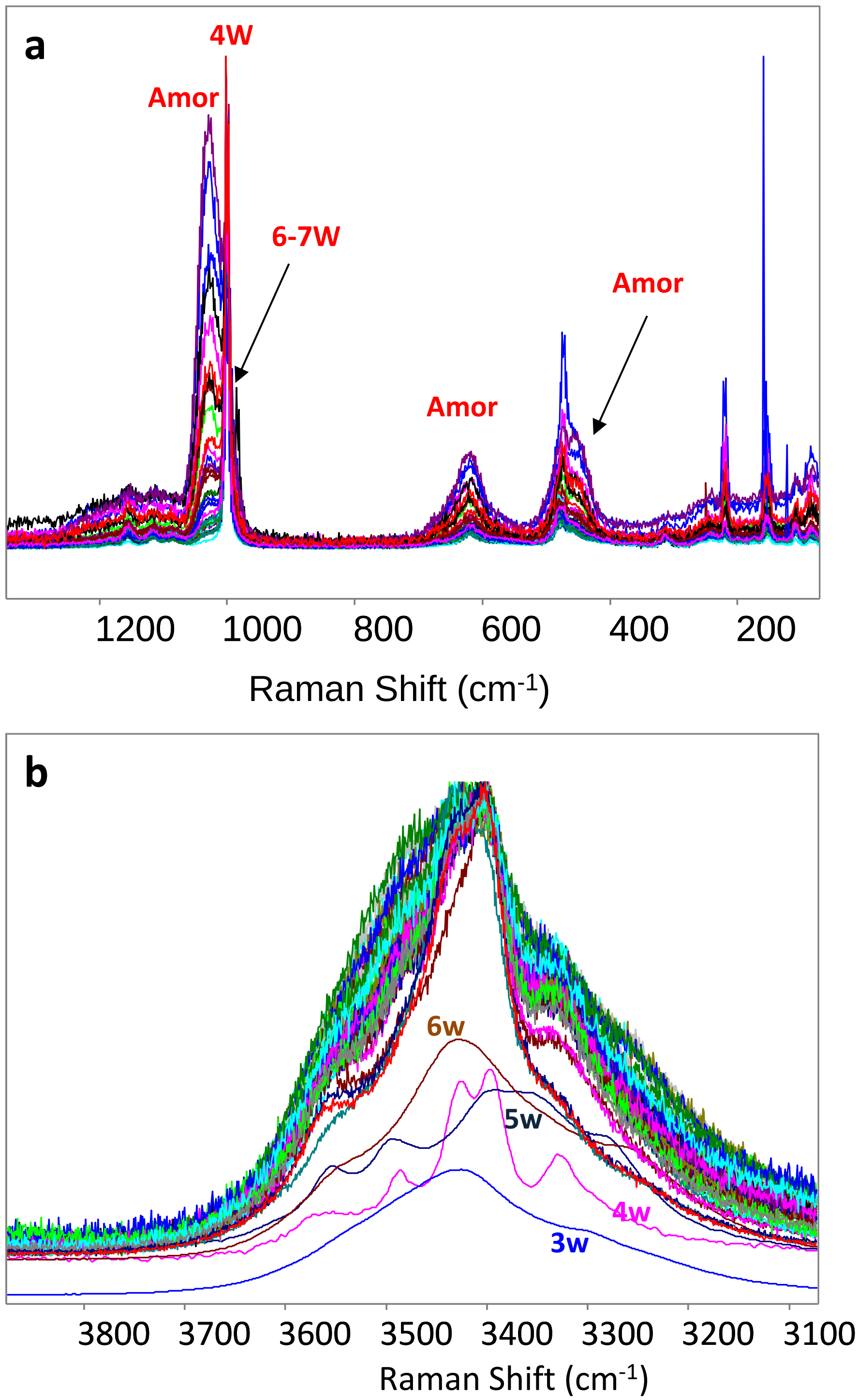

Figure 4. Raman spectra of 0.25h ESD products from $MgSO_4 \cdot 7H_2O$ in (a) spectral range of fundamental vibrational modes; (b) spectral range of H_2O modes, which are compared with standard Raman spectra of $MgSO_4 \cdot 3H_2O$ (3w), $MgSO_4 \cdot 4H_2O$ (4w), $MgSO_4 \cdot 5H_2O$ (5w), $MgSO_4 \cdot 6H_2O$ (6w).

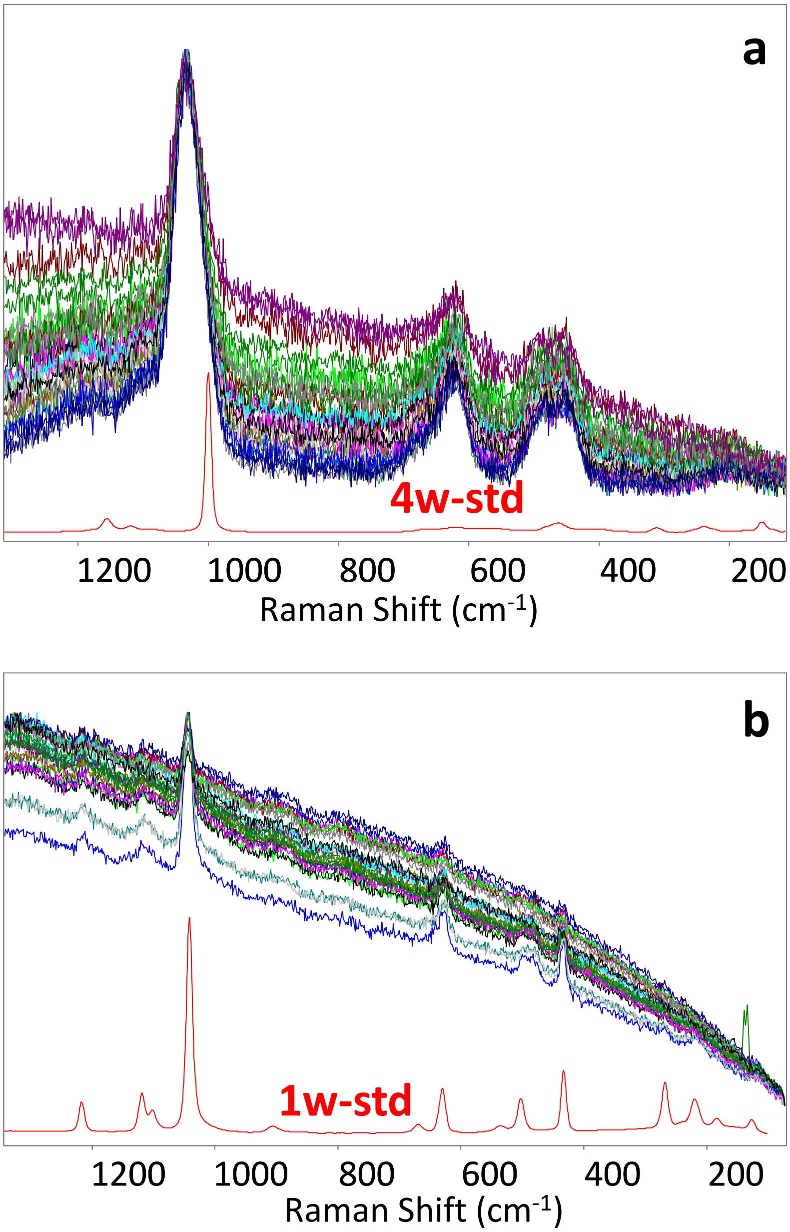

Figure 5. Raman spectra of 1.5h ESD products (a) from $MgSO_4 \cdot 4H_2O$ compared with standard spectrum (4w); (b) from $MgSO_4 \cdot H_2O$ compared with standard spectrum (1w)

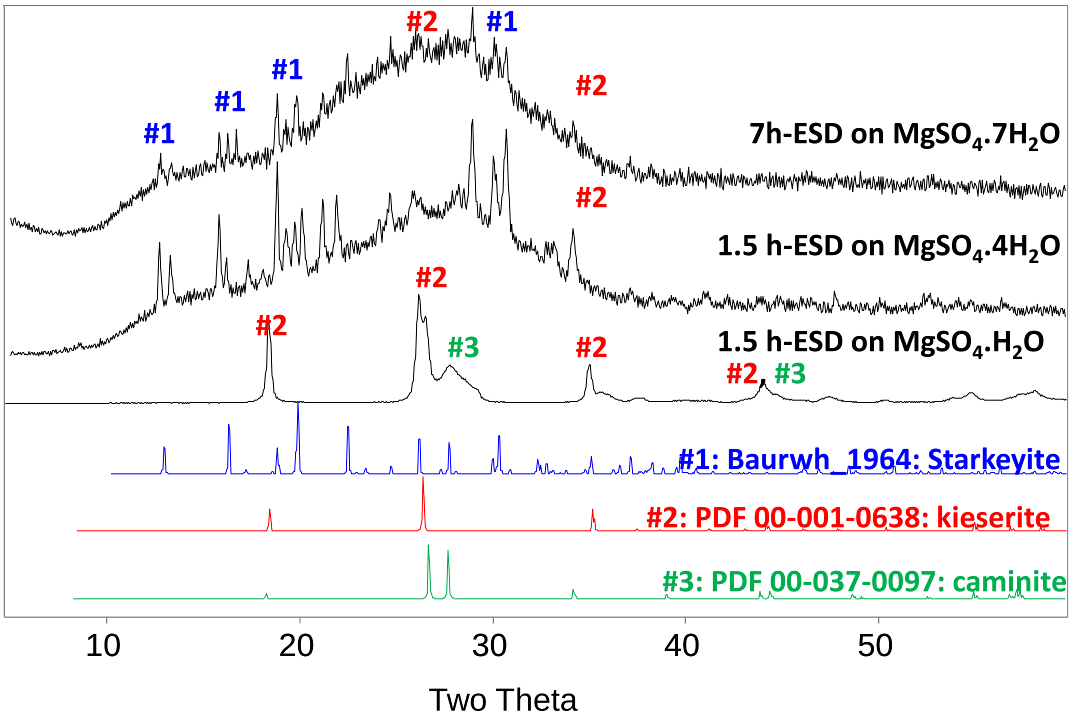

Figure 6. XRD results of ESD products from $MgSO_4·7H_2O$, $MgSO_4·4H_2O$. $MgSO_4·H_2O$, compared with standard XRD patterns of starkeyite ($MgSO_4·4H_2O$), Kieserite ($MgSO_4·H_2O$), and caminite ($MgSO_4·xMg(OH)_2·$ $(1-2x)H_2O$).

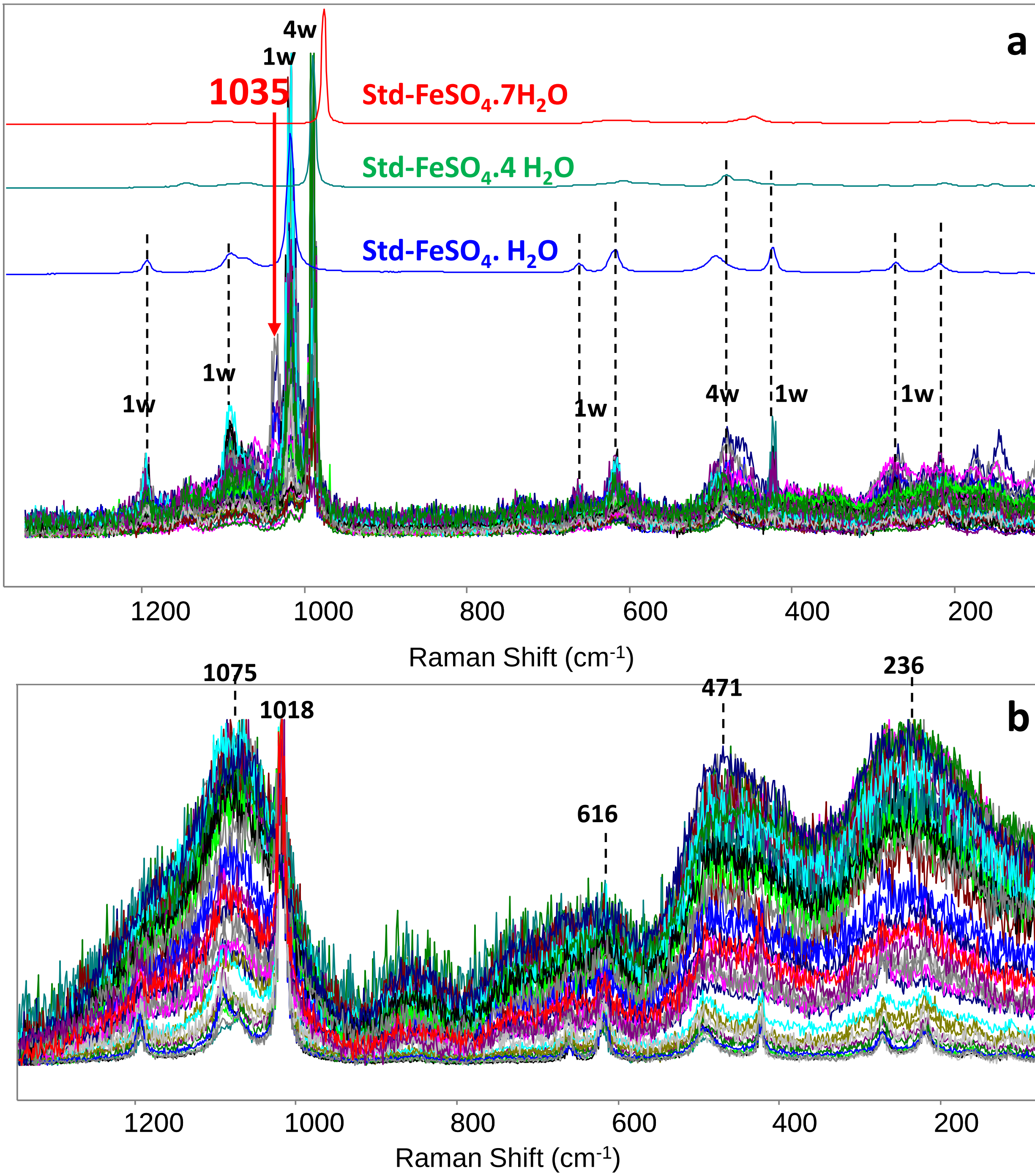

Figure 7. Raman spectra of LT-ESD products from $FeSO_4{\cdot}7H_2O$ (using 1% laser power=0.5 mw, Teq < 30°C); (a) First 60 spectra from a 99-spots Raman analysis on *as is* surface of 0.25h LT-ESD product, compared with standard Raman spectra; (b) first 60 spectra of a 120 Raman analysis on as is surface of LT-7h ESD product.

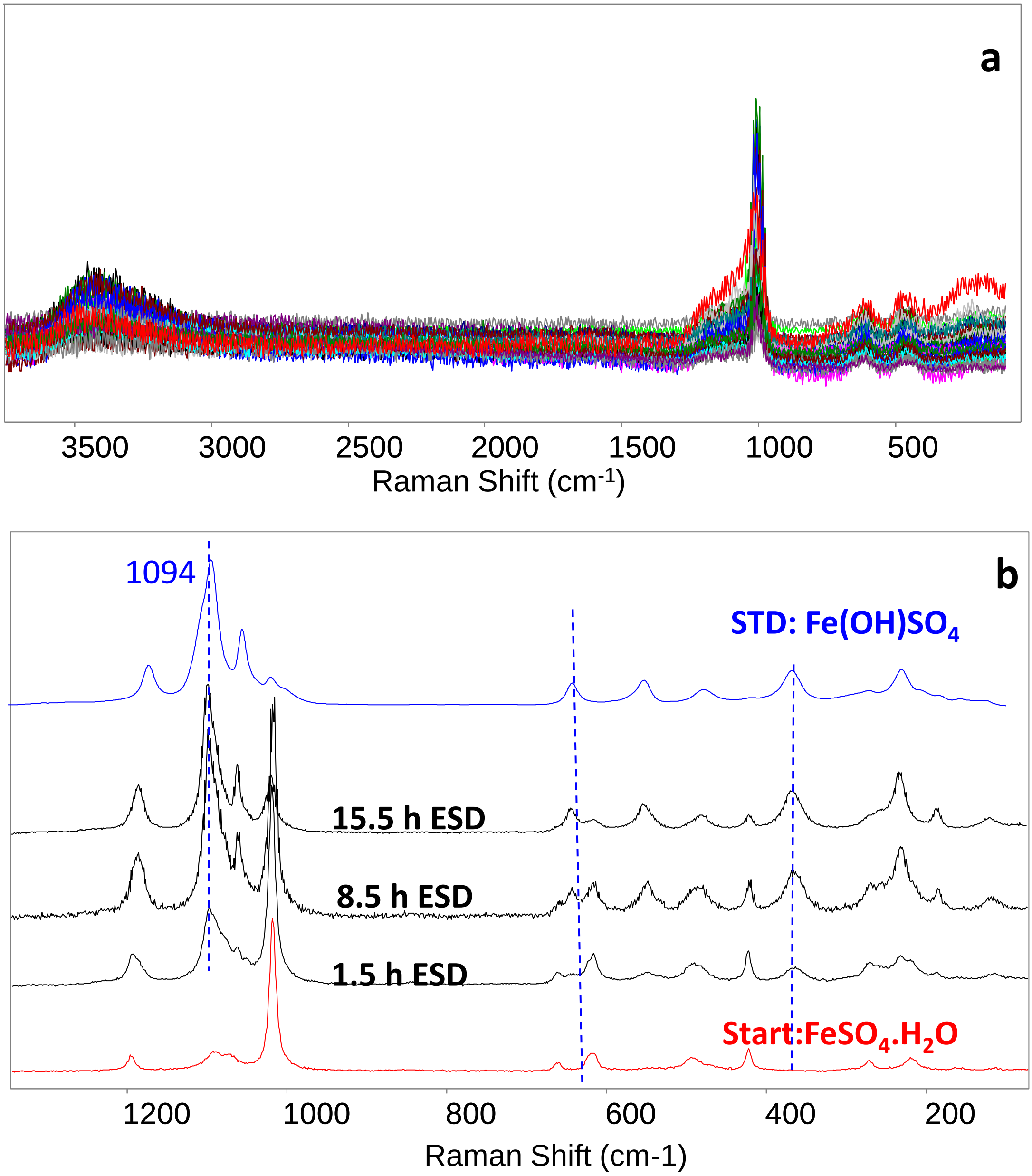

Figure 8. Raman spectra of ESD products: (a) 1.5h-ESD product from $FeSO_4 \cdot 4H_2O$; (b) products after 1.5h, 8.5h, 15.5h ESD process from $FeSO_4 \cdot H_2O$, compared with standard spectra.

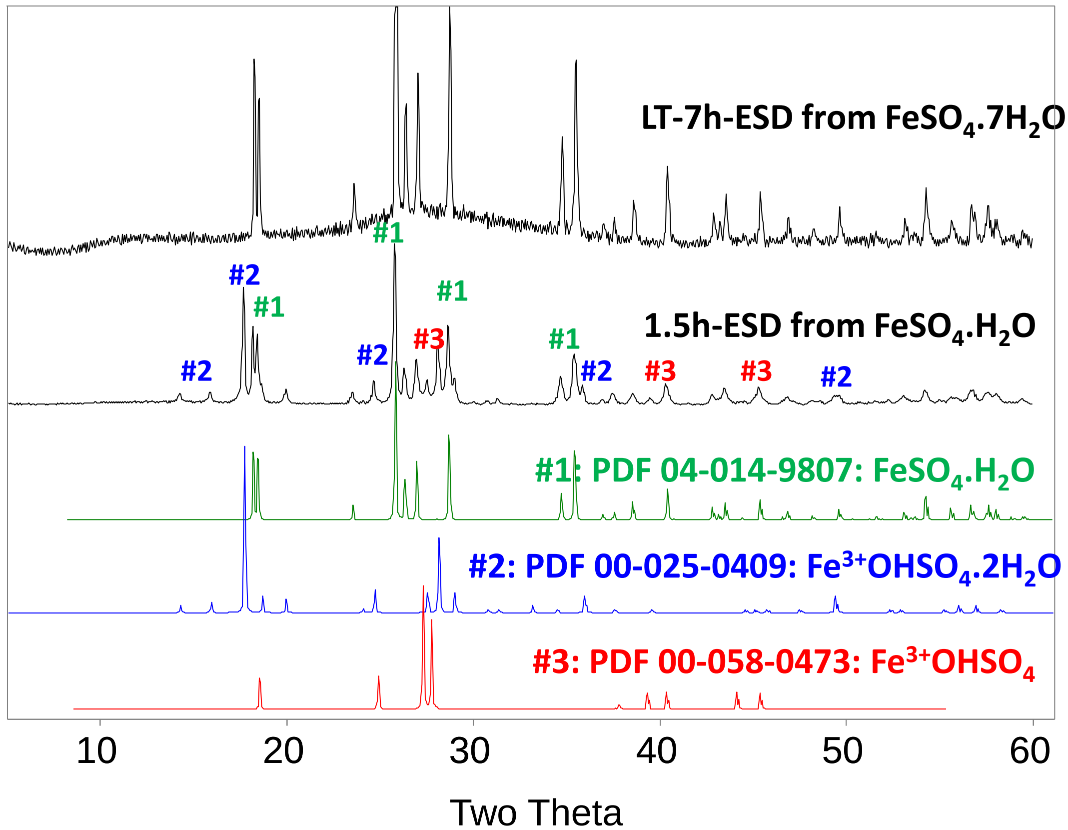

Figure 9. XRD result of LT-7h ESD product (bulk sample) from melanterite $FeSO_4 \cdot 7H_2O$ and szomolnokite $FeSO_4 \cdot H_2O$, compared with standard.

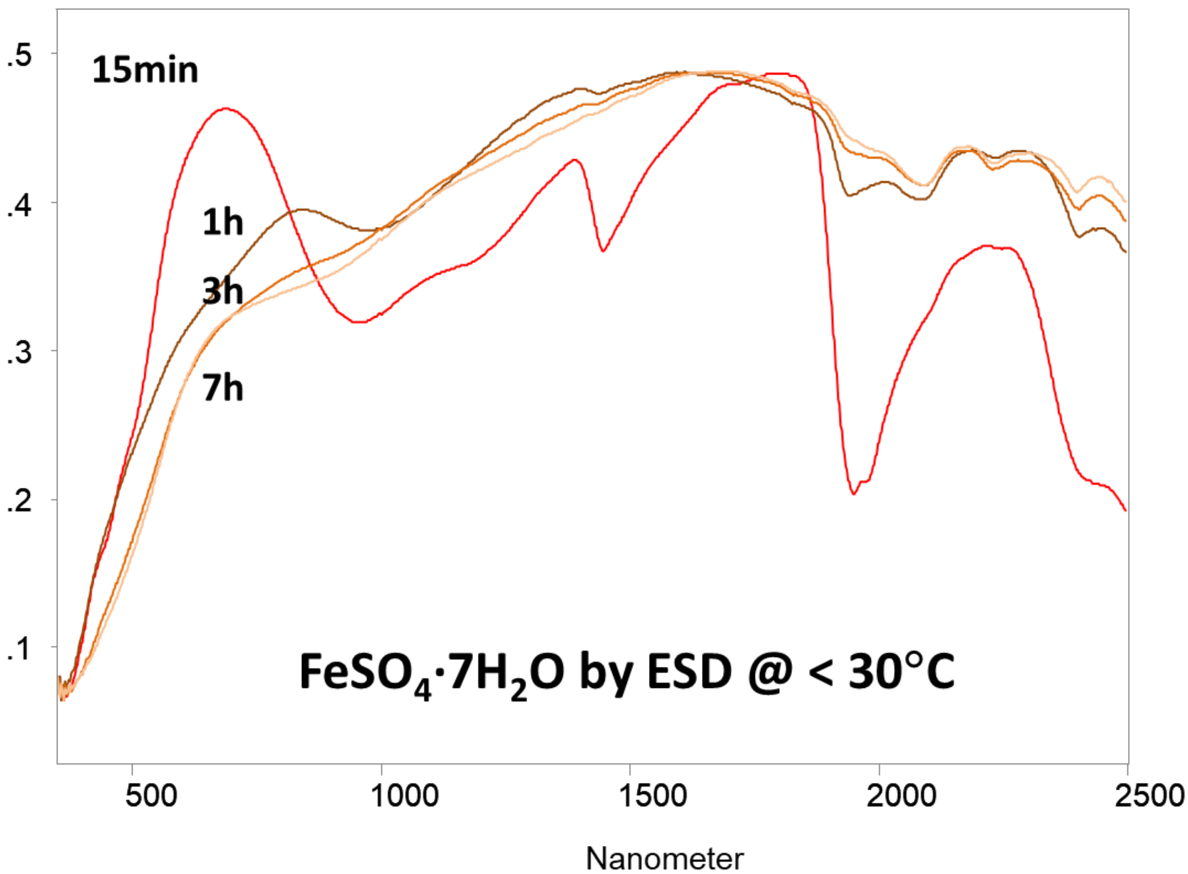

Figure 10. VNIR spectra on as is surfaces of 0.25h, 1h, 3h, 7h LT-ESD (T_{eq}<30°C) from melanterite $FeSO_4·7H_2O$.

JGR: Planets

Supporting Information for

Amorphization of S, Cl-salts Induced by Martian Dust Activities

Alian Wang[1], Yuanchao Yan[1], Darby M. Dyar[2], Jen L. Houghton[1], William M. Farrell[3], Bradley L. Jolliff[1], Scott M. McLennan[4], Erbin Shi[1,5], Hongkun Qu[1,5]

[1]Dept. Earth & Planetary Sciences and McDonnell Center for the Space Sciences, Washington University in St. Louis (alianw@levee.wustl.edu),

[2]Planetary Science Institute, 1700 E. Fort Lowell, Suite 106, Tucson, AZ 85719.

[3]Solar System Exploration Division, Goddard Space Flight Center (GSFC), NASA, USA.

[4]Dept. Geoscience, Stony Brook University, Stony Brook, NY 11794

[5]Dept. Physics and Space Sciences, Shandong University at Weihai, China.

Contents of this file

Table S1. Electron flux

Table S2. MSL-REMS Weibull probability density function

Figure S1. Photos of 0.25h, 1h, 3h, 7h ESD products from melanterite, $FeSO_4 \cdot 7H_2O$.

Figure S2. Photo of Na-jarosite after 35h and 64h ESD.

Figure S3. Raman spectra of 64h ESD product from Na-jarosite. Raman sampled spots are from dark area on *as is* surface.

Figure S4. Mössbauer spectrum and curve fitting results of post 64h ESD jarosite.

Figure S5. Raman spectra of 7h ESD product from akaganeite.

Figure S6. Raman spectra on *as is* surface of 14h ESD product from pyrite. They have the peak ranges of 378.5 – 368.8 (Δ =9.7) cm^{-1} and 342,0 – 337.0 (Δ=5.0) cm^{-1}; while the original natural pyrite sample (from Huanzala, Peru) has much narrow peak ranges of 379.8 – 374.6 (Δ=5.2) cm^{-1} and 344.4 – 340.6 (Δ =3.7) cm^{-1}. In addition, doublet occurs frequently that does not exist in the spectra of original pyrite.

Figure S7. Three types of electrostatic discharge (Gallo 1975).

Figure S8. Plasma spectra generated by ESD in CO_2, CO_2+H_2O, and MSGM (from Figure 4 of Wu et al., 2018)

Introduction

This supporting information document contains two tables and eight figures that provide additional information for the observations presented in this manuscript.

Table S1 lists the derived electron flux in the ESD experiments based on the current measurement (~ 22 mA, same value to that of Wu et al., 2018), which is 1.42×10^{20} $s^{-1}m^{-2}$. When compared with the calculated electron fluxes based on modeled value for ESD-*Townsend dark discharge (TDD) and ESD-normal glow discharge (NGD)(Delory et al., 2006),* 9×10^{16} $s^{-1}m^{-2}$ *(TDD)* and 1.5×10^{24} $s^{-1}m^{-2}$ *(NGD)*, we can conclude that the electron flux density realized in our experiments has a strength mid-way between ESD-TDD and ESD-NGD.

Table S2 lists the Weibull probability density function calculated used the Weibull parameters obtained from the curve fit of REMS data from sol 9 to sol 1474 (1465 sols =2.19 Mars year): Cc=6.87 m/s, k=1.73, into the Weibull probability density function: f(v)=(k/c)(v/c)^(k-1)exp(-(v/c)^k). (Viudex-Mpreiras et al., 2019)

Figure S1 supports section 4.2.1 ESD products from FeSO4.xH2O (x=1, 4, 7), especially the Mossbauer analysis results.

Figure S2-S6 support section 4.1.3.2 ESD products from Na-jarosite, akaganeite, and pyrite that show no obvious phase changes after 7h, 14h, 64h ESD processes on those minerals.

Figure S7 support the discussion in section 6. Implications for martian dust activities, especially about the major differences between Townsend dark discharge (TDD), or normal glow discharge (NGD) is in electron flux density (Gallo 1975).

Figure S8 (from Figure 4 of Wu et al., 2018) supports the statement in abstract and section 2 on the generation of “free Radicals” by ESD process in CO_2, CO_2+H_2O, and MSGM, shown as their emission lines in plasma spectra.

Table S1. Calculated electron flux of our ESD experiments which is same as Wu et al (2018) compared with modeled ESD-TDD and ESD-NGD (Delory et al., 2006).

ESD-NGD of Wu et al., 2018:					
current in mA	**current in C/s**	**number of electron per second (1/s)**	**electrode diameter (m)**	**electrode area (m^2)**	**electron flux (number of electron/(s*m ^2))**
22	0.022	1.37E+17	0.035	0.000962	**1.43E+20**
Delory et al., 2006, Figure 4 & 5					
			electron drift velocity (m/s) by Delory model [3]	**electron density (Ne/m^3) by Delory model**	**electron flux (number of electron/(s*m ^2)) by Delory model**
BEFT of ESD_TDD = 25 kV/m (Farrell et al., 2015)			3.00E+05	3.00E+11	**9.00E+16**
BEFT of ESD_NGD = 34 kV/m (Yan et al., 2017)			3.00E+05	5.00E+18	**1.50E+24**

[1]. 1 ampere (A) =1 Coulomb/s, 1 Coulomb =6.238729x10^{18} electron charge, 1 eV =1.6x10^{-19} Joule
[2]. Electrode: diameter=0.035mm, area=0.000962 m^2
[3]. Assuming the electron drift velocities for ESD-TDD and ESD-NGD are very similar

Table S2. MSL_REMS Weibull probability density function (Viudex-Mpreiras et al., 2019)

Weibull probability density function: f(v)=(k/c)(v/c)^(k-1)exp(-(v/c)^k)

The obtained Weibull Parameters based on curve fit of REMS data from sol 9 to sol 1474 (1465 sols =2.19 Mars year): Cc=6.87 m/s, k=1.73

v (m/s)	k/c	v/c	(v/c)^k-1	(v/c)^k	exp(-(v/c)^k)	**f(V)**	**area**	**< 3.5 m/s**	**< 5 m/s**	**< 7 m/s**	**< 10 m/s**	**< 15 m/s**	**< 20 m/s**
0	0.2518	0.0000	0.0000	0.0000	1.0000	0.0000							
0.5	0.2518	0.0728	0.1477	0.0107	0.9893	0.0368	0.0184						
1	0.2518	0.1456	0.2449	0.0357	0.9650	0.0595	0.0298						
1.5	0.2518	0.2183	0.3293	0.0719	0.9306	0.0772	0.0386						
2	0.2518	0.2911	0.4062	0.1183	0.8885	0.0909	0.0454						
2.5	0.2518	0.3639	0.4781	0.1740	0.8403	0.1012	0.0506						
3	0.2518	0.4367	0.5462	0.2385	0.7878	0.1084	0.0542						
3.5	0.2518	0.5095	0.6112	0.3114	0.7324	0.1127	0.0564	**0.2933**					
4	0.2518	0.5822	0.6738	0.3923	0.6755	0.1146	0.0573						
4.5	0.2518	0.6550	0.7343	0.4810	0.6182	0.1143	0.0572						
5	0.2518	0.7278	0.7930	0.5771	0.5615	0.1121	0.0561		**0.4638**				
5.5	0.2518	0.8006	0.8501	0.6806	0.5063	0.1084	0.0542						
6	0.2518	0.8734	0.9059	0.7912	0.4533	0.1034	0.0517						
6.5	0.2518	0.9461	0.9604	0.9087	0.4031	0.0975	0.0487						
7	0.2518	1.0189	1.0138	1.0330	0.3560	0.0909	0.0454			**0.6639**			
7.5	0.2518	1.0917	1.0661	1.1639	0.3123	0.0838	0.0419						
8	0.2518	1.1645	1.1176	1.3014	0.2722	0.0766	0.0383						
8.5	0.2518	1.2373	1.1681	1.4453	0.2357	0.0693	0.0347						
9	0.2518	1.3100	1.2179	1.5955	0.2028	0.0622	0.0311						
9.5	0.2518	1.3828	1.2670	1.7520	0.1734	0.0553	0.0277						
10	0.2518	1.4556	1.3153	1.9145	0.1474	0.0488	0.0244				**0.8620**		
10.5	0.2518	1.5284	1.3630	2.0832	0.1245	0.0427	0.0214						
11	0.2518	1.6012	1.4101	2.2577	0.1046	0.0371	0.0186						
11.5	0.2518	1.6739	1.4566	2.4382	0.0873	0.0320	0.0160						
12	0.2518	1.7467	1.5025	2.6245	0.0725	0.0274	0.0137						
12.5	0.2518	1.8195	1.5480	2.8166	0.0598	0.0233	0.0117						
13	0.2518	1.8923	1.5929	3.0143	0.0491	0.0197	0.0098						
13.5	0.2518	1.9651	1.6374	3.2177	0.0400	0.0165	0.0083						
14	0.2518	2.0378	1.6815	3.4266	0.0325	0.0138	0.0069						
14.5	0.2518	2.1106	1.7251	3.6411	0.0262	0.0114	0.0057						
15	0.2518	2.1834	1.7683	3.8610	0.0210	0.0094	0.0047					**0.9786**	
15.5	0.2518	2.2562	1.8112	4.0864	0.0168	0.0077	0.0038						

16	0.2518	2.3290	1.8537	4.3171	0.0133	0.0062	0.0031						
16.5	0.2518	2.4017	1.8958	4.5532	0.0105	0.0050	0.0025						
17	0.2518	2.4745	1.9375	4.7945	0.0083	0.0040	0.0020						
17.5	0.2518	2.5473	1.9790	5.0410	0.0065	0.0032	0.0016						
18	0.2518	2.6201	2.0201	5.2928	0.0050	0.0026	0.0013						
18.5	0.2518	2.6929	2.0609	5.5497	0.0039	0.0020	0.0010						
19	0.2518	2.7656	2.1014	5.8118	0.0030	0.0016	0.0008						
19.5	0.2518	2.8384	2.1416	6.0789	0.0023	0.0012	0.0006						
20	0.2518	2.9112	2.1816	6.3511	0.0017	0.0010	0.0005						**0.9959**
20.5	0.2518	2.9840	2.2213	6.6283	0.0013	0.0007	0.0004						
21	0.2518	3.0568	2.2607	6.9104	0.0010	0.0006	0.0003						
21.5	0.2518	3.1295	2.2999	7.1975	0.0007	0.0004	0.0002						
22	0.2518	3.2023	2.3388	7.4896	0.0006	0.0003	0.0002						
22.5	0.2518	3.2751	2.3775	7.7865	0.0004	0.0002	0.0001						
23	0.2518	3.3479	2.4159	8.0882	0.0003	0.0002	0.0001						
23.5	0.2518	3.4207	2.4542	8.3948	0.0002	0.0001	0.0001						
24	0.2518	3.4934	2.4922	8.7062	0.0002	0.0001	0.0001						
24.5	0.2518	3.5662	2.5300	9.0224	0.0001	0.0001	0.0000						
25	0.2518	3.6390	2.5675	9.3433	0.0001	0.0001	0.0000						

Probability of wind speed (in the 2.19 Mars year)

> 3.5 m/s	> 5m/s	> 7m/s	> 10 m/s	> 15 m/s	> 20 m/s
0.7040	**0.5335**	**0.3334**	**0.1354**	**0.0187**	**0.0014**

Figure S1. Photos of 0.25h, 1h, 3h, 7h ESD products from melanterite, $FeSO_4{\cdot}7H_2O$.

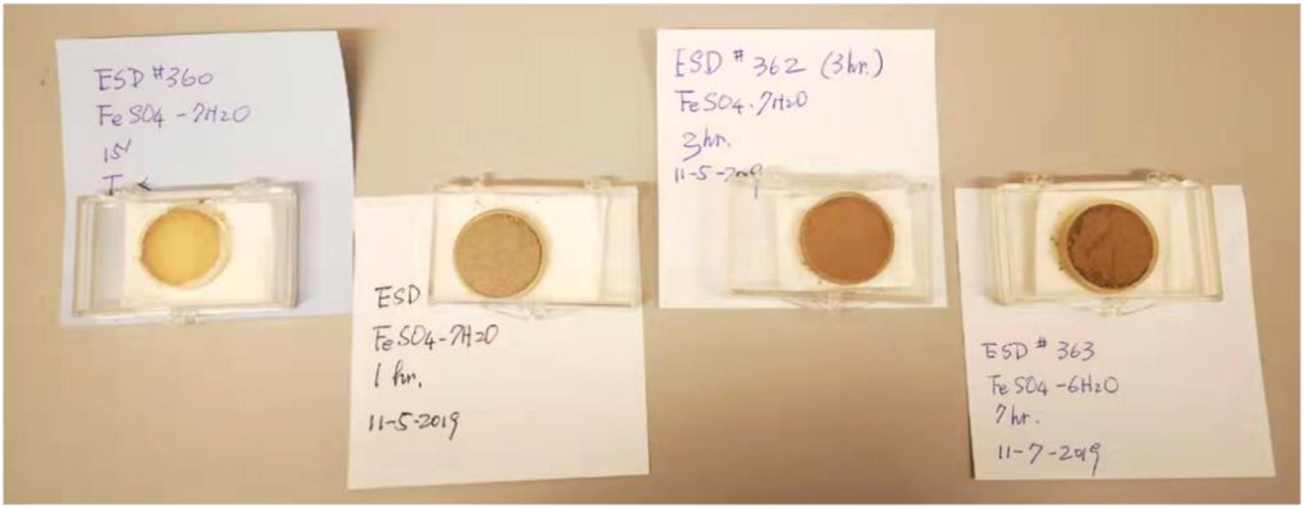

Figure S2. Photos of Na-jarosite after 35h and 64h ESD.

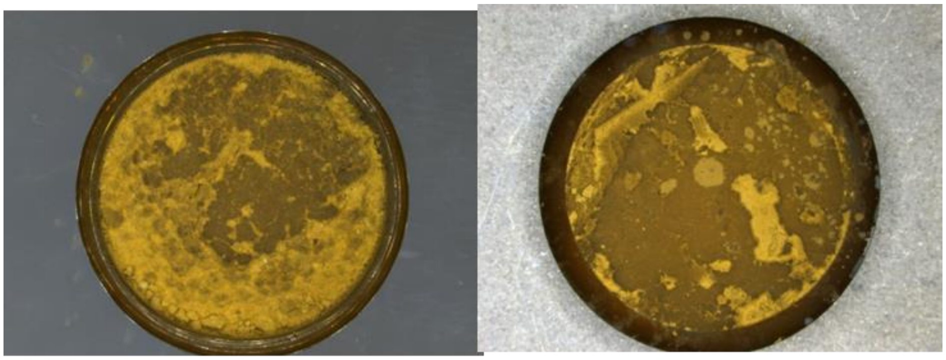

After 35h-ESD After 64h-ESD

Figure S3. Raman spectra of 64h ESD product from Na-jarosite. Raman sampled spots are from dark area on *as is* surface.

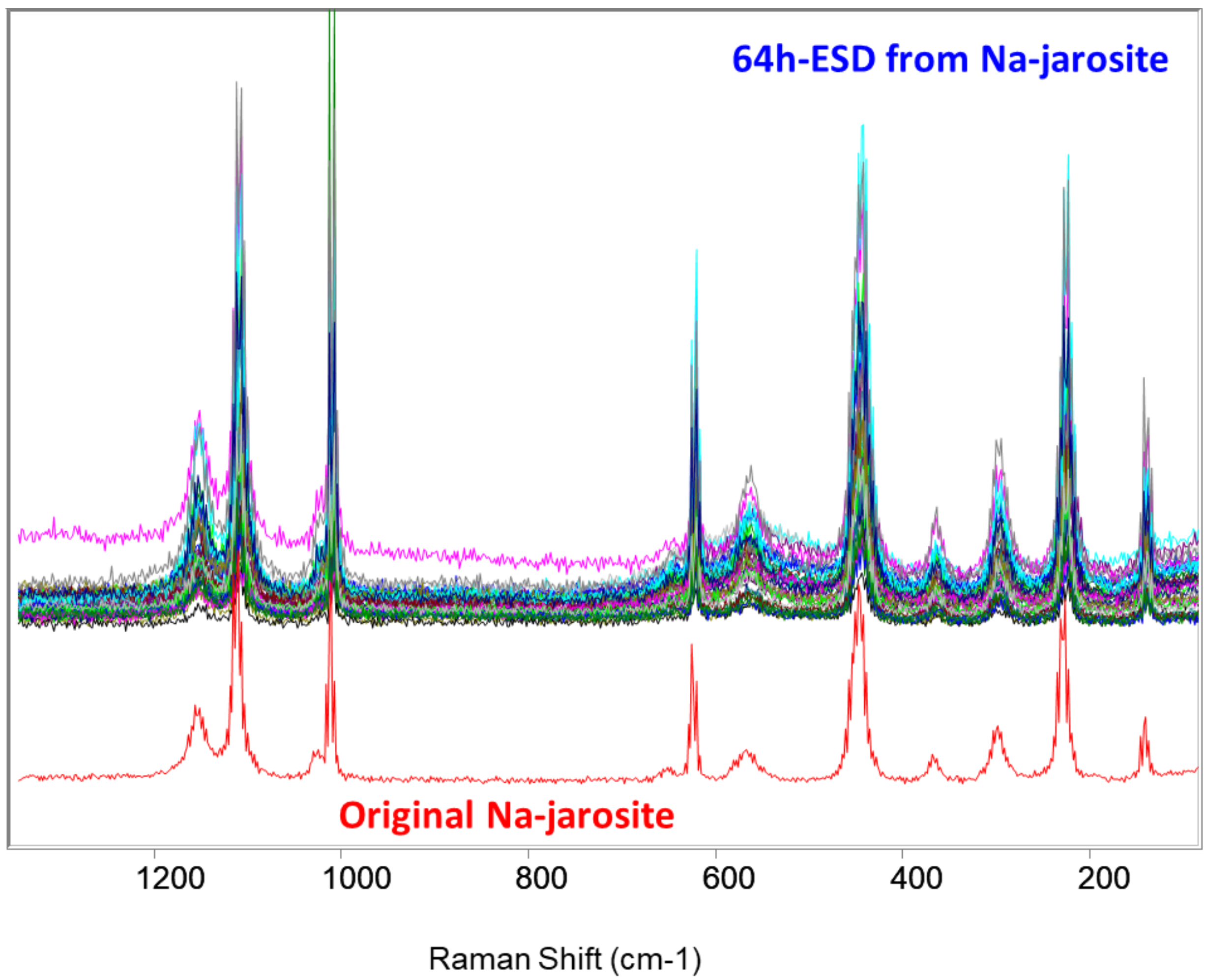

Figure S4. Mössbauer spectrum and curve fitting results of post 64h ESD jarosite.

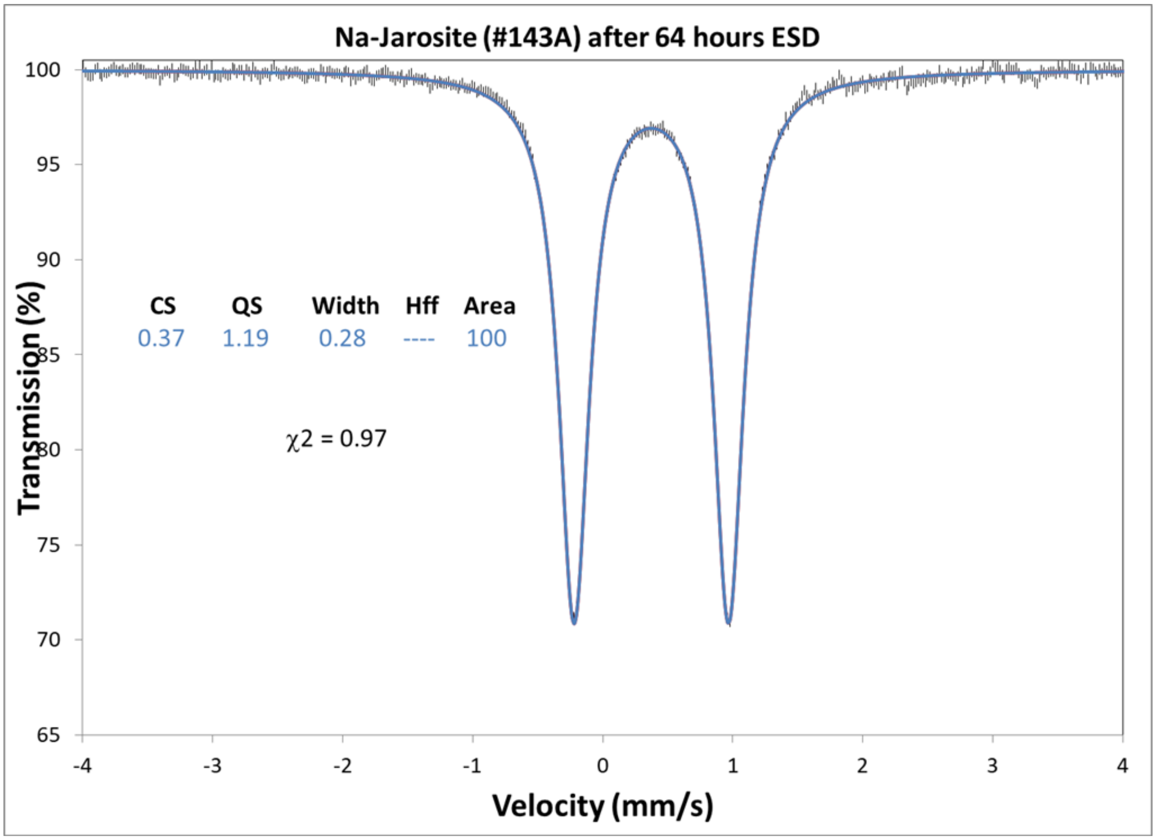

Figure S5. Raman spectra of 7h ESD product from akaganeite.

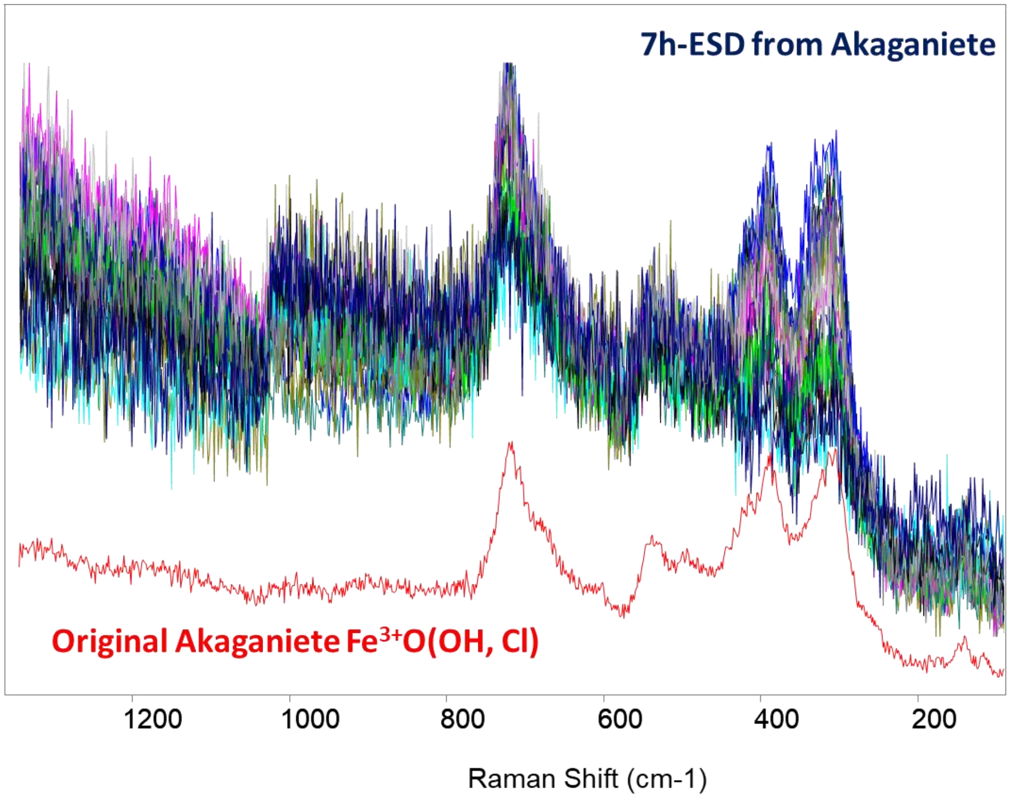

Figure S6. Raman spectra on *as is* surface of 14h ESD product from pyrite. They have the peak ranges of 378.5 – 368.8 (Δ =9.7) cm^{-1} and 342,0 – 337.0 (Δ=5.0) cm^{-1}; while the original natural pyrite sample (from Huanzala, Peru) has much narrow peak ranges of 379.8 – 374.6 (Δ=5.2) cm^{-1} and 344.4 – 340.6 (Δ =3.7) cm^{-1}. In addition, doublet occurs frequently in ESD products that does not exist in the spectra of original pyrite.

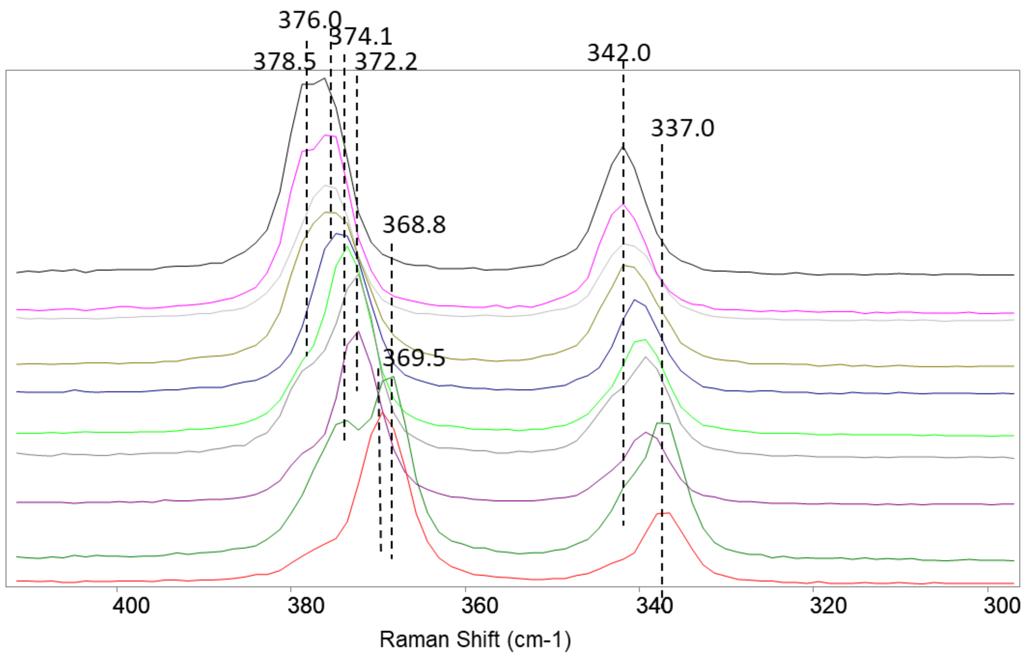

Figure S7. Three types of electrostatic discharge (Gallo 1975).

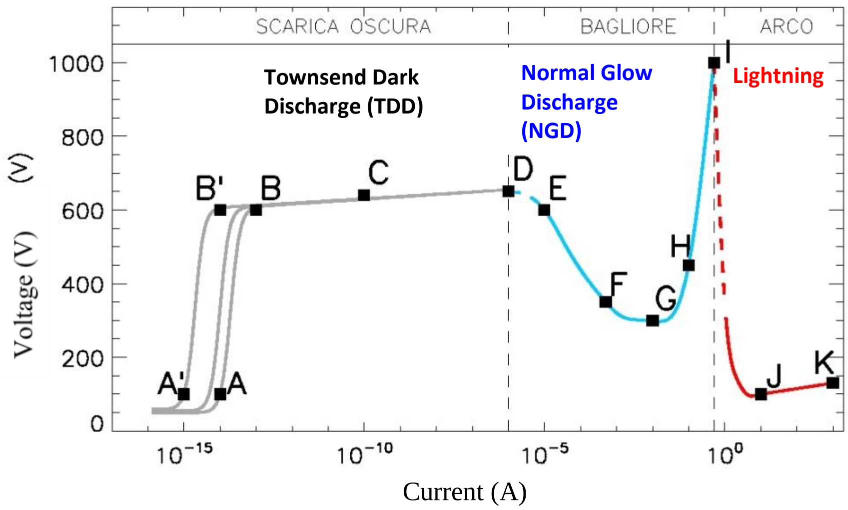

Figure S8 (from Figure 4 of Wu et al., 2018). Plasma emission spectra generated by ESD in PEACh within three different atmospheric environments at room temperature (a) in dry CO_2 (3.0 mbar); (b) in CO_2+H_2O (6.2 mbar, 7.2 %RH); (c) in Mars Simulate Gas Mixture (MSGM, CO_2 95%, N_2 2%, Ar 2%, O_2 1%, 3.0 mbar).

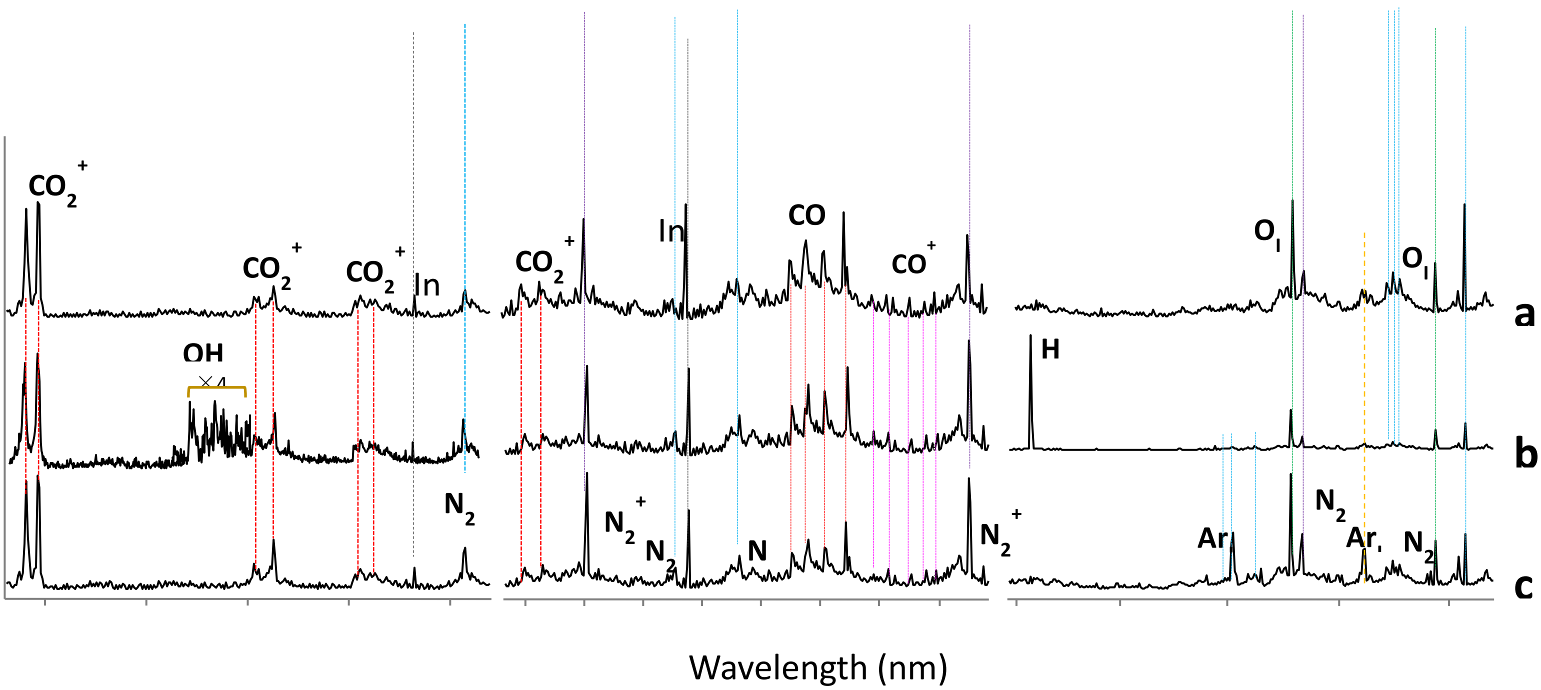

Amorphization of S, Cl-salts induced by Martian Dust Activities

Alian Wang[1], Yuanchao Yan[1], Darby M. Dyar[2], Jen L. Houghton[1], William M. Farrell[3], Bradley L. Jolliff[1], Scott M. McLennan[4], Erbin Shi[1,5], Hongkun Qu[1,5]

[1]Dept. Earth & Planetary Sciences and McDonnell Center for the Space Sciences, Washington University in St. Louis (alianw@levee.wustl.edu),
[2]Planetary Science Institute, 1700 E. Fort Lowell, Suite 106, Tucson, AZ 85719.
[3]Solar System Exploration Division, Goddard Space Flight Center (GSFC), NASA, USA.
[4]Dept. Geoscience, Stony Brook University, Stony Brook, NY 11794
[5]Dept. Physics and Space Sciences, Shandong University at Weihai, China.

Corresponding author: Alian Wang

Key points

- Amorphization of S and Cl salts was induced by electrostatic discharge (ESD) in a Mars chamber that simulates martian dust activities.
- Amorphization is commonly accompanied by dehydration of salts and the oxidation of Fe, Cl, and S species.
- Dust activities may have generated and deposited large quantities of S- and Cl-rich amorphous materials all over the martian surface.

Abstract

A high proportion of non-crystalline (X-ray-amorphous) components has been found in all samples analyzed by CheMin on the *Curiosity rover* at Gale crater on Mars, and such X-ray-amorphous components probably occur at all sites that have been investigated thus far by landers and rovers. The amorphous material at Gale crater is rich in volatiles (S, Cl, and H_2O), as indicated by other science payload elements (APXS, SAM). We demonstrate here that amorphization of S and Cl salts can be induced by energetic electrons and free radicals generated in a medium-strength electrostatic discharge (ESD) process during martian dust activities such as dust storms, dust devils, and grain saltation. Furthermore, we found that the amorphization is commonly accompanied by dehydration of the salts and oxidation of Cl, S, and Fe species. On the basis of experimentally observed rates of the above phase transformations and the mission-observed dust activities and wind speeds on Mars, we anticipate that similar phase transformations could occur on Mars within a time frame of years to hundreds of years. Considering the high frequency, long duration, and large areal coverage of Martian dust activities, our study suggests that the ESD induced by Martian dust activities may have contributed to some the S- and Cl-rich portion of X-ray amorphous materials observed in surface soils at Gale crater. Furthermore, dust activities in the Amazonian period may have generated and deposited a significant quantity of S- and Cl-rich amorphous materials all over Mars.

Plan language summary

Martian dust activities have been altering the look of the surface of Mars, by the blast of particles of various sizes. In addition, frictional electrification in these events would charge the particles, and the charged particles would be further spatially separated by wind at the same time, to form an electric field like those formed in the cloud layers on Earth. Electrostatic discharge (ESD) would occur when enough charges are accumulated. Unlike the lightning on Earth, another two types of ESD, Townsend dark discharge (TDD) and normal glow discharge (NGD) would more likely occur on Mars because of its thin atmosphere. The electrostatic discharge (ESD) would induce electrochemical reactions and change Martian surface materials. Our new simulated ESD experiments revealed three types of phase changes can occur in S and Cl salts. They are amorphization (damage of crystal structure), dehydration (loss of structural water), and oxidation of Cl, S, and Fe. Because of the high occurring frequency, the large area coverage, and long duration of dust events during the recent Amazonian period on Mars, our results imply that Martian dust activities may have generated and deposited a large quantity of S- and Cl-rich amorphous materials all over the surface of Mars.

1. Introduction

Among many great findings in martian mineralogy, the discovery of X-ray amorphous components in all samples analyzed by CheMin on the *Curiosity* rover at Gale crater (Bish et al., 2013, Blake et al., 2013, Vaniman et al., 2014) has been an eye-opening discovery. The proportion of X-ray amorphous components in different martian samples ranges from ~19-36 wt% in active and inactive dune materials, to ~ 20-56 wt% in all mudstones, and ~ 14-71 wt% in altered and less-altered Stimson formation samples (the lowest estimated percentages based on Table 1 and Table 10 of Morrison et al., 2018a, which were supported within the uncertainty range of measurements and analyses by Achilles et al., 2017; Morris, et al., 2016; Rampe et al., 2017, 2018; Yen et al., 2017), implying multiple geological processes for producing the X-ray amorphous components.

In the early history of Mars, several geological processes would form species with low crystallinity. These processes include volcanic activity, impacts, hydrothermal activity, and chemical (including acidic) weathering at low temperature that could free (or partially free) molecules or ionic groups in geological materials, but with insufficient time (or energy) for the newly formed phases to reach crystallographic equilibrium, i.e., an ordinary degree of crystallinity.

A phenomenon with equal significance was that the X-ray amorphous components in all Gale crater samples have a high concentration of volatile-element components (e.g., SO_3 and Cl), a conclusion from combined CheMin and APXS data analyses (Dehouck et al., 2014; Morris et al., 2016; Rampe et al., 2017, 2018; Yen et al., 2017; Achilles et al., 2017), based on a newly developed method to refine unit-cell parameters that has increased the accuracy in derived major-mineral chemistry (Morrison et al, 2018b). An overview published by Morrison et al. (2018a) revealed the highest concentration of SO_3 + Cl in the amorphous component of a surface soil (Rocknest), among all 13 samples from Bradbury landing through Naukluft Plateau (from sol 69 to sol 1332) at Gale crater, to be 24.4 wt% for SO_3 and 3.5 wt% for Cl. In addition, the data from the SAM payload on the same set of collected samples support the existence of poorly crystalline magnesium and iron sulfates and the association of water with amorphous phases (Sutter et al. 2017, 2019). A relevant observation made by the *Spirit* and *Opportunity* rovers at Gusev crater and Meridiani Planum, was that a higher content of SO_3 and Cl were found in surface soils and un-brushed rock surfaces than in rock interiors (Yen et al. 2005; Gellert et al., 2006). The S and Cl enrichment nature and the similar molar S/C ratio in air-fall dust were further confirmed by APXS analyses of the Curiosity rover, and were implied to relate to global Martian dust (Berger et al., 2015, Schmidt et al., 2018). A key follow up question is: By what processes could some of the S- and Cl-bearing salts at the martian surface become (or form as) X-ray amorphous materials?

A sudden exposure (by impact or by rover trench, e.g., Byrne et al., 2009; Wang et al., 2006a) of subsurface hydrous sulfates to current atmospheric conditions at the martian surface, as simulated by vacuum desiccation of hydrous salts in laboratory experiments (Sklute et al., 2015; Vaniman et al., 2004; Wang et al., 2006b, Wang and Zhou 2014), could have formed amorphous sulfates directly from crystalline Mg, Fe^{2+}, and Fe^{3+} sulfates. Another process, a sudden release of subsurface brine(s) to the current martian surface with subsequent desiccation may also form non-crystalline salts. Geological processes on present-day Mars that might induce subsurface brine release could be Recurring Slope Lineae (RSL) (McEwen et al., 2014, Wang et al., 2019) and impacts. In a fast brine-dehydration laboratory simulation, amorphous ferric sulfates were first found to form at mid to high temperatures (293-323 K) (Sklute et al., 2015; Wang et al., 2012), and amorphous Mg, Fe^{2+}, Fe^{3+} (but not Ca, K, Na) sulfates formed at 77 K (Morris et al., 2015). Sklute et al. (2018) further revealed the formation of amorphous phases from pure $FeCl_3$ brine (but not from pure $CaCl_2$, $MgCl_2$, and NaCl brines), and from the brines of mixed salts, i.e., $Fe_2(SO_4)_3$ mixed with Na, Mg, Ca, Fe^{3+} chlorides and Na bicarbonate, at room temperature. Toner et al. (2014) observed that amorphous glasses of $Mg(ClO_4)_2$ and $Ca(ClO_4)_2$ formed near 153 K by cooling the relevant brines below their eutectic temperatures. Furthermore, both amorphous Mg and Fe^{3+}sulfates can host structural H_2O to various degrees (up to three structural H_2O per Mg-sulfate molecule, and up to eleven structural H_2O per Fe^{3+}-sulfate molecule), all of which are stable at low relative humidity (RH <11%) and in a wide temperature range (278-323 K) (Wang et al., 2009, 2012).

In addition, energetic particles from space, such as galactic cosmic rays and energetic UV photons, are capable of damaging the crystal structures of surface minerals on airless planetary bodies, while their effect on martian secondary minerals at the surface needs further investigation.

On the basis of the studies referenced above and our previous experimental investigations (Wu et al., 2018, Wang et al., 2020), we hypothesize that S- and Cl-rich X-ray amorphous materials at the surface of Mars may be very common, and one mechanism to produce them is by *multiphase redox plasma chemistry* (or simply, *electrochemistry*) induced by electrostatic discharge (ESD) that occurred during martian dust activities during the Amazonian period. In this manuscript, we report the results of 75 sets of ESD experiments on 22 Mars-relevant minerals under martian atmospheric conditions to explore and test our hypothesis.

We present some background about ESD in martian dust events in section 2, the studied samples and the experiments in section 3, and the results in section 4. We then report the finding of three phase transformation trends in section 5, and discuss the implications of our study in section 6.

2. Martian dust activities, ESD, free radicals, and electrochemistry

Frictional electrification of mineral particles and aerosols can occur in four types of martian surface processes: volcanic eruption, dust storm, dust devil, and grain saltation. Except for volcanic eruptions, the last three processes occur continuously on present-day Mars. For example, regional dust storms occur every martian year and a global dust storm occurs every 6-8 Earth years (Shirley, 2015; Wang and Richardson, 2015). Dust devils have been observed by all landed missions on Mars (Metzger and Carr, 1999; Ferri at al., 2000; Ellehoj et al., 2010; Greeley et al., 2006, 2010; Lemmon et al., 2017; Murphy et al., 2016), as well as remotely by orbital observations (Cantor et al., 2006; Choi and Dundas, 2011; Reiss and Lorentz, 2016; Verba et al., 2010; Whelley and Greeley, 2008). Grain saltation was first confirmed on Mars at Meridiani Planum and Gusev Crater (Sullivan et al., 2005, 2008), with laboratory simulations suggesting that they could be a ubiquitous occurrence on the martian surface (Sullivan and Kok, 2017).

A tendency for triboelectric charge, i.e., generation of negative charges on smaller grains, but positive charges on larger grains of similar composition, was revealed by experiments (Forward et al., 2009; Krauss et al., 2003). Separation of smaller grains from larger grains by convective martian dust events would generate a large-scale charge separation, i.e., *an active electric field (E-field)*. On Earth, E-fields of up to 166 kV/m was detected during grain saltation (Schmidt et al., 1998), and 60 kV/m during the passage of dust devils (Esposito et al., 2016; Farrell et al., 2004; Harrison et al., 2016; Jackson and Farrell, 2006).

When a local E-field accumulates beyond the *breakdown electric field threshold* (BEFT), electrostatic discharge (ESD) can occur. BEFT on Mars is estimated to be ~ 25-34 kV/m from measurements in Mars environmental chambers (Farrell et al., 2015; Yan et al., 2017), slightly higher than ~ 20-25 kV/m from a modeling study (Melnik and Parrot, 1998). This range is about 1% of the BEFT on Earth (~ 3000 kV/m), which matches with martian atmospheric pressure being < 1% that of Earth. Therefore, ESD occurs on Mars much more easily than on Earth. The low BEFT on Mars prevents the accumulation and separation of large amounts of charges, thus lightning would be unlikely to occur. Whereas the other two types of ESD (Gallo, 1975), *Townsend dark discharge (TDD)* and *normal glow discharge (NGD)* would more likely occur on Mars. In a set of experiments simulating grain saltation using silicates under Mars atmospheric composition and pressure, Bak et al. (2017) detected light emissions (red colored glow from quartz sand and blue colored glow from basaltic sand) that are similar to normal glow discharge (NGD) in a Mars chamber simulated in our laboratory (Wang et al., 2020; Wu et al., 2018).

ESD generates a flux of energetic electrons with high speed, i.e., an electron avalanche. These electrons collide with gaseous molecules and atoms in the martian atmosphere, CO_2, O_2, N_2, Ar, and H_2O, to cause electron impact ionization (EII) of CO_2, electron/CO_2 dissociation attachment (ED of CO_2), and electron/H_2O dissociation attachment (ED of H_2O) (Jackson et al., 2010; Wu et al., 2018). The collision generates free radicals, including ions with positive and negative charges, neutral species at excited states, and additional electrons. The last one could cause further chain electron avalanches (Delory et al., 2006).

Above expectations were validated by our experimental observations (Wu et al., 2018) of CO^{2+}, CO^+, O_I, H_{III}, H_{II}, OH, Ar_I, N_2, N_2^+ by *in situ* plasma emission spectroscopy (also O_2, NO, *and* O^+ because of the overlapping of plasma lines used for detection, Figure S8) and O_3 in the output gas by UV and mid-IR spectroscopy (Figure 5 of Wu et al., 2018), generated by normal glow discharge (ESD-NGD) under simulated Mars atmospheric composition and pressure. During a simulated saltation experiment on silicates upon contact of water (Bak et al., 2017), H_2O_2 and ·OH were detected. Furthermore, Aerts et al. (2015) reported CO_2 splitting (to CO and O_2) by dielectric barrier discharge.

These energetic free radicals could react with the molecules in the martian atmosphere and in surface materials. As demonstrated by our previous work, these *multiphase redox plasma chemical reaction* (or simply *electrochemical reaction*) cause the oxidation of chlorine from chloride (Cl^{1-}) to chlorate/perchlorate (Cl^{5+} and Cl^{7+}) (Wu et al., 2018), and the release of Cl atoms at the first excited state (Cl_I) from common chlorides (Wang et al., 2020), instantaneously and apparently with high yields.

3. Samples and Experiments

3.1 Sample selection

In order to validate our hypothesis, i.e., to make our experiments relevant to the volatile portion (high wt% of SO_3 + Cl) of the X-ray amorphous component found on Mars (Dehouck et al., 2013; Morris et al., 2016; Morrison et al., 2018a; Rampe et al., 2017), we selected crystalline sulfates and chlorides as the starting phases for our ESD experiments. For the most part, hydrous salts were used, based on the association of H_2O with amorphous phases suggested by data analyses of SAM (Sutter et al., 2017, 2019). Salts with Mg, Fe^{2+}, Fe^{3+}, Ca, Al, Na, K were selected, based on the findings by recent missions of martian sedimentary minerals, i.e., they are enriched in Mg and Fe, less in Ca, and relatively depleted in Na and K (McLennan and Grotzinger 2008; McLennan, 2012; McLennan et al., 2019). A few relevant samples were added later, including two Na-sulfites, an Fe-sulfide (pyrite), and a Fe-hydroxide (akaganeite). These starting phases are listed in Table 1**.**

Each starting sample for an ESD experiment was ground and sieved. A grain size range of 63-88 µm was selected for all samples. Each powdered sample was placed into a fused-SiO_2 cell with an inner diameter of 22 mm and inner depth of 2 mm, i.e., about 760 mm^3 in volume. Depending on the density of different salts, a total mass of different salts in the range of 400-1100 mg was used. During each ESD experiment (Figure 1), the SiO_2 sample cell was placed in the lower electrode (Figure 1b), facing the energetic electrons from the upper electrode, and was entirely enveloped by the generated plasma (inset of Figure 1).

3.2 ESD experiments

A Planetary Environment and Analysis Chamber (PEACh) at Washington University in St. Louis (Sobron and Wang, 2012) was used for all ESD experiments designed for this study. A combination of needle and ball valves connect the PEACh with a CO_2 gas tank to regulate atmospheric pressure (and composition when desired). The PEACh was first evacuated to 3×10^{-2} mbar to remove the air, and then filled with pure ultra-dry CO_2 for this study. The ESD experiments of this study were conducted with active evacuation and continuous CO_2 in-filling. The pressure was kept at 3 ± 0.1 mbar in each ESD experiment.

As described by Sobron and Wang (2012), the temperature of the sample cell can be controlled by a liquid nitrogen (LN_2) delivery system attached to the PEACh (Figure 1). The LN_2, stored in a dewar outside the PEACh, is heated by a resistor immersed in the LN_2 reservoir, and the evaporated N_2 gas at near-LN_2 temperature is directed via a feedthrough in the PEACh's wall into a toroid-shaped, double-walled copper block (referred to as *the cold plate* hereafter) that sits inside the PEACh. Another feedthrough allows for the evacuation of the nitrogen gas after its circulation through the cold plate. An electronic controller (OMEGA Engineering Inc. CN76000 autotune controller) monitors the temperature of the cold plate via a resistive thermal device and regulates the flow of cold N_2 gas that enters the cold plate. This setup allows the temperature of the cold plate to be kept relatively constant at a desired temperature between 21°C and −100°C with deviations of less than 0.5°C.

The normal glow discharge (NGD) in this set of ESD experiment was generated by two parallelly mounted electrodes in the PEACh (Fig. 1b). They are made of copper, with a diameter of 35 mm. The distance between the two electrodes was adjusted by a motorized precision translation stage (Thorlab PTI-Z8), 6 mm was used in all experiments of this study.

We used AC power (110 V, 50/60 Hz), a contact voltage regulator (No. 2090 VR), and a triggering neon power supply (CPI Advanced Inc., CPI-EZ12, max output 12 kV, 40 mA) that was directly connected to the ESD electrodes in the PEACh. Electric voltage from the upper electrode to the ground, and electric current through the pair of ESD electrodes were recorded every 30 minutes during an ESD experiment, using two multimeters (KEYSIGHT-U1251B). We found the values of electric current is ~ 22 mA, not affected by different starting salts, and is very similar to those reported in Wu et al. (2018) and Wang et al. (2020), i.e., with the same electron flux shown in Table S1.

The electron flux in our current experimental setting is 1.42×10^{20} $s^{-1}m^{-2}$, calculated from the electric current measurement (Table S1), indicating that we used an ESD with a strength midway between the two extreme cases, ESD-TDD and ESD-NGD (ranging from 9×10^{16} $s^{-1}m^{-2}$ (TDD) to 1.5×10^{24} $s^{-1}m^{-2}$ (NGD), detailed discussion in section 5.3 of Wu et al., 2018) to process all selected starting phases. Another important parameter is the kinetic energy of ESD generated electrons, for which we use the observed free radicals and relevant reactions to make estimation. For example, CO_2^+ was the dominant species generated by the same ESD setup in CO_2 (Figure 4a, b, c, and Table 1 of Wu et al., 2018), and it is a product of electron impact ionization (EII) of CO_2 (Delory et al., 2006; Jackson et al., 2010). The occurrence of EII of CO_2 in our ESD experiment revealed that a considerable portion of ESD generated electrons has a kinetic energy >14 eV. Furthermore, a very strong Hα line at 656.3 nm was observed by *in situ* plasma spectroscopy at extremely low P_{H2O} (Fig. 4b, d, e of Wu et al., 2018) or when the starting mineral is hydrous salt. This line is generated by a transition from H_{III} to H_{II} that indicates the presence of electrons with a kinetic energy > 17.19 eV to excite hydrogen to H_{III} (Delory et al., 2006, Itikawa and Mason 2005).

Specifically for this investigation, we used the cold plate to control the temperature of some starting salts during ESD so that is was lower than 30°C to avoid sample melting (melting point (MP) in Table 1, based on Lide 2001). The cold plate in the PEACh is electrically grounded, as well as the PEACh itself. On the other hand, the lower electrode must be isolated electrically from the cold plate; this was satisfied by using a Teflon holder between the lower electrode and the cold plate. The holder is thin enough (1.59 mm) to allow the temperature (T) of the lower electrode to be thermally controlled by the cold plate. A thermocouple was inserted into a tunnel of 0.79 mm diameter in this Teflon holder to measure the T of the lower electrode while keeping its electric isolation from the cold plate.

During an ESD process in the PEACh, the equilibrated temperature T_{eq} of the lower-electrode sample cell was normally reached after > 30 minutes. For most hydrous S and Cl salts with melting-point temperatures above 130°C, we do not use LN_2 cooling. The resulting T_{eq} is in the range of 80-105°C (Figure 2). For a few selected salts (e.g., $FeSO_4 \cdot 7H_2O$ and some hydrous chlorides, Table 1), the ESD experiments were run using LN_2 to cool the cold plate and generate a T_{eq} in the range of 10-30°C, with the exact T_{eq} value depending on the type of salt (Figure 2). Those experiment products are marked as LT (low temperature) –ESD in figures.

3.3 Analysis methods of ESD reaction products

Almost all sulfates and chlorides show a color change after an ESD process of certain time duration (e.g., ≥ 7 hours, Table 1) under Mars conditions. For example, the photos in Figure 3 (a, b) are $MgCl_2 \cdot 6H_2O$ before and after 7h ESD, shown with different magnifications (Figure 3b, c, d). The color change only appears at the surface of ESD products, that is consistent with our previous finding of surface enrichment of ESD-generated species ($NaClO_3$ and $NaClO_4$, when using NaCl as the starting phase) based on Ion Chromatography (IC) analyses of the layers in the ESD-product (Figure 6b of Wu et al., 2018). Both color change and IC data suggest that the electrochemical reaction induced by ESD in a Mars chamber is an atmosphere-to-surface interaction, which also means the *as is* surface of an ESD product should be the best sampling site for the characterization of new species generated by ESD.

We used laser Raman spectroscopy (Raman), X-ray diffraction (XRD), Vis-Near-IR spectroscopy (VNIR), Mössbauer spectroscopy (MB), and Ion Chromatography (IC) to characterize the ESD products in this study. Among them, Raman and VNIR measurements were made on the *as is* surface. In particular, all micro-beam Raman analyses were made directly on the spots that show color changes, which were selected under the microscope of our Raman system. On the other hand, the field of view (FOV) of the VNIR probe matches well with the size of the SiO_2 cell that contains the ESD product, so a VNIR spectrum was taken from the whole *as is* surface of the ESD product. For XRD and Mössbauer analyses, the bulk powder sample from the full depth of the SiO_2 cell of an ESD product was re-ground and used. Bulk powder samples were also used for IC analyses. All these analyses were taken at room temperature.

<u>Raman spectra</u> of all samples were collected using a Renishaw inVia Raman system, with 532 nm excitation wavelength, spectral range of 50-4300 cm^{-1} and spectral resolution better than 1 cm^{-1}. A 50× long-working-distance objective was used that generates an ~ 1 µm beam diameter at laser focus. Raman analysis of each ESD product was always taken on multiple spots in several areas at the *as is* surface of a sample, with a total of > 30 (at least) spectra per sample. A laser beam energy of 5 mW was normally used for the measurements of ESD products from Mg, Ca, and Na salts. A much lower laser energy (0.5-0.05 mW) was used on the ESD products from Fe-bearing salts. The Raman spectrometer is calibrated during each working day to keep the accuracy and precision of Raman peak positions within ± 0.5 cm^{-1}.

<u>The VNIR spectra</u> of the ESD products were acquired using Analytical Spectral Devices (ASD) FieldSpec4 spectroradiometer (Malvern Panalytical Company) with a contact probe. The obtained spectrum covers a wavelength range of 0.35 to 2.5 µm, with spectral resolution of 3 nm @ 700 nm and 10 nm @ 1400/2100 nm. A Spectralon target was used for absolute reflectance calibration before the sample measurements. The recording time of each spectrum was 1 second, and at least two spectra were taken from each sample for redundancy.

<u>XRD measurements of ESD products</u> were made using a Bruker D8 Advance diffractometer, with CuKα radiation (λ = 1.54052 Å) at 40 kV and 40 mA and a collecting angle of 3°. Each sample was ground

again to fine powder, and was put into a MTI zero background silicon holder. The XRD measurement routine was 0.02° step size, 1 second dwell time, and 15 rotation per minute, and 4° to 60° 2θ range. The Bruker XRD has a guaranteed calibration that is confirmed during installation and monitored by analysis of a NIST SRM 1976a Al_2O_3 standard. The alignment is also guaranteed and has been demonstrated to be within 0.03° 2θ of the absolute peak position of the NIST SRM.

Mössbauer spectral measurements were made on the ESD products from a few Fe-bearing phases. A plastic washer with an inner diameter of 1.2 cm was used to hold a mixture of sample plus sugar with Kapton® polyimide tape on either side. A source of ~80 mCi ^{57}Co in Rh on a SEE Co. (formerly WEB Research Co.) model WT302 spectrometer at Mount Holyoke College was used. Following standard practice, Compton scattering of 122 keV gammas caused by electrons inside the detector were measured with and without a 14.4-keV Al foil stop filter in the gamma beam. Absorption was corrected Compton scattering by dividing the uncorrected absorption by one minus the Compton fraction. This correction allows accurate determination of % absorption in the spectra without affecting the fits. The range of energy deposited in the detector by Compton events extends from 0 keV to 40 keV, and overlaps both the 14 keV and 2 keV energies deposited by the 14 keV gammas, thus requiring correction.

Mössbauer spectra were acquired in 1024 channels at 295K over 24 hours for each sample. Interpolation to a linear velocity scale was used to correct for non-linearity using the spectrum of a 31 mm Fe foil.. The WMOSS Auto-fold procedure fits a straight line to points at the published values of the Fe metal and the observed positions in channels (*x* values), then folds each spectrum around the channel value that minimizes the least squares sum difference between the first and second halves of each spectrum.

Ion chromatography was used to quantify the SO_4 production from ESD experiments using Na_2SO_3 and $NaHSO_3$ as starting salts. A 15-20 mg homogenized sample was dissolved in N_2-purged milliQ water for IC analysis. An A-Supp7-250 anion column (45◦C, 3mM Na_2CO_3 eluent, 0.8mL/min, with suppression) on a Metrohm 881 Compact IC pro was used with a conductivity detector. We prepared five standards, from pure Na_2SO_4 from Sigma-Aldrich ,at concentrations of 1.3 ppm, 10.6 ppm, 20.3 ppm, 51.4 ppm, and 100.6 ppm, and generated a calibration line with R^2 value of 0.9954. The detection limit for sulfate by IC analysis was 0.1 ppm. The concentration in solution (in ppm) is then converted to ppm in the solid (mg SO_4/kg sample). Due to the rapid oxidation of sulfite in solution to sulfate under ambient laboratory conditions, the sample solutions were analyzed immediately after preparation to minimize oxidation during sample handling. The stability of sulfite was tested by comparing the concentration in the freshly prepared solutions and the same solution after sitting in air for 1 hour. Slight oxidation occurs even in this short time; therefore, the error of these measurements is estimated as the standard deviation between these two replicate measurements and was found to be on average 0.6 ppm in solution. This equates to a conservative estimate of ~350 ppm error in the solid, although samples were prepared and analyzed within ~20 min.

4. Analysis results of the ESD products from S and Cl salts

4.1 ESD products from Mg, Fe^{2+}, Fe^{3+}, Ca, Na sulfates and sulfites

4.1.1. ESD products from $MgSO_4 \cdot xH_2O$ (x=1, 4, 7)

As listed in Table 1, 0.25h, 1h, 2h and 7h ESD experiments were carried out on $MgSO_4 \cdot xH_2O$ (x=1, 4, 7) powder. The ESD product from each experiment was analyzed using Raman on multiple spots of an *as is* surface and using XRD on the bulk sample (from the full depth of the SiO_2 cell).

Raman spectra in Figure 4a are from 36-spot analyses on the *as is* surface of a 0.25h-ESD product from epsomite $MgSO_4 \cdot 7H_2O$. Data from the shortest ESD duration (0.25 hour) were purposely presented to show the intermediate species generated during the ESD process. In a Raman spectrum of sulfate, the fundamental vibrational modes (ν_1, ν_2, ν_3, and ν_4) of the $(SO_4)^{2-}$ unit are located in four spectral regions centered around ~ 1000, 500, 1150, and 600 cm^{-1}, often with multiple peaks for each mode. Among the ν_1 Raman peaks near 1000 cm^{-1} in Figure 4a, the strongest sharp peak at 1000 cm^{-1} belongs to a crystalline starkeyite $MgSO_4 \cdot 4H_2O$ (4W), a weak sharp peak at 983 cm^{-1} belongs to a crystalline $MgSO_4 \cdot 6\text{-}7H_2O$ phase (6-7 W) (983.6 cm^{-1} for $MgSO_4 \cdot 6H_2O$ and 984.1 cm^{-1} for $MgSO_4 \cdot 7H_2O$, Table 3 of Wang et al., 2006), the broad peaks (from all sampling spots) centered ~1030 cm^{-1}, ~600 cm^{-1} and ~500 cm^{-1} (marked as "Amor") demonstrate the initiation of amorphization (based on Figure 20 of Wang et al., 2009). Figure 4b shows an overlay of the Raman spectra from a 37-spot analysis of the same 0.25h-ESD product in 3876 - 3072 cm^{-1} spectral range. The occurrence of H_2O peaks from each sampling spots indicates retention of structural H_2O in ESD product, i.e., $MgSO_4 \cdot 7H_2O$ is partially dehydrated.

Raman spectra in Figure 4 reveal a fast dehydration from epsomite $MgSO_4 \cdot 7H_2O$ to crystalline starkeyite (4W) at least, and the initiation of amorphization. Experimental study of hydrous Mg-sulfates (Wang et al., 2009) revealed that amorphous $MgSO_4 \cdot xH_2O$ can hold up to three structural H_2O per $MgSO_4$ molecule, consistent with the observation of H_2O Raman peaks of different shapes from all sampled spots on the *as is* surface (Fig. 4b).

Amorphization in epsomite $MgSO_4 \cdot 7H_2O$ developed very fast with increased ESD time duration. After 1 hour of ESD processing in the PEACh, almost no crystalline Mg-sulfates can be detected in the fundamental vibrational spectra range (not shown, but similar to Figure 5a). On the other hand, a trace of the H_2O peak still remains (not shown) after 7h ESD process on epsomite. In other words, full amorphization was reached but the full dehydration was not reached at the *as is* surface.

Total amorphization at the *as is* surface was reached after 1.5 h of ESD process on crystalline starkeyite $MgSO_4 \cdot 4H_2O$. As seen in Figure 5a, amorphization is characterized by (1) shift of the ν_1 peak from 1000 cm^{-1} to ~ 1030 cm^{-1}, (2) broadened peak width for every peak in the whole spectrum and in every spectrum from all sampled spots, (3) merged peaks of ν_2, ν_4, and the lattice modes (below 400 cm^{-1}) into three large spectral envelopes, and (4) severely reduced S/N ratio (because the Raman peak intensity of non-crystalline phase is 1-2 order of magnitude weaker than that of crystalline phase with similar composition, White 1975) which also appeared as a raised spectral background. In Figure 5b, the structural damage of a crystalline kieserite $MgSO_4 \cdot H_2O$ by a 1.5h ESD are presented by (1) broadened peak widths, (2) loss of minor peaks, and (3) reduction of S/N, but to a lesser degree when compared with Figure 5a from crystalline starkeyite of 1.5h ESD.

<u>*XRD measurements*</u> made on the bulk ESD products from $MgSO_4 \cdot xH_2O$ (x=1, 4, 7) are shown in Figure 6. Both XRD patterns on the top of Figure 6 have a raised "hump" from 10° to 40°(2θ), which can be fitted with three wide "bands", centered at 14.2°, 21.9°, and 28.0° with widths of 5.4°, 11.4°, and 11.5°, respectively. A few sharp XRD lines remain on the top of the "hump"; some can be assigned as crystalline $MgSO_4 \cdot H_2O$ (1w) or $MgSO_4 \cdot 4H_2O$ (4w), with some lines unassigned since hydrous Mg-sulfates can have eight different hydration degrees. The difference in the degrees of amorphization seen in XRD patterns (Fig. 6) and Raman spectra (Fig. 5a) is caused by the sampling differences of the two analyses, with XRD sampled the bulk sample (from full depth of SiO_2 cell) and Raman sampled the *as is* surface only.

The third XRD pattern in Figure 6 is obtained from the 1.5h-ESD product from kieserite $MgSO_4.H_2O$ (8.5h-ESD product has the same pattern). When compared with the standard XRD pattern of kieserite, the 1.5h-ESD product has a broadened line width for every line in the whole XRD pattern. In addition, the multiple lines in the line groups at 25-30°, 35-40°, ~44°, and 55-60° 2θ ranges are merged into envelopes with non-symmetric shape. XRD standard 00-001-0638 (kieserite, $MgSO_4 \cdot H_2O$, monoclinic) and 00-037-009 (caminite $Mg_2(SO_4)_2 \cdot 2H_2O$, tetragonal) in the PDF database have lines that may contribute the merged line groups of the ESD product (Fig. 6). The observed XRD line widening and merging of line clusters suggest a heavily distorted crystal structure in the ESD product from kieserite, suggesting development of amorphization caused by the impact of energetic electrons and by the reaction with free radicals generated in the ESD process. This conclusion is consistent with Raman observations from Figure 5b.

Overall, the effects of ESD processes on hydrous Mg sulfates are dehydration and amorphization. The higher the hydration degree in an original salt, the higher the rate of amorphization by the ESD process, a phenomenon that we also observed for other salts in this study.

4.1.2. ESD products from FeSO4.xH2O (x=1, 4, 7)

The melting point of melanterite $FeSO_4{\cdot}7H_2O$ is 60°C (Lide 2001, Table 1). So the ESD experiment of melanterite was made with LN_2 temperature control, T_{eq} < 30°C (Figure 2), and durations of 0.25h, 1h, 3h, and 7h. ESD products were analyzed by Raman and VNIR on the *as is* surface, and by XRD and Mössbauer on bulk samples. Very low laser power (0.5 mW) was used in Raman measurements to avoid overheating of these Fe-bearing phases by the laser beam, which was confirmed by visual inspection under the Raman microscope before and after each scan.

Raman spectra Figure 7 (a, b) shows the overlay of the first 60 Raman spectra from the 0.25h ESD and 7h ESD products. The obtained spectra from the 0.25h ESD product are compared in Figure 7a with the standard Raman spectra of $FeSO_4{\cdot}xH_2O$ (x=1, 4, 7, Choi et al., 2007). The ν_1 mode of rozenite $FeSO_4.4H_2O$ (4w) and szomolnokite $FeSO_4{\cdot}H_2O$ (1w), 1018 cm^{-1} and 990 cm^{-1}, appeared after a 0.25 hour ESD process, while the Raman peaks of melanterite $FeSO_4{\cdot}7H_2O$ (7w) disappeared i.e., a total destruction of melanterite by 0.25h-ESD. The only unassigned Raman peak in Figure 7a is at 1035 cm^{-1} (marked by red arrow), which is an indication of early development of amorphization (Fig. 7 of Ling and Wang, 2010), similar to the case of $MgSO_4{\cdot}7H_2O$ after 0.25h-ESD (Fig. 4a). The peak position at 1035 cm^{-1} suggests an amorphous phase $Fe^{3+}{}_2(SO4)_3{\cdot}5H_2O$ (based on Fig. 18 of Wang and Ling 2011). Because of the different T_{eq} achieved by ESD processes on epsomite and melanterite (Fig. 2), a direct comparison of the amorphization rate cannot be extracted for these Mg, Fe-sulfates.

Figure 7b shows the first 60 spectra from a 120-spots Raman scan on the *as is* surface of 7h ESD product from melanterite, which revealed the abundant amorphization in the product. The center of strongest peak moves to near 1075 cm^{-1} (Fig. 7b), shown as a large envelop that merged the multiple peaks of ν_1 and ν_3 modes of SO_4 unit together (the merge of ν_1 and ν_3 was less obvious in Mg-sulfates, Fig. 5, 6). Peaks of the ν_2, ν_4, and lattice modes are also merged into three large envelopes around 610, 470, and 240 cm^{-1}, respectively, with severely reduced S/N ratio. The ν_1 peak of crystalline szomolnokite $FeSO_4{\cdot}H_2O$ (1w) at 1018 cm^{-1} remains in some spectra.

Raman spectra obtained from a scan on the 1.5h-ESD product from rozenite $FeSO_4{\cdot}4H_2O$ are shown in Figure 8a. The strong and wide envelope spanning 1300 to 950 cm^{-1} represents a merge of ν_1 and ν_3 modes of SO_4 unit, with the sharp ν_1 peak of $FeSO_4{\cdot}H_2O$ remaining in some spectra. The other three wide envelopes (below 1000 cm^{-1}) are from the merged peaks of ν_2, ν_4, and lattice modes respectively, similar to 7h ESD products from melanterite (Fig. 7b). H_2O peaks centered at 3430 cm^{-1} were detected at almost all sampled spots on the *as is* surface (Fig. 8a), suggesting that full dehydration was not reached.

Very sharp Raman peaks remained in all spectra from the ESD products of szomolnokite $FeSO_4{\cdot}H_2O$ (1w), even after 15.5h-ESD (Fig. 8b). When compared with the standard spectra of various ferrous and ferric sulfates, we found that the best match was with $Fe^{3+}OHSO_4$. The transformation from $Fe^{2+}SO_4{\cdot}H_2O$ to $Fe^{3+}OHSO_4$ demonstrated the occurrence of oxidation ($Fe^{2+} \rightarrow Fe^{3+}$) and hydrolysis caused by the ESD process. The major peak at 1094 cm^{-1} of $Fe^{3+}OHSO_4$ was also observed at some sampled spots (hidden in the spectral overlay of Fig. 8a) on the *as is* surface of 1.5h-ESD product from rozenite $FeSO_4 \cdot 4H_2O$.

<u>*XRD measurements*</u> were made on the bulk samples of ESD products from $FeSO_4 \cdot xH_2O$ (x = 1, 4, 7). Figure 9 shows the XRD pattern from the 7h ESD product from melanterite $FeSO_4 \cdot 7H_2O$ and from szomolnokite $FeSO_4 \cdot H_2O$. The top XRD pattern in Figure 9 overlays the characteristic XRD lines of $FeSO_4.H_2O$ onto two large XRD "humps", centered at 11.4° and 27.5° that are similar to the humps in Figure 6, but slightly narrower in widths, 5.4° and 9.0°. This XRD pattern reveals a partially amorphous bulk sample. The XRD pattern from the 1.5h-ESD product from $FeSO_4 \cdot 4H_2O$ (not shown) has strong lines of crystalline rozenite and szomolnokite. The partial amorphization observed in Raman data (Fig. 8a) appears less obvious in XRD data, likely because a bulk sample from full depth of ESD product in the SiO_2 cell was used for XRD. The XRD pattern (2^{nd} in Fig. 9) from the 1.5h-ESD product from $FeSO_4 \cdot H_2O$ has the major lines of butlerite $Fe^{3+}OHSO_4 \cdot 2H_2O$ and $Fe^{3+}OHSO_4$, in addition to the remaining lines of $FeSO_4 \cdot H_2O$. The appearance of butlerite and dehydrated butlerite indicate the oxidation of Fe^{2+} to Fe^{3+}, and hydrolysis caused by ESD processes, consistent with Raman observations (Fig. 8b).

<u>*VNIR spectra*</u> (Fig. 10) were taken at the *as is* surfaces of 0.25h, 1h, 3h, and 7h ESD products from $FeSO_4 \cdot 7H_2O$ ($T_{eq} < 30$°C, Fig. 2). The first major spectral change with increasing ESD time is a decrease in absorption band depth near 1.0, 1.4, and 1.9 µm, suggesting gradual dehydration. Indeed, the narrow and strong VNIR doublet near 1.9 µm of the 0.25h-ESD product can be assigned to $FeSO_4 \cdot 4H_2O$ (Fig. 3 of Wang et al., 2016), and the much wider and weaker doublets (near 1.9 µm) in the spectra of the 1h, 3h, 7h ESD products are similar to the doublet of $FeSO_4 \cdot H_2O$ (Fig. 6 of Wang et al., 2016). The second major spectral change is a gradual decrease of spectral contrast, which is especially obvious in the spectrum of 7h ESD product. This phenomenon reflects the destruction from a crystalline structure, consistent with Raman and XRD observations. Notice a weak but characteristic VNIR spectral pattern of $FeSO_4 \cdot H_2O$ (Fig. 10) was obtained from the 7h ESD product, while on the same *as is* surface, a multi-spot Raman scan shows almost total amorphization; only a few spots retained the 1018 cm^{-1} peak of szomolnokite (Fig. 7b). This phenomenon shows that the sensitivities of Raman and VNIR spectra for detecting structural damage are different. A previous study using XRD, Raman, Mid-IR, and VNIR on a set of saponite samples with different degrees of amorphization revealed that VNIR spectroscopy is less sensitive to the loss of crystallinity. From the saponite samples that show totally non-crystalline XRD patterns, sharp VNIR spectral peaks can still be seen at 1.4 µm, 1.9 µm and especially in the 2.2-2.4 µm spectral range (Fig. 1, 2 of Fu et al., 2017).

A <u>*Mössbauer spectrum*</u> was obtained from 59 mg of the powdered bulk 7h ESD product from $FeSO_4 \cdot 7H_2O$. The measured spectrum was fit in a variety of ways using two different programs. The Mex_disdd solves the full hyperfine interaction Hamiltonian and minimizes the difference between modeled line shape independent peaks and the experimental spectrum using center shift, quadrupole splitting, and linewidth as variable parameters. Disd_3e makes velocity approximations rather than solving the full interaction Hamiltonian and uses a range of line-shape-independent quadrupole splitting distributions (QSD) to build the peaks. Because the peaks in these spectra overlap heavily and it is difficult to prioritize one model over the other, so both are shown and reported (Figure 11a, b). In both models, there are two Fe^{3+} and three Fe^{2+} distributions. Parameters are given in Table 2; errors on total $\%Fe^{3+}$ are ±1-5 % absolute based on repeated fits to the same spectra, with a detection limit for Fe^{3+} of roughly 1%. Although it is known that differential recoil-free fraction (*f*) effects can affect the assumption that Mössbauer peak area directly represents the proportions of Fe in each site or valence state, *f* has not been determined for these materials. Thus, this paper assumes that recoil is the same for both Fe^{2+} and Fe^{3+}. Based on Mössbauer analysis, we obtained a Fe^{3+}/Fe_{total} ratio of 44% in analyzed sample. This result indicates a strong oxidation has occurred during ESD process on melanterite $FeSO_4 \cdot 7H_2O$. This conclusion is visually confirmed by the color change of the samples, from light green of

$FeSO_4 \cdot 7H_2O$, to light yellow, to light brown, and finally to dark brown after 7h ESD, suggesting more oxidized iron (Fig. S1). The amorphization development in 7h ESD product from $FeSO_4 \cdot 7H_2O$ may be reflected in the details of Mössbauer parameters, e.g., CS = 1.21-1.29 mm/s and QS = 1.55-2.66 mm/s, which are different from the ranges in literature for $FeSO_4 \cdot xH2O$ (x=1, 4,7), 1.16-1.31 mm/s for CS and 3.17-3.24 mm/s for QS (Cheetham et al., 1981; Dyar et al., 2013; Eissa et al., 1994a,b; Grant et al., 1966; Montano; 1981; Sakai et al., 1981; Sallam et al., 1994).

Overall, the effects of ESD processes on hydrous Fe^{2+} sulfates are dehydration, amorphization, and oxidation from Fe^{2+} to Fe^{3+}.

4.1.3. ESD products from ferric sulfates

Given the importance of Fe^{3+}-bearing phases for Mars surface mineralogy, we conducted ESD experiments in the PEACh on four Fe^{3+}-bearing species, Na-jarosite $NaFe_3(OH)_6(SO_4)_2$, ferricopiapite $Fe_{4.67}(SO_4)_6(OH)_2 \cdot 20H_2O$, akaganeite FeO(OH,Cl), and pyrite FeS_2 (Table 1).

4.1.3.1. ESD products from ferricopiapite

Figure 12b shows typical Raman spectra obtained from ESD products of ferricopiapite $Fe_{4.67}(SO_4)_6(OH)_2 \cdot 20H_2O$, with the ESD durations of 0.25h, 1h, 2h, 3h, and 7h. When compared with Raman spectra of standard ferric sulfates (Fig. 12a, from Ling and Wang, 2010), we found the spectra from the 0.25h-ESD product can be assigned to ferricopiapite (#1 in Fig. 12b), rhomboclase $FeH(SO_4)_2 \cdot 4H_2O$ (#2 in Fig. 12b), and a phase whose most peaks are similar to those of ferricopiapite in positions and shapes, except its strongest ν_1 peak at 1018 cm^{-1} (#3 in Fig. 12b) that can be regarded as a merged ferricopiapte doublet, with an upper-shifted peak center. Forming acidic rhomboclase from basic ferricopiapite is also a dehydration process with N_{H2O}/N_{SO4}=3.67 → 2. The shifting of ν_1 peak position to higher wavenumber is normally an indication of dehydration, observed in the Raman spectra of hydrous Mg, Fe^{2+}, and Ca sulfates. The merge of the doublet suggests a damaged crystal structure, i.e., an early step towards the amorphization.

Typical Raman spectra from #4 to #8 in Figure 12b obtained from 1h, 2h, and 7h ESD products all have the strong and wide peak in ν_1 spectral range, but the central position of this peak gradually shifted towards higher wavenumber (indicated by a dotted arrow line in Fig. 12b), from 1018 cm^{-1} to 1057cm^{-1} (#3 to #8 in Fig. 12b). This peak shift is accompanied by the loss of details for all peaks below 800 cm^{-1}, which eventually become three wide envelopes centered around ~650 cm^{-1}, ~480 cm^{-1}, and ~250 cm^{-1} (spectrum #4, #5, #6, #7, #8). These are typical Raman spectral pattern of amorphous ferric sulfates (#3 in Fig. 12a). Wang and Ling (2011) built a calibration curve (their Fig. 18) to quantify the number of structural H_2O per $Fe_2(SO_4)_3$ unit, from eleven to five, using the ν_1 peak position of amorphous ferric sulfates (from 1022 to 1035 cm^{-1}). Although there are no other experimental studies of amorphous ferric sulfates with structural water less than five, an educated guess is that the continuous ν_1 peak upper shift from 1035 cm^{-1} to 1057 cm^{-1} (Fig. 12b) is due to continuous dehydration from five to zero structural waters per $Fe_2(SO_4)_3$ unit, based on the assignment of spectra #9 and #10 in Figure 12b.

Spectra #9 and #10 (Figure 12b) were obtained from many Raman sampled spots on the *as is* surface of the 7h ESD product from ferricopiapite. Spectrum #10 is a perfect match with the standard Raman spectrum of crystalline anhydrous $Fe_2(SO_4)_3$ (#4 in Fig. 12a), and spectrum #9 is a mixture of standard spectra of two polymorphs, the anhydrous $Fe_2(SO_4)_3$ and mikasaite $Fe_2(SO_4)_3$ (#5 in Fig. 12a), both are crystalline materials (Ling and Wang 2010). The multi-spots Raman scans revealed that crystalline anhydrous $Fe_2(SO_4)_3$ appeared early in ESD products (e.g., 1h-ESD) and became abundant in the ESD product with longer time duration (e.g., 7h ESD).

Overall, the major effect of ESD process on ferricopiapite is dehydration, from N_{H2O}/N_{SO4}=3.67 to N_{H2O}/N_{SO4}=0. The ESD caused structural change is complicated, from crystalline to full amorphization, then back to crystalline again. During the early dehydration, the ferric sulfate also changed from basic ferricopiapite to acidic rhomboclase.

4.1.3.2. ESD products from Na-jarosite, akaganeite, and pyrite

It is quite surprising that no obvious mineral transformation occurred in Na-jarosite after long duration ESD processes (even after 64 hours). The color of post-ESD sample surface shows an obvious darkening (Fig. S2). The peaks of hematite appeared in the spectra from some spots in multi-spots Raman scans. However, 99% of Raman spectra obtained from the *as is* surfaces of eight ESD products from Na-jarosite maintain an almost perfect match with the Raman spectrum of the original Na-jarosite (Fig. S3). The Mössbauer spectrum of this post-64h ESD product revealed a set of typical CS and QS for Na-jarosite (Fig. S4).

Considering the importance of jarosite in martian surface mineralogy, we made two sets of 1:1 mixtures of Na-jarosite with $MgSO_4 \cdot 7H_2O$ and $MgCl_2 \cdot 6H_2O$, and did ESD on them, with a goal to study a potential catalysis effect. Again, no obvious mineral phase transformation was observed by Raman spectroscopy in the products from two additional sets of eight ESD experiments (Table 1, 2), except the spectrum of hematite was seen from some spots in the Raman scans on these ESD products. The Mössbauer spectra of the 7h ESD products from the two mixtures (not shown) support ~ 100% jarosite among the Fe-phases in bulk samples.

Similar to Na-jarosite, no obvious mineral transformation from akaganeite $Fe^{3+}O(OH,Cl)$ was found by Raman and Mössbauer analysis of the post-ESD products (Fig. S5). On the other hand, Raman scans on post-ESD products from a natural pyrite show minor changes in Raman peak positions and shapes (Fig. S6). However, the XRD pattern of the 14h ESD product from this natural pyrite does show an obvious change from standard pyrite, thus it cannot be compared with Raman spectra to suggest any significant phase transformation.

4.1.4. ESD products from Na_2SO_4

The Raman spectra obtained on the *as is* surface of the 7h ESD product from Na_2SO_4 powder have only minor changes from the standard spectrum (Fig. 13), such as the slight peak broadening of Raman ν_1 mode near 992 cm^{-1} (insert of Fig. 13), and slightly raised spectral background after 400 cm^{-1}. The broadening of the Raman peak indicates a damaged crystalline structure from original Na_2SO_4. XRD measurements were not made on this sample.

4.1.5. ESD products from $CaSO_4.2H_2O$

The Raman spectra (Fig. 14) obtained on the 7h ESD product of $CaSO_4 \cdot 2H_2O$ powder revealed the transformation from gypsum to γ-$CaSO_4$ phase (not anhydrite α-$CaSO_4$) mainly, that has a sharp peak at 1026 cm^{-1} shown in the insert of Figure 14. Ordinary γ-$CaSO_4$ would not be stable at ambient terrestrial laboratory conditions. The post-ESD product from $CaSO_4 \cdot 2H_2O$ was sealed in a glass vial, with the Raman measurements made through the glass wall. In addition to γ-$CaSO_4$, bassanite $CaSO_4 \cdot 0.5H_2O$ was identified in some sampled spots (peak at 1014 cm^{-1} in the inset of Fig. 14), that is also supported by the observations of structural H_2O peaks in Raman spectra (not shown) of some sampled spots. No XRD measurement was made on this sample. It is notable that a large amount of γ-$CaSO_4$ was found to be stable within the vein system of martian meteorite MIL03346 (Ling and Wang, 2015), as well as in soils of hyperarid regions on Earth, such as from the Atacama Desert (Wei et al., 2015) and the saline playa on the Tibet Plateau (Wang et al., 2018). The γ-$CaSO_4$ phase apparently can exist stably under ambient terrestrial laboratory conditions. We are currently investigating the structural and chemical reasons for the abnormal stability of the γ-$CaSO_4$.

4.1.6. ESD products from Na_2SO_3 and $NaHSO_3$

In order to evaluate the oxidation power of ESD processes on S-bearing species, we selected two sulfites, $Na_2S^{4+}O_3$ and $NaHS^{4+}O_3$, as the starting phases for a set of ESD experiments with 0.25h to 11h duration (Table 1).

Among the obtained Raman spectra from 252 spots-scan on the *as is* surface of 7h ESD product from Na_2SO_3, about ~ 12% has an additional peaks at 997 cm^{-1} (insert of Fig. 15). On the other hand, all Raman spectra from a total of 188 spots-scan on the *as is* surface of the 7h ESD product from $NaHSO_3$ has the additional peak at 997 cm^{-1} (not shown). Besides, this peak position does not match with the ν_1 peak of Na_2SO_4 at 993 cm^{-1} (insert of Fig. 15). XRD measurements were made on both sulfites. The XRD pattern of the 7h ESD product of $NaHSO_3$ is different from that of original sample (#1 in Fig. 16). After the 7h ESD process, new XRD lines appeared, and multiple lines merged in four regions (22-30°, 31-37°, 46-50°, and 57– 61° 2θ), suggesting structural damage of $NaHSO_3$. In addition, XRD standards 00-037-1488 ($Na_2S^{4+}O_3$), 04-015-3684 ($Na_2S^{4+}{}_2O_5$), and 00-021-1371 ($Na_2S^{6+}{}_3O_{10}$) in PDF database (#2, #3, #4 in Fig. 16) have lines that might contribute the merged line groups that appear in the top XRD pattern of Figure 16. The potential contribution of $Na_2S^{6+}{}_3O_{10}$ (#4 in Fig. 16) to the merged line groups provides a hint for the oxidation of S^{4+} to S^{6+}.

Oxidation of sulfite ($S^{4+}O_3^{-2}$) to sulfate ($S^{6+}O_4^{-2}$) through the ESD process was finally established using the Ion Chromatography (IC) analyses of 1h, 3h, 7h ESD products from Na_2SO_3 (dissolved in N_2-purged milliQ water and immediately analyzed by IC), shown in Figure 17. The time series shows a gradual increase as a function of ESD experimental duration, from 1 hour to 7 hours.

4.2. Analyses of the ESD products from Mg, Fe, Ca, Al, Na, K- Chlorides

We conducted ESD experiments on six chlorides (Table 1), two anhydrous (NaCl and KCl) and four hydrous (Mg-, Fe^{2+}-, Ca-, Al-chlorides). This selection was made on the basis of their potential existence in anhydrous or hydrous forms on Mars and their stable existence at ambient laboratory conditions making them experimentally feasible. Three hydrous chlorides (Mg-, Fe^{2+}-, Al-) among them have melting points T_{mp} below 100°C (Table 1); thus we ran the ESD experiments on these chlorides with LN2 temperature control with equilibrated temperature T_{eq} < 30 °C (Fig. 2).

4.2.1. ESD products from $FeCl_2.4H_2O$

Figure 18 shows typical Raman spectra obtained from the *as is* surfaces of 0.25h, 1h, 3h, and 7h ESD products from $FeCl_2{\cdot}4H_2O$. Spectral features from most spots on 0.25h-ESD product remained similar to those of crystalline chlorides, with an additional sharp Raman peak at 334 cm^{-1} (#2 in Fig. 18) The major H_2O peak at 3406 cm^{-1} and a peak-shoulder at 3445 cm^{-1} (not shown) suggest a change of hydration degree from $FeCl_2{\cdot}4H_2O$ to probably $FeCl_2{\cdot}2H_2O$. After 1h ESD, Raman peaks began to broaden (#3 in Fig. 18). In addition, an overall Raman spectral shape very similar to that of hematite $Fe^{3+}{}_2O_3$ occurs frequently after 3h ESD (#4 in Fig. 18). After 7h ESD, a few sampled spots have a peak near 395 cm^{-1} (#5 in Fig. 18) that is the major Raman peak of goethite, $Fe^{3+}OOH$, but most spots have extremely broad Raman "humps" near 1310, 710, and 300 cm^{-1} (#6 in Fig. 18). The H_2O peak in the 3300-3700 cm^{-1} range becomes wide and weak, to almost nonexistent (not shown). Overall, this set of spectra revealed a progressive loss of crystallinity, oxidation ($Fe^{2+} \rightarrow Fe^{3+}$), and dehydration.

The XRD pattern obtained from this 7h ESD product from $FeCl_2{\cdot}4H_2O$ (Fig. 19) has three "humps" in 2θ ranges of 8-18°, 23-41°, and 45-60°, with broadened lines on top of the humps. These XRD lines match with $FeCl_2{\cdot}2H_2O$ (pdf: 00-025-1040), $FeCl_2$ (pdf: 00-001-1106), and $Fe^{3+}OCl$ (pdf: 00-039-0612) (#1, #2, #3 in Fig. 19), but have much wider linewidth and merged line groups. Therefore, XRD data supports the inferences of amorphization, oxidation, and dehydration that are based on Raman analysis.

The Mössbauer spectrum of bulk 7h ESD product from $FeCl_2 \cdot 4H_2O$ (Fig. 20) was modeled using the Mex_disdd program. These data are interpreted within the context of broader work on Mössbauer spectroscopy of minerals with similar structures. Only a handful of Mössbauer spectra could be found in the literature for iron dichloride tetrahydrate, and most of the papers do not provide explicit parameters (Ohshita et al., 2002) or focus on low-temperature (Shinohara, 1977) or magnetic field measurements (Johnson, 1966; Kandel et al., 1973; Spiering et al., 1978) that are not comparable to this study. Overall, the analyzed sample contains 88% of the total Fe as Fe^{3+}, which was 0% in the starting phase of $FeCl_2 \cdot 4H_2O$. The strong oxidation revealed by this Mössbauer result is consistent with Raman observation of hematite occurrence in 3h and 7h ESD products.

The Mössbauer result suggests that both Fe^{2+} and Fe^{3+} are present in two dissimilar sites. Most of the Fe is Fe^{3+} in sites with CS = 0.37-0.38 mm/s and Qs = 0.55 and 0.93 mm/s. A small amount of Fe^{2+} is also observed, with CS = 1.22 and 1.26 mm/s and Qs = 2.96 and 2.10 mm/s, respectively. Ôno et al. (1964) report parameters of CS = 1.26 mm/s and QS = 0.80 mm/s for $FeCl_2$; these seem unusual for this phase. Chandra and Hoy (1966) studied $FeCl_2 \cdot 2H_2O$ and gave parameters of CS = 1.03 mm/s and QS = 2.50 mm/s. Grant et al. (1966) gave parameters of CS = 1.22 mm/s and QS = 2.98 mm/s for $FeCl_2 \cdot 4H_2O$ – very similar to the parameters obtained in this study, though our modern analyses reveal two different doublets.

VNIR spectra (Fig. 21) were measured from the *as is* surfaces of 0.25h, 1h, 3h, and 7h ESD products from $FeCl_2 \cdot 4H_2O$ (T_{eq} < 30°C, Fig. 2). As with the ESD products from $FeSO_4 \cdot 7H_2O$ (Fig. 10), there are two major trends of spectral changes following the increase of ESD duration. Absorption band depth near 1.0, 1.4, and 1.9 µm decreases, suggesting a gradual dehydration, and overall spectral contrast decreases, consistent with the destruction of a crystalline structure observed by Raman and XRD analysis. Furthermore, there is a reduction of spectral slope between 400 to 800 nm that is more obvious in Figure 21 than in Figure 10. This more obvious slope change could be a reflection of Fe^{3+}/Fe_{total} = 88% in 7h ESD from $FeCl_2 \cdot 4H_2O$, which is higher than Fe^{3+}/Fe_{total} = 44% in 7h ESD product from $FeSO_4 \cdot 7H_2O$, determined by Mössbauer analyses.

4.2.2. ESD products from Na, K, Mg, Al, Fe^{2+}-chlorides

The structural damage (i.e., development towards amorphization) of common chlorides by energetic electrons of the ESD process is strongly influenced by chemical bonding. XRD is the major tool to characterize these ESD products.

After running ESD experiments with the same time duration (Table 1), the product from a starting material of $FeCl_2 \cdot 4H_2O$ shows an obvious change in XRD pattern (Fig. 19), whereas the products from either NaCl or KCl as starting material (Fig. 22) still have perfect matches with the standard crystalline forms of NaCl (pdf: 00-005-0628) and KCl (pdf: 00-004-0587).

Similarly, the XRD pattern of the LT-7h ESD product from $AlCl_3.6H_2O$ indicates a total amorphization (1st black curve in Fig. 23). On the other hand, the XRD pattern of the LT-7h ESD product from $MgCl_2 \cdot 6H_2O$ (2nd black curve in Fig. 23) has an uneven raised background, with lines that match with a mixture of $MgCl_2 \cdot H_2O$ (pdf: 00-061-0222), $MgCl_2 \cdot 2H_2O$ (pdf: 00-003-0765), and $MgCl_2 \cdot 4H_2O$ (pdf: 04-017-8711), suggesting dehydration from $MgCl_2 \cdot 6H_2O$. The raised background, the line broadening, and line merging indicate development of amorphization. Furthermore after a long duration (21 hours) ESD on $MgCl_2 \cdot 6H_2O$, the XRD lines of $Mg(ClO_4)_2 \cdot 6H_2O$ (pdf: 00-014-0022) appear (not shown), indicating oxidation from Cl^{1-} to Cl^{7+} as observed in NaCl by our previous study (Wu et al., 2018).

In contrast, the XRD pattern of the LT-7h ESD product from $CaCl_2 \cdot 2H_2O$ (3rd black curve in Fig. 23) almost perfectly matches standard $CaCl_2 \cdot 2H_2O$ (pdf: 04-010-1481). During the XRD measurement (total of 15 minutes) on the 14h ESD product from $CaCl_2 \cdot 2H_2O$, an obvious color change of the sample (from white to semi-transparent) was observed (laboratory relative humidity > 55%) and an XRD pattern similar to standard $CaCl_2·2H_2O$ was obtained. Based on these two XRD measurements, we estimate that the ESD process may have caused dehydration of $CaCl_2·2H_2O$, while a positive identification of the ending phase is lacking at current stage.

Overall, these XRD data on 7h ESD products from Mg, Fe, Al, Ca, Na, K chlorides suggest an approximate grouping that reflects how easily the ESD process causes structural damage of these chlorides, with Al, Fe, and Mg chlorides more easily damaged than Ca, Na, and K chlorides. This grouping is consistent with the observed ease of Cl release induced by the ESD process from common chlorides as reported in Wang et al. (2020).

5. Discussion

Table 3 summarizes the major conclusions on phase identifications of the ESD products from each salt. The column of "mid-phase" after a short period of ESD (⩽ 1.5 hour) shows the pathways of these ESD-induced phase transformations. The listed final phases were reached mostly after 7 hours of the ESD process, with a few exceptions. Table 3 shows that phase transformations have occurred to different degrees in most of the 22 minerals and their mixtures tested in this study (a total of 75 ESD experiments, Table 1), as induced by a medium-strength ESD process with limited time duration (normally 7 hours). There are three major trends in the phase transformations: dehydration, amorphization, and oxidation of Fe, S, and Cl, which will be discussed separately.

5.1. Dehydration

Dehydration of hydrous salts was determined on the basis of direct Raman and XRD identification in ESD products of phases with hydration degrees lower than the starting salts. For example, $MgSO_4·xH_2O$ (x=1, 4), $FeSO_4·xH_2O$ (x=1, 4), $FeOHSO_4$, $Fe_2(SO_4)_3$, and γ-$CaSO_4$ were found in the ESD products of $MgSO_4·7H_2O$, $FeSO_4·7H_2O$, $Fe_{4.67}(SO_4)_6(OH)_2·20H_2O$, and $CaSO_4·2H_2O$ (Fig. 4, 6, 7, 8, 9, 12, 14). $FeCl_2·2H_2O$, $FeCl_2$, and $MgCl_2·xH_2O$ (x=1, 2, 4) were found in the ESD products of $FeCl_2·4H_2O$ and $MgCl_2·6H_2O$ (Fig. 19, 23).

In addition, there are three specific ESD-induced dehydrations. The first is that the highly hydrated sulfates ($MgSO_4·7H_2O$, $FeSO_4·7H_2O$) have a higher dehydration rate than those with lower hydration degrees of the same type (i.e., $MgSO_4·xH_2O$, $FeSO_4·xH_2O$, x=1, 4). This was reflected by the shift of central positions of the ν_1 Raman peak in the products as a function of ESD duration. The second is the occurrence of hydrolysis induced by ESD, i.e., from $FeSO_4·H_2O$ to $Fe(OH)SO_4$. The third is the difficulty in the dehydration of the salts (and minerals) without structural H_2O but only OH, such as jarosite $NaFe_3(OH)_6(SO_4)_2$ and akaganeite FeO(OH, Cl), as well as the 1:1 mixtures of Na-jarosite with each of two hydrous salts ($MgSO_4·7H_2O$ and $MgCl_2·6H_2O$). The spectrum of hematite was seen from some spots in the Raman scans on these ESD products, but it did not affect the conclusion from Mössbauer spectra, i.e. ~ 100% jarosite among the Fe-phases in bulk samples. This result means that transformation to hematite from jarosite by medium-strength ESD must be at a very low rate compared with those of other Mg, Fe^{2+}, Fe^{3+}, Ca, and Na sulfates.

It is worth to mention that we did not put a control in PEACh (i.e., a starting salt of same type but to protect it from being affected by ESD generated plasma and free radicals) during each of 75 sets of experiments, mainly due to the experimental difficulties. Considering the vacuum desiccation experiments on hydrous salts (Sklute et al., 2015; Vaniman et al., 2004; Wang et al., 2006b, Wang and Zhou 2014), dehydrations caused by the simulated martian atmospheric conditions should have also occurred.

5.2. Amorphization

Amorphization of salts in this study is judged by Raman and XRD data analyses, with Raman analysis made on the *as is* surface of ESD products, and XRD analysis made on the bulk sample of ESD products. Three stages of amorphization can be distinguished based on Raman data analyses (Table 3), as Amor-I, Amor-II, and Amor-III. For the Amor-I group, such as those observed from Na_2SO_4, $CaSO_4{\cdot}2H_2O$, and Na_2SO_3 after 7h ESD (Fig. 13, 14, 15), the obvious broadening of major Raman peaks indicates the initiation of structural distortion from a perfect crystalline phase, which is commonly accompanied by the raising of spectral background and reduction of signal to noise (S/N). Structural distortion would generate the observed changes in chemical bond lengths and bond angles in a crystal, causing a much wider Raman peak to be obtained from a vibrational mode. The envelope of many Raman peaks with slightly different central positions widens because of many slightly different chemical bonds in a distorted structure, and an overall reduced S/N. Raman spectra of Amor-III exhibit a total loss of spectral details, in many cases with merged peaks in ν_1, ν_2, ν_3, and ν_4 modes, extensively broadened peak widths (> 10 times), and very low S/N, observed from $MgSO_4{\cdot}yH_2O$ (y=7, 4), $FeSO_4{\cdot}yH_2O$ (y=7, 4), $Fe_{4.67}(SO_4)_6(OH)_2{\cdot}20H_2O$, $FeCl_2{\cdot}4H_2O$ after the ESD process (Fig. 5a, 7b, spectra #4 to #8 in Fig. 12b, spectra #3 to #6 in Fig. 18). The spectra of Amor-II have characteristics between those of Amor-I and Amor-III, such as the ESD product of $MgSO_4{\cdot}H_2O$ shown in Fig. 5b.

Two stages of amorphization can be distinguished from the XRD data (Table 3), corresponding to Amor-III and the combined Amor-I and –II assigned by Raman results. Amor-III would appear as the "large hump" in the XRD patterns from the ESD products from $MgSO_4{\cdot}yH_2O$ (y=7, 4) (Fig. 6), $FeSO_4{\cdot}7H_2O$ (Fig.9), $FeCl{\cdot}4H_2O$ (Fig. 19), and $AlCl_3.6H_2O$ (Fig. 23), consistent with Amor-III assigned by Raman analyses. Because XRD sampled the powder from the full depth of the SiO_2 cell including the bottom of cell that is less affected by energetic electrons, some XRD lines of crystalline phases may overlie the "large hump" (Fig. 6, 9, 19) while the Raman spectra from the *as is* surface show full amorphization (Fig. 5a, 18). The XRD pattern of the products assigned to Amor-I and Amor-II by Raman analysis would appear as line broadening and the merge of line groups, as seen in Figure 6 (1.5h-ESD from $MgSO_4{\cdot}H_2O$), Figure 16 (7h ESD from $NaHSO_3$), and Figure 23 (LT- 7h ESD from $MgCl_2{\cdot}6H_2O$).

It is worth noting that the generation of Amor-III is normally accompanied by the rapid dehydration from sulfates originally having high degrees of hydration, such as from $MgSO_4{\cdot}xH_2O$ (x=4, 7), $FeSO_4{\cdot}xH_2O$ (x=4,7), and $Fe_{4.67}(SO_4)_6(OH)_2{\cdot}20H_2O$. Amor-I or Amor-II occurred in anhydrous sulfates (e.g., Na_2SO_4, Na_2SO_3) or those with a low degree of hydration, e.g., $MgSO_4{\cdot}H_2O$.

The rate of amorphization (i.e., the ease of damaging the crystalline structure) of common chlorides appears to be more related to the type of cations present, and reflected by a grouping of chlorides mentioned in section 4.2.2, i.e., higher rates in Fe, Mg, and Al chlorides than in Ca, Na, and K chlorides. The same grouping was found in experimentally observed rates of Cl-release induced by ESD from Mg, Fe, Al, Ca, Na, and K chlorides (Wang et al., 2020), which was correlated with the degree of M - Cl bond covalence that is usually quantified by the difference of electronegativity of M and Cl (Allred, 1961). These electronegativity differences range from 2.34 to 2.16 for KCl, NaCl, and $CaCl_2$, and from 1.2 to 1.85 for $FeCl_3$, $AlCl_3$, $FeCl_2$, and $MgCl_2$ (Wang et al., 2020). An apparent connection between amorphization and dehydration is observed in chlorides. Hydrous chlorides ($AlCl_3{\cdot}6H_2O$, $FeCl_2{\cdot}4H_2O$, $MgCl_2{\cdot}6H_2O$) appeared to amorphize more quickly (Fig. 19, 23) than anhydrous chlorides (NaCl, KCl, Fig. 22). Nevertheless, the ESD-induced Cl-release experiments were conducted strictly on anhydrous chlorides (KCl, NaCl, $CaCl_2$, $FeCl_3$, $AlCl_3$, $FeCl_2$, and $MgCl_2$), and the same grouping was found in two sets of experiments (Wang et al., 2020, and this study). We conclude that the rate of amorphization of the tested chlorides is fundamentally affected by the degree of M - Cl bond covalence.

5.3. Oxidation

Oxidation of Fe^{2+} to Fe^{3+} is evidenced by Mössbauer analyses of the ESD products from $FeSO_4 \cdot 7H_2O$ and $FeCl_2 \cdot 4H_2O$. The ratio of Fe^{3+}/Fe_{total} in both cases changed from zero to 44%, and to 88%, respectively, after a medium-strength ESD process of only 7 hours. These Mössbauer results are confirmed by the slope change in the 400-800 nm range of VNIR spectra, particularly as seen in the ESD-product set from $FeCl_2 \cdot 4H_2O$ (Fig. 21). The hydrolysis from $Fe^{2+}SO_4 \cdot H_2O$ to $Fe^{3+}(OH)SO_4$ revealed by Raman spectra (Fig. 8) and by XRD-based phase ID (Fig. 9), and the appearance of $Fe^{3+}OCl$ in the ESD product of $FeCl_2 \cdot 4H_2O$ (Fig. 19), provide additional evidence of the oxidation of ferrous iron to ferric iron, induced by the ESD process.

During a normal glow discharge (ESD-NGD) in simulated Mars atmospheric composition and pressure, the free radicals CO^{2+}, CO^{+}, O_I, H_{III}, H_{II}, *OH*, Ar_I, N_2, N_2^{+} (as well as O_2, *NO, and* O^{+} because of the overlapping of plasma lines used for detection, Figure S8) were detected instantaneously by *in situ* plasma emission spectroscopy. O_3 was also detected in the output gas by UV and mid-IR spectroscopy (Wu et al., 2018). These free radicals would induce the oxidation of Fe^{2+} to Fe^{3+}. Similarly, oxidation of Cl^{-} to Cl^{7+} was indicated in this study by the presence of $Mg(ClO_4)_2 \cdot 6H_2O$ in 21h ESD products from $MgCl_2 \cdot 6H_2O$ (section 4.2.2). In addition, Wu et al. (2018) observed the formation of $NaClO_3$ and $NaClO_4$ from NaCl, both induced by the ESD processes of medium strength (Table S1).

Finally, our hypothesis of S-oxidation induced by ESD process was validated by the analyses of ESD products from two sulfites, $Na_2S^{4+}O_3$ and $NaHS^{4+}O_3$. The XRD-based identification of $Na_2S^{6+}{}_3O_{10}$ in ESD products (Fig. 16) supports the oxidation hypothesis, as does the IC observation of a surge in SO_4 concentration with increasing ESD duration (Fig. 17).

Overall, the results of this study demonstrated that dehydration and amorphization (to different degrees depending on the properties of salts) were induced by the medium-strength ESD processes within a nominal time duration from 0.25 hours to 7 hours. In addition, oxidation of Cl, S, and Fe occurred in Cl-, S-, and Fe-bearing salts as a result of this type of ESD process.

6. Implications for martian dust activities

Martian dust activities have been physically altering the morphology of the martian surface. Some of them, especially the regional and global dust storms, have the potential to physically remove and re-deposit the top layer of regolith and even rocks if secondary minerals (salts and phyllosilicates) are the major components. When electrostatic discharge is induced by martian dust activity, it exerts two additional effects on surface minerals: physically impacting them with energetic electrons and chemically attacking them with free radicals and electrons. The potential effects in chemistry and biology of ESD induced by Mars dust activities have been investigated and reported by Wu et al. (2018), and Wang et al. (2020a, b and this study) and by another group in Denmark (Bak et al., 2016, 2017, 2018; Knakjensen et al., 2014; Thoegersen et al., 2019).

To date, there has been no actual measurement made of the electric properties of martian dust events. Thus, two important unknowns remain. First is the probability of the occurrence of an ESD during a dust event, which would be expressed as a percentage of time duration in a dust event. Second is the type of ESD, either *Townsend dark discharge (TDD)*, or *normal glow discharge (NGD)*, that would occur in a specific dust event. Our current investigations (Wu et al., (2018), and Wang et al., 2020a, b, c) revealed the types of phase transformations (with some rate information) that can be induced by a medium-strength NGD, to a group of important secondary martian minerals (S- and Cl-salts). However, the overall effect of these phase transformations on the "*big picture*" of martian surface mineralogy cannot be estimated, unless some assumptions on the above two important unknowns are made.

We will take a very conservative assumption for the first unknown, and consider only two extreme cases: grain saltation and global dust storm. Our terminology in using "dust" in following discussion lumps all particles (dust, sand, soil grains, etc.) that can be physically moved by these two processes

First, grain saltation (GS) can occur on Mars everywhere and all year around when wind speed is beyond a threshold. Atmospheric scientists use *threshold friction speed* (u_{*t}) to judge the generation of GS. An early experiment using a wind tunnel (Greely et al., 1980) found that the u_{*t} at martian condition (at 5 mbar, 95% CO_2, T =150-240K) is about 10 times higher than on Earth, i.e., GS is more difficult to initiate on Mars than on Earth. For example, the u_{*t} for grain size of 100 µm would be 2.5-3.5 m/s, and the u_{*t} for grain size of 800 µm would be 4-5 m/s under Mars conditions (Figure 5 of Greely et al., 1980). When adding the effect of the lower gravitational field of Mars, however, a recent study (Sullivan and Kok, 2017) found that at a wind speed much lower than u_{*t}, "sporadically mobilized" grains on Mars can develop into "self-sustaining saltation." This conclusion was validated by the observations made during the *Spirit*, *Opportunity*, and *Curiosity* rover missions (Sullivan et al., 2005, 2008; Sullivan and Kok, 2017).

Fortunately, a Rover Environmental Monitoring Station (REMS) was carried by *Curiosity* rover to Gale crater. A recent paper (Viudex-Mpreiras et al., 2019) published wind speed data at Gale crater collected by REMS from sol 9 to sol 1474. Their finding was that the *wind speed probability density function* at Gale crater matches quite well with the Weibull function, with a scale factor c= 6.87 m/s and a shape parameter k= 1.73 (Fig.1 of Viudex-Mpreiras et al., 2019; Table S2). Furthermore, they found these parameters fall into the ranges of two Viking landers (which landed on flat plain, c=2.55 – 7.9 m/s, k=1.06 – 1.68). On the basis of this REMS data set collected during 2.19 Mars years, the probability of wind speed > 3.5 m/s is 70% and of wind speed > 5 m/s is 53%, at Gale crater (Table S2). Therefore, even we take the most conservative consideration by using the high *threshold friction speed* (u_{*t}) derived by the Greely et al. (1980) experiments (> 5 m/s for grain size of 800 µm), the winds at Gale crater would induce grain saltation (GS) over half of a martian year (53%, Table 4).

Schmidt et al. (1998) measured the E-fields in saltating grains at a California field site and found a level as high as 166 kV/m (>> 25-34 kV/m BEFT measured in Mars environmental chambers, Farrell et al., 2015; Yan et al., 2017). Since there was no actual measurement of the electric properties of grain saltation made on Mars and counting the other uncertainties in ESD generation that beyond the scope of current study, we chose a very conservative number, 1%, to estimate the ESD occurrence probability induced by martian grain saltation (GS). Combined with the occurring probability of GS during a Mars year at specific sites (e.g., Gale crater), the resulting probability of a GS-induced ESD would be 5.3×10^{-3}, equal to 87 hours during a martian year (Table 4).

Other martian dust activities, e.g., dust devils and dust storms, would disturb the martian surface dust and sand to much larger degrees than that by grain saltation. For simplification, we use global dust storm (GDS) to make a rough numerical calculation for comparison purposes. In general, GDS occurs on average once every three martian years. Once it occurs, it can be roughly assumed to cover at least 80% of the martian surface and last 10% of a martian year, corresponding ~ 69 Earth days (Gierasch, 1974; Shirley, 2015; Wang and Richardson, 2015). Therefore, the probability of any location on Mars during a martian year encountering a GDS is 0.026, or 435 hours (Table 4).

Now the question is: what is the percentage of time during a GDS that ESD could occur? Based on decades of study of martian dust storms, we understand that GDS are driven by a set of hot cores. Within the cores, there is likely convective activity, which could generate large electric fields (E-field) that would eventually cause an ESD to occur. During a GDS, the dust in these cores then gets transported to high altitudes and covers the globe of Mars. Therefore in the regions away from the cores, the dust load increases, but it is not vigorously mixing dust. The amount of suspended small aerosols increases, but there is probably not a lot of electrical activity away from the cores (Gierasch, 1974). Considering this model and many more remaining uncertainties in martian GDS than GS, we chose a percentage at two orders of magnitude lower, 0.01%, for the probability of ESD occurring during a global dust storm (Table 4). Thus, the probability of encountering ESD as induced by GDS at any location on Mars during a martian year is 2.6×10^{-6} that equals to 4.4×10^{-2} hour (Table 4).

The second unknown is the type of ESD (either *Townsend dark discharge (TDD),* or *normal glow discharge (NGD)*) that would occur in a specific dust event. Based on gas discharge phenomena described in the literature (Fig. S7), the major difference between TDD and NGD is in electron flux. This is reflected by the electric current measured in a discharge event (Gallo, 1975), which was observed at µA level for TDD by Farrell et al., (2015), and at mA level for NGD by Wu et al., (2018), both under Mars atmospheric conditions. Based on a modeling study (Delory et al., 2006), the full range of estimated electron flux between martian TDD and NGD ranges over seven orders of magnitude, from 9×10^{16} $s^{-1}m^{-2}$ (TDD) and 1.5×10^{24} $s^{-1}m^{-2}$ (NGD) (detailed discussion in section 5.3 of Wu et al., 2018**).** An ESD-NGD was observed in our experimental setting, with an electron flux of 1.42×10^{20} $s^{-1}m^{-2}$ (Table S1) calculated on the basis of measured electric current across the two electrodes, a strength at mid-way between the two extreme cases.

On the other hand, the type of chemical reaction that could be induced by an ESD process depends on the kinetic energy ($\boldsymbol{E_k}$) of electrons being generated, i.e., $\boldsymbol{E_k}$ > an energy threshold for a chemical reaction to occur. As discussed in Wu et al. (2018) and discussed in section 3.2, the kinetic energy of electrons generated in our ESD experiments was estimated on the basis of plasma spectroscopic observations of CO_2^+ and H_α lines, with considerable portion of electrons having $\boldsymbol{E_k}$ >14 eV and even > 17.2 eV. Because the drift velocities of electrons in TDD and NGD are similar (Fig. 4a and equation (8) of Delory et al., 2006; Jackson et al., 2008, 2010), their electrons should have similar kinetic energy distributions. Therefore, the chemical reactions induced by NGD can also be induced by TDD. However, the same reaction induced by the TDD process will take much longer time than NGD to reach the same level of phase transformation because of its lower electron flux (Fig. S7). For example, the electron flux realized in our NGD experiments is about $\sim 10^4$ times of that of typical TDD, thus the mineral transformation produced by a 0.25h ESD-NGD in our experiments (Table 3) would only be seen after about 2500 hours of a typical TDD process.

We further assume that NGD would more likely be induced by dust storms, while TDD would more likely be induced by grain saltation, simply because the difference in the amounts of dust grains involved in these two extreme dust activities matches well with the differences in electron flux densities of NGD and TDD, which are at mA and µA levels, respectively, when measuring electric current under Mars conditions (Farrell et al., 2015; Wu et al., 2018).

Based on the above assumptions and considering only the grain saltation and the global dust storms (and the probabilities derived in the front part of this section), we can make very rough estimations on how long it would take on Mars to reach the levels of phase transformations induced by our medium-strength ESD-NGD process in PEACh. The last two rows of Table 4 show that the phase transformations produced by a 0.25h-ESD-NGD process in the PEACh (column #3 of Table 3) would likely be seen after > 29 martian years when considering only the grain saltation induced ESD-TDD (at typical TDD electron flux level, Table S1). The time would be > 5.7 martian years when considering only the global dust storms induced ESD-NGD (at the same electron flux level of our experiments, Table S1). The durations needed for the phase transformation levels reached by 7h ESD-NGD (column #4 of Table 3) would likely be seen on Mars after a few hundred martian years for both extreme cases (grain saltation and global dust storms).

Note that the choice of ESD-occurring probabilities in the above analyses (1% for grain saltation and 0.01% for global dust storms), although based on some knowledge, maintains certain arbitrary nature because no real measurements have yet been made on Mars. Our goal was to enable a rough estimation on the numbers of martian years (Table 4), after which the phase transformations observed in our experiments (dehydration, amorphization, and oxidations of Fe, Cl, and S) would be seen on Mars. The estimated time lengths would be 10 to 100 times longer if we chose to further reduce the probability by one to two order of magnitude for both extreme dust activities, which would result an estimation of thousands to tens' thousands martian years. Nevertheless, the cold and dry atmospheric conditions have prevailed during Amazonian period (~ 3 Ga), especially in the most recent tens' of million years, during which martian dust activities (dust storms, dust devil, and grain saltation) have been rampantly altering martian surface materials. Our experimental results suggest that ESD induced by martian dust activities may have contributed some of the S- and Cl-rich X-ray amorphous materials in surface soils at Gale crater.

Furthermore, compared with the high frequency of occurrence, large area, and long temporal coverage of martian dust activities in the current epoch on Mars, the other potential amorphization processes, i.e., the sudden exposure of subsurface hydrous salts or a sudden release of subsurface brines (section 1) that might be induced by impacts or by other events such as Recurring Slope Lineae (RSL) would result in mostly localized occurrences with a lower probability of occurrence. This comparison suggests that the ESD process induced by martian dust activities could be a very important process during the Amazonian period on Mars in causing the generation of S- and Cl-rich amorphous materials and the oxidation of Fe, S, and Cl. A direct implication of this conclusion is that we would anticipate significant amounts of S- and Cl-rich amorphous materials, with highly oxidized Cl, S, and Fe, over the entire surface of Mars.

7. Acknowledgements

All coauthors claim no conflict of interest in publishing this manuscript.
Additional data that support this manuscript can be found in Supporting Information document. The digital file corresponding the spectral data in figures of this manuscript is available (Wang et al., 2020b), no user ID and password are required to access these data.

This laboratory experimental investigation was supported by NASA SSW-80NSSC17K0776. We are thankful to Prof. R. Arvidson and Mr. P. Carpenter in the Department of Earth & Planetary Sciences for their help in using the ASD spectrometer and the XRD instrument, and their advice regarding the data analyses. We thank Dr. Z. C. Wu for his effort in building the initial ESD setup in the PEACh during his visit to WUSTL during 2015-2016. Furthermore, we are grateful to the McDonnell Center for the Space Sciences (MCSS) at WUSTL for specific financial support (94351A) to continue our collaboration with Chinese planetary scientists and students. EBS and HKQ thank the China Scholarship Council (201806220274 and 201906280336) for supporting their PhD studies at WUSTL.

8. Authors contributions

AW designed the experimental investigations. YCY did the sample preparations and conducted the ESD experiments in the PEACh, with the help of HKQ. AW conducted the analyses using Raman, VNIR spectroscopy, and XRD diffractometry, with the help of EBS. DMD and JH performed Mössbauer and IC analyses of ESD products and data interpretations. WMF provided scientific support for the ESD process in martian dust activity, especially the implication study. BLJ and SMM examined the experimental results and the conclusions derived from them. All coauthors participated in the manuscript writing.

9. References

Achilles, C. N., Downs, R. T., Ming, D. W., Rampe, E. B., Morris, R. V, Treiman, A. H., et al. (2017). Mineralogy of an active eolian sediment from the Namib dune, Gale crater, Mars. *Journal of Geophysical Research: Planets*, *122*(11), 2344–2361. https://doi.org/10.1002/2017JE005262

Aerts, R., Somers, W., & Bogaerts, A. (2015). Carbon Dioxide Splitting in a Dielectric Barrier Discharge Plasma: A Combined Experimental and Computational Study. *ChemSusChem*, *8*(4), 702–716. https://doi.org/10.1002/cssc.201402818

Allred, A. L. (1961). Electronegativity values from thermochemical data. *Journal of Inorganic and Nuclear Chemistry*, *17*(3), 215–221. https://doi.org/https://doi.org/10.1016/0022-1902(61)80142-5

Anthony, J. W., R. A. Bideaux, K. W. Bladh, and M. C. Nichols (1990–2003), Handbook of Mineralogy, Mineralog. Soc. Am., Chantilly, VA. http://www.handbookofmineralogy.org/

Bak, E N, Larsen, M. G., Jensen, S. K., Nørnberg, P., Moeller, R., & Finster, K. (2018). Wind-Driven Saltation: An Overlooked Challenge for Life on Mars. *Astrobiology*, *19*(4), 497–505. https://doi.org/10.1089/ast.2018.1856

Bak, Ebbe N, Jensen, S. J. K., Nørnberg, P., & Finster, K. (2016). Methylated silicates may explain the release of chlorinated methane from Martian soil. *Earth and Planetary Science Letters*, *433*, 226–231. https://doi.org/https://doi.org/10.1016/j.epsl.2015.10.044

Bak, Ebbe N, Zafirov, K., Merrison, J. P., Jensen, S. J. K., Nørnberg, P., Gunnlaugsson, H. P., & Finster, K. (2017). Production of reactive oxygen species from abraded silicates. Implications for the reactivity of the Martian soil. *Earth and Planetary Science Letters*, *473*, 113–121. https://doi.org/https://doi.org/10.1016/j.epsl.2017.06.008

Bak, Ebbe N, Larsen, M. G., Moeller, R., Nissen, S. B., Jensen, L. R., Nørnberg, P., et al. (2017). Silicates Eroded under Simulated Martian Conditions Effectively Kill Bacteria—A Challenge for Life on Mars . *Frontiers in Microbiology* . Retrieved from https://www.frontiersin.org/article/10.3389/fmicb.2017.01709

Bish, D. L., Blake, D. F., Vaniman, D. T., Chipera, S. J., Morris, R. V, Ming, D. W., et al. (2013). X-ray Diffraction Results from Mars Science Laboratory: Mineralogy of Rocknest at Gale crater. *Science*, *341*(6153), 1238932. https://doi.org/10.1126/science.1238932

Blake, D. F., Morris, R. V, Kocurek, G., Morrison, S. M., Downs, R. T., Bish, D., et al. (2013). Curiosity at Gale Crater, Mars: Characterization and Analysis of the Rocknest Sand Shadow. *Science*, *341*(6153), 1239505. https://doi.org/10.1126/science.1239505

Byrne, S., Dundas, C. M., Kennedy, M. R., Mellon, M. T., McEwen, A. S., Cull, S. C., et al. (2009). Distribution of Mid-Latitude Ground Ice on Mars from New Impact Craters. *Science*, *325*(5948), 1674 LP – 1676. https://doi.org/10.1126/science.1175307

Cantor, B. A., Kanak, K. M., & Edgett, K. S. (2006). Mars Orbiter Camera observations of Martian dust devils and their tracks (September 1997 to January 2006) and evaluation of theoretical vortex models. *Journal of Geophysical Research: Planets*, *111*(E12). https://doi.org/10.1029/2006JE002700

Chandra, S., & Hoy, G. R. (1966). Mössbauer studies of quadrupole and hyperfine interactions in FeCl2·2H2O. *Physics Letters*, *22*(3), 254–256. https://doi.org/https://doi.org/10.1016/0031-9163(66)90598-1

Cheetham, A. K., Cole, A. J., & Long, G. J. (1981). Investigation of the mixed-metal sulfide (Mn,Fe)S2 by analytical electron microscopy and Moessbauer spectroscopy. *Inorganic Chemistry*, *20*(9), 2747–2750. https://doi.org/10.1021/ic50223a001

Chio, C. H., Sharma, S. K., & Muenow, D. W. (2007). The hydrates and deuterates of ferrous sulfate (FeSO4): a Raman spectroscopic study. *Journal of Raman Spectroscopy*, *38*(1), 87–99. https://doi.org/10.1002/jrs.1623

Choi, D. S., & Dundas, C. M. (2011). Measurements of Martian dust devil winds with HiRISE. *Geophysical Research Letters*, *38*(24). https://doi.org/10.1029/2011GL049806

Dehouck, E., McLennan, S. M., Meslin, P.-Y., & Cousin, A. (2014). Constraints on abundance, composition, and nature of X-ray amorphous components of soils and rocks at Gale crater, Mars. *Journal of Geophysical Research: Planets*, *119*(12), 2640–2657. https://doi.org/10.1002/2014JE004716

Dehouck, E., McLennan, S. M., Sklute, E. C., & Dyar, M. D. (2017). Stability and fate of ferrihydrite during episodes of water/rock interactions on early Mars: An experimental approach. *Journal of Geophysical Research: Planets*, *122*(2), 358–382. https://doi.org/10.1002/2016JE005222

Delory, G. T., Farrell, W. M., Atreya, S. K., Renno, N. O., Wong, A.-S., Cummer, S. A., et al. (2006). Oxidant Enhancement in Martian Dust Devils and Storms: Storm Electric Fields and Electron Dissociative Attachment. *Astrobiology*, *6*(3), 451–462. https://doi.org/10.1089/ast.2006.6.451

Dyar, M. D., Breves, E., Jawin, E., Marchand, G., Nelms, M., O'Connor, V., et al. (2013). Mössbauer parameters of iron in sulfate minerals†. *American Mineralogist*, *98*(11–12), 1943–1965. https://doi.org/10.2138/am.2013.4604

Eissa, N. A., Sallam, H. A., Sheta, N. H., Radwan, S. N., & Soliman, M. A. (1994). Moessbauer study of the role of Fe22 /Fe3+ ratio and water of hydration on the optical and electrical properties of gamma irradiated melanterite. *Arab Journal of Nuclear Sciences and Applications*, 27(2), 143–154. Retrieved from http://inis.iaea.org/search/search.aspx?orig_q=RN:25068711

Eissa, N. A., Sheta, N. H., El Mossalamy, S. M., Soliman, M. A., & El Fouly, M. H. (1994). Study of the dehydration process of melanterite under heat treatment and gamma irradiation effects using Moessbauer spectroscopy and thermal analysis measurements. *Arab Journal of Nuclear Sciences and Applications*, *27*(2), 33–45. Retrieved from http://inis.iaea.org/search/search.aspx?orig_q=RN:25068893

Ellehoj, M. D., Gunnlaugsson, H. P., Taylor, P. A., Kahanpää, H., Bean, K. M., Cantor, B. A., et al. (2010). Convective vortices and dust devils at the Phoenix Mars mission landing site. *Journal of Geophysical Research: Planets*, *115*(E4). https://doi.org/10.1029/2009JE003413

Esposito, F., Molinaro, R., Popa, C. I., Molfese, C., Cozzolino, F., Marty, L., et al. (2016). The role of the atmospheric electric field in the dust-lifting process. *Geophysical Research Letters*, *43*(10), 5501–5508. https://doi.org/10.1002/2016GL068463

Farrell, W. M., Smith, P. H., Delory, G. T., Hillard, G. B., Marshall, J. R., Catling, D., et al. (2004).

Electric and magnetic signatures of dust devils from the 2000–2001 MATADOR desert tests. *Journal of Geophysical Research: Planets*, *109*(E3). https://doi.org/10.1029/2003JE002088

Farrell, W. M., McLain, J. L., Collier, M. R., Keller, J. W., Jackson, T. J., & Delory, G. T. (2015). Is the electron avalanche process in a martian dust devil self-quenching? *Icarus*, *254*, 333–337. https://doi.org/https://doi.org/10.1016/j.icarus.2015.04.003

Farrell, W. M., McLain, J. L., Collier, M. R., & Keller, J. W. (2017). The Martian dust devil electron avalanche: Laboratory measurements of the E-field fortifying effects of dust-electron absorption. *Icarus*, *297*, 90–96. https://doi.org/https://doi.org/10.1016/j.icarus.2017.06.001

Ferri, F., Smith, P. H., Lemmon, M., & Rennó, N. O. (2003). Dust devils as observed by Mars Pathfinder. *Journal of Geophysical Research: Planets*, *108*(E12). https://doi.org/10.1029/2000JE001421

Forward, K. M., Lacks, D. J., & Sankaran, R. M. (2009). Particle-size dependent bipolar charging of Martian regolith simulant. *Geophysical Research Letters*, *36*(13). https://doi.org/10.1029/2009GL038589

Fu, X., Wang, A. (2017). Crystallinity effects on spectral features of amorphous saponite and

Implication for poorly crystalline phyllosilicates on mars, Abstract #2977 to 48th LPSC

Gallo, C. F. (1975). Coronas and Gas Discharges in Electrophotography: A Review. *IEEE Transactions on Industry Applications*, *IA-11*(6), 739–748. https://doi.org/10.1109/TIA.1975.349370

Grant, R. W., Wiedersich, H., Muir, A. H., Gonser, U., & Delgass, W. N. (1966). Sign of the Nuclear Quadrupole Coupling Constants in Some Ionic Ferrous Compounds. *The Journal of Chemical Physics*, *45*(3), 1015–1019. https://doi.org/10.1063/1.1727651

Greeley, R, Leach, R., White, B., Iversen, J., & Pollack, J. (1980). Threshold windspeeds for sand on Mars: Wind tunnel simulations. *Geophysical Research Letters*, *7*(2), 121–124. https://doi.org/10.1029/GL007i002p00121

Greeley, Ronald, Whelley, P. L., Arvidson, R. E., Cabrol, N. A., Foley, D. J., Franklin, B. J., et al. (2006). Active dust devils in Gusev crater, Mars: Observations from the Mars Exploration Rover Spirit. *Journal of Geophysical Research: Planets*, *111*(E12). https://doi.org/10.1029/2006JE002743

Greeley, Ronald, Waller, D. A., Cabrol, N. A., Landis, G. A., Lemmon, M. T., Neakrase, L. D. V, et al. (2010). Gusev Crater, Mars: Observations of three dust devil seasons. *Journal of Geophysical Research: Planets*, *115*(E7). https://doi.org/10.1029/2010JE003608

Gellert et al., (2006). Alpha Particle X-Ray Spectrometer (APXS): Results from Gusev crater and calibration report. J. Geophys. Research, 111, E02S05, doi:10.1029/2005JE002555.

Harrison, R. G., Barth, E., Esposito, F., Merrison, J., Montmessin, F., Aplin, K. L., et al. (2016). Applications of Electrified Dust and Dust Devil Electrodynamics to Martian Atmospheric Electricity. *Space Science Reviews*, *203*(1), 299–345. https://doi.org/10.1007/s11214-016-0241-8

Huggins, F. E., & Huffman, G. P. (1979). Chapter 50 - Mössbauer Analysis of Iron-Bearing Phases in Coal, Coke, and Ash. In C. B. T.-A. M. for C. and C. P. KARR (Ed.) (pp. 371–423). Academic Press. https://doi.org/https://doi.org/10.1016/B978-0-12-399903-0.50019-2

Itikawa, Y., & Mason, N. (2005). Cross Sections for Electron Collisions with Water Molecules. *Journal* *of Physical and Chemical Reference Data*, *34*(1), 1–22. https://doi.org/10.1063/1.1799251

Jackson, T L, & Farrell, W. M. (2006). Electrostatic fields in dust devils: an analog to Mars. *IEEE Transactions on Geoscience and Remote Sensing*, *44*(10), 2942–2949. https://doi.org/10.1109/TGRS.2006.875785

Jackson, Telana L, Farrell, W. M., Delory, G. T., & Nithianandam, J. (2008). Effect of dust absorption on the electron avalanche process occurring within Martian dust storms. *Geophysical Research Letters*, *35*(16). https://doi.org/10.1029/2008GL034523

Jackson, Telana L, Farrell, W. M., Delory, G. T., & Nithianandam, J. (2010). Martian dust devil electron avalanche process and associated electrochemistry. *Journal of Geophysical Research: Planets*, *115*(E5). https://doi.org/10.1029/2009JE003396

Johnson, C. E. (1966). A M ssbauer effect study of the magnetic properties of FeCl2.2H2O. *Proceedings of the Physical Society*, *88*(4), 943–955. https://doi.org/10.1088/0370-1328/88/4/317

Kandel, L., Weber, M. A., Frankel, R. B., & Abeledo, C. R. (1974). Mössbauer spectroscopy of magnetic phases in FeCl2 · 2H2O. *Physics Letters A*, *46*(6), 369–370. https://doi.org/https://doi.org/10.1016/0375-9601(74)90920-7

Knak Jensen, S. J., Skibsted, J., Jakobsen, H. J., ten Kate, I. L., Gunnlaugsson, H. P., Merrison, J. P., et al. (2014). A sink for methane on Mars? The answer is blowing in the wind. *Icarus*, *236*, 24–27. https://doi.org/https://doi.org/10.1016/j.icarus.2014.03.036

Krauss, C. E., Hor nyi, M., & Robertson, S. (2003). Experimental evidence for electrostatic discharging of dust near the surface of Mars. *New Journal of Physics*, *5*, 70. https://doi.org/10.1088/1367-2630/5/1/370

Lemmon, M. T., Wolff, M. J., Bell, J. F., Smith, M. D., Cantor, B. A., & Smith, P. H. (2015). Dust aerosol, clouds, and the atmospheric optical depth record over 5 Mars years of the Mars Exploration Rover mission. *Icarus*, *251*, 96–111. https://doi.org/https://doi.org/10.1016/j.icarus.2014.03.029

Lide, 2001, Handbook of Chemistry & Physics, 82nd edition, by CRC, London.

Ling, Z., & Wang, A. (2015). Spatial distributions of secondary minerals in the Martian meteorite MIL 03346,168 determined by Raman spectroscopic imaging. *Journal of Geophysical Research: Planets*, *120*(6), 1141–1159. https://doi.org/10.1002/2015JE004805

Ling, Z. C., Wang, A., & Jolliff, B. L. (2011). Mineralogy and geochemistry of four lunar soils by laser-Raman study. *Icarus*, *211*(1), 101–113. https://doi.org/https://doi.org/10.1016/j.icarus.2010.08.020

McEwen, A. S., Dundas, C. M., Mattson, S. S., Toigo, A. D., Ojha, L., Wray, J. J., et al. (2014). Recurring slope lineae in equatorial regions of Mars. *Nature Geoscience*, *7*(1), 53–58. https://doi.org/10.1038/ngeo2014

McLennan, S. M., Grotzinger, J., (2008). The sedimentary rock cycle of Mars. The Martian Surface-Composition, Mineralogy, and Physical Properties, Cambridge University Press, New York

McLennan, S. M. (2012). Geochemistry of sedimentary processes on Mars. Sedimentary Geology of Mars, 102, 119–138. https://doi.org/10.2110/pec.12.102.0119

McLennan, S. M., Anderson, R. B., Bell, J. F., Bridges, J. C., Calef, F., Campbell, J. L., et al. (2014).

Elemental Geochemistry of Sedimentary Rocks at Yellowknife Bay, Gale crater, Mars. *Science*, *343*(6169), 1244734. https://doi.org/10.1126/science.1244734

McLennan, S. M, Grotzinger, J. P., Hurowitz, J. A., & Tosca, N. J. (2019). The Sedimentary Cycle on Early Mars. *Annual Review of Earth and Planetary Sciences*, *47*(1), 91–118. https://doi.org/10.1146/annurev-earth-053018-060332

Melnik, O., & Parrot, M. (1998). Electrostatic discharge in Martian dust storms. *Journal of Geophysical Research: Space Physics*, *103*(A12), 29107–29117. https://doi.org/10.1029/98JA01954

Metzger, S. M., Carr, J. R., Johnson, J. R., Parker, T. J., & Lemmon, M. T. (1999). Dust devil vortices seen by the Mars Pathfinder Camera. *Geophysical Research Letters*, *26*(18), 2781–2784. https://doi.org/10.1029/1999GL008341

Morris, R. V., Vaniman, D. T., Blake, D. F., Gellert, R., Chipera, S. J., Rampe, E. B., et al. (2016). Silicic volcanism on Mars evidenced by tridymite in high-SiO₂ sedimentary rock at Gale crater. *Proceedings of the National Academy of Sciences*, *113*(26), 7071 LP – 7076. https://doi.org/10.1073/pnas.1607098113

Morrison, S. M., Downs, R. T., Blake, D. F., Vaniman, D. T., Ming, D. W., Hazen, R. M., et al. (2018). Crystal chemistry of martian minerals from Bradbury Landing through Naukluft Plateau, Gale crater, Mars. *American Mineralogist*, *103*(6), 857–871. https://doi.org/10.2138/am-2018-6124

Morrison, S. M., Downs, R. T., Blake, D. F., Prabhu, A., Eleish, A., Vaniman, D. T., et al. (2018). Relationships between unit-cell parameters and composition for rock-forming minerals on Earth, Mars, and other extraterrestrial bodies. *American Mineralogist*, *103*(6), 848–856. https://doi.org/https://doi.org/10.2138/am-2018-6123

Morris, R. V., Rampe, E. B., Graff, T. G., Archer Jr, P. D., Le, L., Ming, D. W., & Sutter, B. (2015). Transmission X-Ray Diffraction (XRD) Patterns Relevant to the MSL CheMin Amorphous Component: Sulfates and Silicates, Abs #2434, 46th LPSC

Montano, P.A. (1981) Transformations and role of iron sulfides in coal liquefaction. Bulletin of the American Physical Society, 26, 201–201

Murphy, J., Steakley, K., Balme, M., Deprez, G., Esposito, F., Kahanpää, H., et al. (2016). Field Measurements of Terrestrial and Martian Dust Devils. *Space Science Reviews*, *203*(1), 39–87. https://doi.org/10.1007/s11214-016-0283-y

Ohshita, T., Nakajima, D., Tsukamoto, A., Tsuchiya, N., Isobe, T., Senna, M., et al. (2002). Role of molecular strain on the solid-state synthesis of coordination compounds from iron(II) chloride tetrahydrate and 1,10-phenanthroline under mechanical stress. *Annales de Chimie Science Des Matériaux*, *27*(6), 91–101. https://doi.org/https://doi.org/10.1016/S0151-9107(02)90017-6

Ôno, K., Ito, A., & Fujita, T. (1964). The Mössbauer Study of the Ferrous Ion in FeCl2. *Journal of the Physical Society of Japan*, *19*(11), 2119–2126. https://doi.org/10.1143/JPSJ.19.2119

Rampe, E. B., Ming, D. W., Blake, D. F., Bristow, T. F., Chipera, S. J., Grotzinger, J. P., et al. (2017). Mineralogy of an ancient lacustrine mudstone succession from the Murray formation, Gale crater, Mars. *Earth and Planetary Science Letters*, *471*, 172–185. https://doi.org/https://doi.org/10.1016/j.epsl.2017.04.021

Rampe, E. B., Lapotre, M. G. A., Bristow, T. F., Arvidson, R. E., Morris, R. V, Achilles, C. N., et al. (2018). Sand Mineralogy Within the Bagnold Dunes, Gale crater, as Observed In Situ and From Orbit. *Geophysical Research Letters*, *45*(18), 9488–9497. https://doi.org/10.1029/2018GL079073

Reiss, D., Zanetti, M., & Neukum, G. (2011). Multitemporal observations of identical active dust devils on Mars with the High Resolution Stereo Camera (HRSC) and Mars Orbiter Camera (MOC). *Icarus*, *215*(1), 358–369. https://doi.org/https://doi.org/10.1016/j.icarus.2011.06.011

Sakai, N., Sekizawa, H., & Ôno, K. (1981). Mössbauer spectroscopic identification of the γ-ray radiolytic product of FeSO4·7H2O as FeSO4OH·2H2O. *Journal of Inorganic and Nuclear Chemistry*, *43*(8), 1731–1734. https://doi.org/https://doi.org/10.1016/0022-1902(81)80373-9

Sallam, H. A., Eissa, N. A., Sheta, N. H., Soliman, M. A., & El Fouly, M. H. (1994). Mössbauer effect, x-ray diffraction and infrared studies of the effect of gamma irradiation on the molecular bonding of melanterite. *Journal of Physics and Chemistry of Solids*, *55*(11), 1175–1180. https://doi.org/https://doi.org/10.1016/0022-3697(94)90196-1

Schmidt, D. S., Schmidt, R. A., & Dent, J. D. (1998). Electrostatic force on saltating sand. *Journal of Geophysical Research: Atmospheres*, *103*(D8), 8997–9001. https://doi.org/10.1029/98JD00278

Shinohara, M. (1977). Mössbauer Effect Study of $FeCl_2 \cdot 4H_2O$ in the Antiferromagnetic State. *Journal of the Physical Society of Japan*, *42*(1), 64–71. https://doi.org/10.1143/JPSJ.42.64

Shirley, J. H. (2015). Solar System dynamics and global-scale dust storms on Mars. *Icarus*, *251*, 128–144. https://doi.org/https://doi.org/10.1016/j.icarus.2014.09.038

Sklute, E C, Jensen, H. B., Rogers, A. D., & Reeder, R. J. (2015). Morphological, structural, and spectral characteristics of amorphous iron sulfates. *Journal of Geophysical Research: Planets*, *120*(4), 809–830. https://doi.org/10.1002/2014JE004784

Sklute, Elizabeth C, Rogers, A. D., Gregerson, J. C., Jensen, H. B., Reeder, R. J., & Dyar, M. D. (2018). Amorphous salts formed from rapid dehydration of multicomponent chloride and ferric sulfate brines: Implications for Mars. *Icarus*, *302*, 285–295. https://doi.org/https://doi.org/10.1016/j.icarus.2017.11.018

Sobron, P., & Wang, A. (2012). A planetary environment and analysis chamber (PEACh) for coordinated Raman–LIBS–IR measurements under planetary surface environmental conditions. *Journal of Raman Spectroscopy*, *43*(2), 212–227. https://doi.org/10.1002/jrs.3017

Spiering, H., Hösl, S., & Vogel, H. (1978). Polarization effects in mössbauer absorption of a FeCl2 · 4 H2O single crystal in an external magnetic field. *Physica Status Solidi (B)*, *85*(1), 87–93. https://doi.org/10.1002/pssb.2220850108

Sullivan, R., & Kok, J. F. (2017). Aeolian saltation on Mars at low wind speeds. *Journal of Geophysical Research: Planets*, *122*(10), 2111–2143. https://doi.org/10.1002/2017JE005275

Sullivan, R., Banfield, D., Bell, J. F., Calvin, W., Fike, D., Golombek, M., et al. (2005). Aeolian processes at the Mars Exploration Rover Meridiani Planum landing site. *Nature*, *436*(7047), 58–61. https://doi.org/10.1038/nature03641

Sullivan, R., Arvidson, R., Bell III, J. F., Gellert, R., Golombek, M., Greeley, R., et al. (2008). Wind-driven particle mobility on Mars: Insights from Mars Exploration Rover observations at “El Dorado” and surroundings at Gusev Crater. *Journal of Geophysical Research: Planets*, *113*(E6). https://doi.org/10.1029/2008JE003101

Sutter, B, McAdam, A. C., Mahaffy, P. R., Ming, D. W., Edgett, K. S., Rampe, E. B., et al. (2017). Evolved gas analyses of sedimentary rocks and eolian sediment in Gale crater, Mars: Results of the Curiosity rover's sample analysis at Mars instrument from Yellowknife Bay to the Namib Dune. *Journal of Geophysical Research: Planets*, *122*(12), 2574–2609. https://doi.org/10.1002/2016JE005225

Sutter, Brad, McAdam, A. C., & Mahaffy, P. R. (2019). Chapter 12 - Volatile Detections in Gale crater Sediment and Sedimentary Rock: Results from the Mars Science Laboratory's Sample Analysis at Mars Instrument. In J. Filiberto & S. P. B. T.-V. in the M. C. Schwenzer (Eds.) (pp. 369–392). Elsevier. https://doi.org/https://doi.org/10.1016/B978-0-12-804191-8.00012-X

Thøgersen, J., Bak, E. N., Finster, K., Nørnberg, P., Jakobsen, H. J., & Knak Jensen, S. J. (2019). Light on windy nights on Mars: A study of saltation-mediated ionization of argon in a Mars-like atmosphere. *Icarus*, *332*, 14–18. https://doi.org/https://doi.org/10.1016/j.icarus.2019.06.025

Toner, J. D., Catling, D. C., & Light, B. (2014). The formation of supercooled brines, viscous liquids, and low-temperature perchlorate glasses in aqueous solutions relevant to Mars. *Icarus*, *233*, 36–47. https://doi.org/https://doi.org/10.1016/j.icarus.2014.01.018

Treiman, A. H., Morris, R. V, Agresti, D. G., Graff, T. G., Achilles, C. N., Rampe, E. B., et al. (2014). Ferrian saponite from the Santa Monica Mountains (California, U.S.A., Earth): Characterization as an analog for clay minerals on Mars with application to Yellowknife Bay in Gale crater†. *American Mineralogist*, *99*(11–12), 2234–2250. https://doi.org/10.2138/am-2014-4763

Vaniman, D T, Bish, D. L., Ming, D. W., Bristow, T. F., Morris, R. V, Blake, D. F., et al. (2014). Mineralogy of a Mudstone at Yellowknife Bay, Gale crater, Mars. *Science*, *343*(6169), 1243480. https://doi.org/10.1126/science.1243480

Vaniman, David T, Bish, D. L., Chipera, S. J., Fialips, C. I., William Carey, J., & Feldman, W. C. (2004). Magnesium sulphate salts and the history of water on Mars. *Nature*, *431*(7009), 663–665. https://doi.org/10.1038/nature02973

Viúdez-Moreiras, D., Gómez-Elvira, J., Newman, C. E., Navarro, S., Marin, M., Torres, J., & de la Torre-Juárez, M. (2019). Gale surface wind characterization based on the Mars Science Laboratory REMS dataset. Part II: Wind probability distributions. *Icarus*, *319*, 645–656. https://doi.org/https://doi.org/10.1016/j.icarus.2018.10.010

Wang A., L. A. Haskin, S. W. Squyres, B. L. Jolliff, L. Crumpler, R. Gellert, C. Schröder, K. Herkenhoff, J. Hurowitz, N. J. Tosca, W. H. Farrand, Robert Anderson, A. T. Knudson, (2006), Sulfate Deposition in Subsurface Regolith in Gusev Crater, Mars, *J. Geophys. Res. 111*, E02S17, doi:10.1029/2005JE002513.

Wang, A., Freeman, J. J., Jolliff, B. L., & Chou, I.-M. (2006). Sulfates on Mars: A systematic Raman spectroscopic study of hydration states of magnesium sulfates. *Geochimica et Cosmochimica Acta*, *70*(24), 6118–6135. doi.org/https://doi.org/10.1016/j.gca.2006.05.022

Wang, A., & Ling, Z. C. (2011). Ferric sulfates on Mars: A combined mission data analysis of salty soils at Gusev crater and laboratory experimental investigations. *Journal of Geophysical Research: Planets*, *116*(E7). https://doi.org/10.1029/2010JE003665

Wang, A., Freeman, J. J., & Jolliff, B. L. (2009). Phase transition pathways of the hydrates of magnesium sulfate in the temperature range 50°C to 5°C: Implication for sulfates on Mars. *Journal of Geophysical Research: Planets*, *114*(E4). https://doi.org/10.1029/2008JE003266

Wang, A., Ling, Z., Freeman, J. J., & Kong, W. (2012). Stability field and phase transition pathways of hydrous ferric sulfates in the temperature range 50°C to 5°C: Implication for martian ferric sulfates. *Icarus*, *218*(1), 622–643. https://doi.org/https://doi.org/10.1016/j.icarus.2012.01.003

Wang, A., & Zhou, Y. (2014). Experimental comparison of the pathways and rates of the dehydration of Al-, Fe-, Mg- and Ca-sulfates under Mars relevant conditions. *Icarus*, *234*, 162–173. https://doi.org/https://doi.org/10.1016/j.icarus.2014.02.003

Wang, A., Jolliff, B. L., Liu, Y., & Connor, K. (2016). Setting constraints on the nature and origin of the two major hydrous sulfates on Mars: Monohydrated and polyhydrated sulfates. *Journal of Geophysical Research: Planets*, *121*(4), 678–694. https://doi.org/10.1002/2015JE004889

Wang, A., Sobron, P., Kong, F., Zheng, M., & Zhao, Y.-Y. S. (2018). Dalangtan Saline Playa in a Hyperarid Region on Tibet Plateau: II. Preservation of Salts with High Hydration Degrees in Subsurface. *Astrobiology*, *18*(10), 1254–1276. https://doi.org/10.1089/ast.2018.1829

Wang, A., Ling, Z., Yan, Y., McEwen, A. S., Mellon, M. T., Smith, M. D., et al. (2019). Subsurface Cl-bearing salts as potential contributors to recurring slope lineae (RSL) on Mars. *Icarus*, *333*, 464–480. https://doi.org/https://doi.org/10.1016/j.icarus.2019.06.024

Wang, A., Yan, Y., Jolliff, B. L., McLennan, S. M., Wang, K., Shi, E., & Farrell, W. M. (2020a). Chlorine Release From Common Chlorides by Martian Dust Activity. *Journal of Geophysical Research: Planets*, *125*(6), e2019JE006283. https://doi.org/10.1029/2019JE006283

Wang, A., Yan, Y. C., Dyar, D., Houghton, J., Farrell, W. M., Jolliff, B., McLennan, S., Shi, E. B., Qu, H. K., (2020b). Dataset for Amorphization of S, Cl-salts by Martian Dust Activities [Data set]. Washington University in St. Louis. https://doi.org/10.7936/E6P1-CC09

Wang, A., Alexander S. Bradley, and Yuanchao Yan (2020c), Destruction of Biomarkers Within Mg-Chlorides by Energetic Electrons, Relevant to Mars And Europa, **A***bstract #2702 for 51st Lunar and Planetary Science Conference.*

Wang, H., & Richardson, M. I. (2015). The origin, evolution, and trajectory of large dust storms on Mars during Mars years 24–30 (1999–2011). *Icarus*, *251*, 112–127. https://doi.org/https://doi.org/10.1016/j.icarus.2013.10.033

Wei, J., Wang, A., Lambert, J. L., Wettergreen, D., Cabrol, N., Warren-Rhodes, K., & Zacny, K. (2015). Autonomous soil analysis by the Mars Micro-beam Raman Spectrometer (MMRS) on-board a rover in the Atacama Desert: a terrestrial test for planetary exploration. *Journal of Raman Spectroscopy*, *46*(10), 810–821. https://doi.org/10.1002/jrs.4656

White, W. B., (1975). The Infrared Spectra of Minerals (Eds: VC Farmer) , Mineralogical Society, London, 87–110.

Wu, Z., Wang, A., Farrell, W. M., Yan, Y., Wang, K., Houghton, J., & Jackson, A. W. (2018). Forming perchlorates on Mars through plasma chemistry during dust events. *Earth and Planetary Science Letters*, *504*, 94–105. https://doi.org/https://doi.org/10.1016/j.epsl.2018.08.040

Yan, Y. C., Wang, A., Wu, Z. C. (2017). A Simulated Electro-Chemical Reaction for the Generation of Oxidants in Near-Surface Atmosphere and the Cl^{-1} to Cl^{+X} Phase Transformation at Martian surface. Abstract #2413 for 48th Lunar and Planetary Science Conference.

Yen, A. S., Ming, D. W., Vaniman, D. T., Gellert, R., Blake, D. F., Morris, R. V, et al. (2017). Multiple stages of aqueous alteration along fractures in mudstone and sandstone strata in Gale crater, Mars. *Earth and Planetary Science Letters*, *471*, 186–198. https://doi.org/https://doi.org/10.1016/j.epsl.2017.04.033

10. Captions of tables and figures

Table 1. Salts used in the ESD process and analysis.

Table 2. Mössbauer parameters obtained from curve fittings.

Table 3. Compilation of analysis results of ESD products of the salts studied.

Table 4. Rough calculations on grain saltation and global-dust-storm-induced ESD probabilities based on mission observations and various assumptions.

Figure 1. Scheme of ESD experimental setup.

Figure 2. Examples of the equilibrated temperatures T_{eq} during ESD experiments on studied salts.

Figure 3. (a) starting $MgCl_2 \cdot 6H_2O$ in a SiO2 cell; (b, c, d) LT-7h ESD product of $MgCl_2 \cdot 6H_2O$ (in a SiO2 cell, and zoom-in)

Figure 4. Raman spectra of 0.25h ESD products from $MgSO_4 \cdot 7H_2O$ in (a) spectral range of fundamental vibrational modes; (b) spectral range of H_2O modes, which are compared with standard Raman spectra of $MgSO_4 \cdot 3H_2O$ (3w), $MgSO_4 \cdot 4H_2O$ (4w), $MgSO_4 \cdot 5H_2O$ (5w), $MgSO_4 \cdot 6H_2O$ (6w).

Figure 5. Raman spectra of 1.5h ESD products: (a) from $MgSO_4 \cdot 4H_2O$ compared with standard spectrum (4w); (b) from $MgSO_4 \cdot H_2O$ compared with standard spectrum (1w).

Figure 6. XRD results of ESD products from $MgSO_4 \cdot 7H_2O$, $MgSO_4 \cdot 4H_2O$. $MgSO_4 \cdot H_2O$, compared with standard XRD patterns of starkeyite ($MgSO_4 \cdot 4H_2O$), Kieserite ($MgSO_4 \cdot H_2O$), and caminite ($MgSO_4 \cdot xMg(OH)_2 \cdot (1\text{-}2x)H_2O$).

Figure 7. Raman spectra of ESD products from $FeSO_4 \cdot 7H_2O$ (using 1% laser power=0.5 mw, Teq < 30°C); (a) First 60 spectra from a 99-spots Raman analysis on *as is* surface of 0.25h ESD product, compared with standard Raman spectra; (b) first 60 spectra of a 120 Raman analysis on as is surface of 7h ESD product.

Figure 8. Raman spectra of ESD products: (a) 1.5h-ESD product from $FeSO_4 \cdot 4H_2O$; (b) products after 1.5h, 8.5h, 15.5h ESD process from $FeSO_4 \cdot H_2O$, compared with standard spectra.

Figure 9. XRD result of LT-7h ESD product (bulk sample) from melanterite $FeSO_4 \cdot 7H_2O$ and szomolnokite $FeSO_4 \cdot H_2O$, compared with standard.

Figure 10. VNIR spectra on as is surfaces of 0.25h, 1h, 3h, 7h ESD (T_{eq}<30°C) from melanterite $FeSO_4 \cdot 7H_2O$.

Figure 11. Mössbauer spectrum and curve fitting results (a, b) of a 7h ESD product from melanterite, $FeSO_4 \cdot 7H_2O$.

Figure 12. Raman spectra of ESD product from ferricopiapite, $Fe_{4.67}(SO_4)_6(OH)_2 \cdot 20H_2O$, compared with standards. (a) Standard spectra of ferricopiapite (ferri), rhomboclase, $FeH(SO_4) \cdot 4H_2O$ (rhom), amorphous $FeS_2(SO_4)_3 \cdot 5H_2O$ (Am5w), anhydrous $Fe_2(SO_4)_3$(anhy), and mikasaite, $Fe_2(SO_4)_3$(mika) (Ling and Wang 2010); (b) Raman spectra of ESD products from ferricopiapite.

Figure 13. Raman spectra of 7h ESD product from Na_2SO_4, compared with the spectrum of starting Na_2SO_4.

Figure 14. Raman spectra of 7h ESD product from $CaSO_4{\cdot}2H_2O$

Figure 15. Raman spectra of 7h ESD products from $NaSO_3$, compared with standard spectra.

Figure 16. XRD results of 7h ESD product from $NaHSO_3$, compared with original salt, and standards.

Figure 17. Results from ion chromatography on 1h, 2h, 7h ESD products from Na_2SO_3.

Figure 18. Typical Raman spectra of ESD-products from $FeCl_2{\cdot}4H_2O$, compared with a standard spectrum of starting $FeCl_2{\cdot}4H_2O$.

Figure 19. XRD pattern of 7h ESD product from $FeCl_2{\cdot}4H_2O$, compared with standards.

Figure 20. Mössbauer spectrum and curve fitting results of a 7h ESD product from $FeCl_2{\cdot}4H_2O$.

Figure 21. VNIR spectra from as is surfaces of 0.25h, 1h, 3h, 7h ESD (T_{eq} <30°C) from $FeCl_2{\cdot}4H_2O$.

Figure 22. XRD results of ESD-7h products from NaCl, KCl, which match with PDF:00-005-0628(NaCl) and PDF: 00-004-0587 (KCl).

Figure 23. XRD results obtained from LT-7h ESD on $AlCl_3{\cdot}6H_2O$, $MgCl_2{\cdot}6H_2O$ and $CaCl_2{\cdot}2H_2O$, compared with standards.